Characterization of the Molecular Structure and Mechanical Properties of Polymer Surfaces and Protein/Polymer Interfaces by Sum Frequency Generation Vibrational Spectroscopy and Atomic Force Microscopy

by

Telly Stelianos Koffas

B.S. (University of California, Los Angeles) 2000

A dissertation submitted in partial satisfaction of the

requirements for the degree of

Doctor of Philosophy

in

Chemistry

in the

GRADUATE DIVISION

of the

UNIVERSITY OF CALIFORNIA, BERKELEY

Committee in charge:

Professor Gabor A. Somorjai, Chair
Professor Herbert L. Strauss
Professor Kyriakos Komvopoulos

Spring 2004

This dissertation of Telly Stelianos Koffas is approved:

_____

Chair Date

_____

Date

_____

Date

University of California, Berkeley

Spring 2004

Characterization of the Molecular Structure and Mechanical Properties of Polymer Surfaces and Protein/Polymer Interfaces by Sum Frequency Generation Vibrational Spectroscopy and Atomic Force Microscopy

by

Telly Stelianos Koffas

Abstract

Characterization of the Molecular Structure and Mechanical Properties of Polymer Surfaces and Protein/Polymer Interfaces by Sum Frequency Generation Vibrational Spectroscopy and Atomic Force Microscopy

by

Telly Stelianos Koffas

Doctor of Philosophy in Chemistry

University of California, Berkeley

Professor Gabor A. Somorjai, Chair

Sum frequency generation (SFG) vibrational spectroscopy, atomic force microscopy (AFM), and other complementary surface-sensitive techniques have been used to study the *surface molecular structure* and *surface mechanical behavior* of biologically-relevant polymer systems. SFG and AFM have emerged as powerful analytical tools to deduce structure/property relationships, in situ, for polymers at air, liquid and solid interfaces. The experiments described in this dissertation have been performed to understand how polymer surface properties are linked to polymer bulk composition, substrate hydrophobicity, changes in the ambient environment (e.g., humidity and temperature), or the adsorption of macromolecules. The correlation of spectroscopic and mechanical data by SFG and AFM can become a powerful methodology to study and engineer materials with tailored surface properties.

The overarching theme of this research is the interrogation of systems of increasing structural complexity, which allows us to extend conclusions made on simpler model systems. We begin by systematically describing the surface molecular composition and mechanical properties of polymers, copolymers, and blends having simple linear architectures. Subsequent chapters focus on networked hydrogel materials used as soft contact lenses and the adsorption of protein and surfactant at the polymer/liquid interface.

The power of SFG is immediately demonstrated in experiments which identify the chemical parameters that influence the molecular composition and ordering of a polymer chain's side groups at the polymer/air and polymer/liquid interfaces. In general, side groups with increasingly greater hydrophobic character will be more surface active in air. Larger side groups impose steric restrictions, thus they will tend to be more randomly ordered than smaller hydrophobic groups. If exposed to a hydrophilic environment, such as water, the polymer chain will attempt to orient more of its hydrophilic groups to the surface in order to minimize the total surface energy.

With an understanding of the structural and environmental parameters which govern polymer surface structure, SFG is then used to explore the effects of surface hydrophobicity and solvent polarity on the orientation and ordering of amphiphilic neutral polymers adsorbed at the solid/liquid interface. SFG spectra show that poly(propylene glycol) (PPG) and poly(ethylene glycol) (PEG) adsorb with their hydrophobic moieties preferentially oriented toward hydrophobic polystyrene surfaces. These same moieties, however, disorder when adsorbed onto a hydrophilic silica/water interface. Water is identified as a critical factor for mediating the orientation and ordering of hydrophobic moieties in polymers adsorbed at hydrophobic interfaces.

The role of bulk water content and water vapor, as they influence hydrogel surface structure and mechanics, continues to be explored in the next series of experiments. A method was developed to probe the surface viscoelastic properties of hydroxylethyl methacrylate (HEMA) based contact lens materials by analyzing AFM force-distance curves. AFM analysis indicates that the interfacial region is dehydrated, relative to the bulk. Experiments performed on poly(HEMA+MA) (MA = methacrylic acid), a more hydrophilic copolymer with greater *bulk* water content, show even greater water depletion at the *surface*. SFG spectra, as well as surface energy arguments, suggest that the more hydrophilic polymer component (such as MA) is not favored at the air interface; this may explain anomalies in water retention at the hydrogel surface. Adsorption of lysozyme onto poly(HEMA+MA) was found to further reduce near-surface viscous behavior, suggesting lower surface water content.

Lastly, protein adsorption is studied using a model polymer system of polystyrene covalently bound with a monolayer of bovine serum albumin. SFG results indicate that some amino acid residues in proteins adopt preferred orientations. SFG spectra also show that the phenyl rings of the bare polystyrene substrate in contact with air or liquid are ordered, with a dipole component directed along the surface normal, but slightly disorder after protein adsorption. Differences in AFM friction values suggest that protein interacts more strongly with the polystyrene substrate at the air/solid interface. The molecular orientation and ordering of surface phenyl groups are also shown to affect substrate hydrophobicity.

_____

Professor Gabor A. Somorjai
Dissertation Committee Chair

For my mother, father, and aunt –

με όλη μου την αγάπη.

Acknowledgements

I remember the nervous excitement at the outset of my graduate career, still wet behind the ears, but with strong notions of the work I wanted to do at Berkeley. The cumulative experience of teaching, challenging coursework, and selecting a research advisor contributed to this anxiety. I had met with several potential research advisors, collected the required signatures, and was prepared to make a decision. I turned the paperwork in to the advisor for experimentalists in our class – Prof. Evan Williams at the time. Handing the form back to me, he had decided I had not met with enough people. I added a few names, indifferently, as my mind had already been made up. Prof. Gabor Somorjai was among the names I added.

As I sat down to meet with him, I was struck by his conviction to lead the group into areas outside his own research background and the ability to distill those ideas into simple questions. The unsolved molecular basis of friction – shoe against pavement, for example – translated into *how do we walk*. Skin – perhaps the ultimate surface – represented an opportunity to take the tools and methods of surface science into the realm of biology. Gabor offered me a unique degree of latitude in outlining and conducting my research. I am grateful to him, as both a teacher and a mentor, for providing me a panoramic vision of science.

My time in the Somorjai group these past four years has been a privilege – encouraging both intellectual and social growth (though I suspect my foosball game could always use a little more help). I am indebted to the postdocs and graduate students I have been fortunate enough to work alongside. Foremost, I thank Jamie Kim, Seong Kim, and Aric Opdahl for helping me to think deeply and conduct

research both independently and collaboratively. I also wish to single out Ella Amitay-Sadovsky, Keng Chou, Sasha Kweskin, and Roger York for their willingness to lend a thoughtful ear or hand. More than a few memorable Friday evenings were spent over pitchers at the Bear's Lair. I am thankful to those in the group who could make the trip. On the flip side, the wry humor of Inger Coble has made the bureaucratic tasks of my time here as painless as possible.

The pursuit to create science is hollow if the highs and lows are unshared. In this regard, I thank my family for their steadfast love and support. Throughout my life, my mom, dad, and aunt have been a humbling source of inspiration. When I loaded up my car and pulled out of their driveway to head 400 miles north on I-5, I was lucky to be making the move with my best friend. But little did I know that I would be equally blessed to add to my family at Cal. I could not celebrate any accomplishment without mentioning those who helped keep life balanced.

Though much could be said about *our* time at Berkeley, words fail to convey the frustration of weekday homework sessions in our first year or the anticipation of weekend outings to the Hotsy and elsewhere in the years that would follow. Thank you to Tony Dutoi, Jeff Grunes, Matt Nee, Kim Pierce, Alex Sodt, Harsha Vaswani, and those in the Tilley group for memories I will always cherish and also to Hsu Li and Zach Zwald – one-time roommates, but also lifelong friends. Lastly, from grade school to graduate school, let me acknowledge wonderfully uncommon friendships with Richard Brutchey and Melissa Morlok. Though this chapter has come to a close, they say that the adventure lies in those that are yet unwritten. And once again, I find myself making a move northward with a friend.

Contents

List of Figures and Tables

Introduction

The study of polymer surfaces and thin films cuts across synthetic, surface, and colloid chemistry, as well as traditional materials and biomaterials science. Industry depends on the surface properties of polymers in products involving coatings,[1] colloidal stability,[2,3] lubrication and adhesion,[4,5] and biocompatibility.[6] A goal of many academic and industrial researchers is to be able to systematically tune the surface chemical and surface mechanical properties of a polymer to a desired application. Recent technological advances, for example, have seen polymer surfaces designed for use as biological scaffolds[7] and drug delivery systems[8] and also as nanopatterned templates and films for use in microelectronics,[9] catalysis,[10,11] and sensor development.[12] The combination of versatility and relative low cost has made polymer films ubiquitous in technological applications at ever-shrinking length scales. In order to understand the interaction of the polymer with its environment at these size regimes, it becomes increasingly important to have experimental measurements of the surface chemical and mechanical properties of these materials and to understand how these properties are modified as the environment is

Figure 0.1: Various polymer environments. An astronaut's extravehicular mobility unit contains a polyurethane-coated nylon pressure bladder, a polyester structural restraint layer with folded and pleated joints (for mobility), and a woven Kevlar, Teflon, and Dacron anti-abrasion outer layer. Skin represents a biopolymer of elastin and collagen, with interesting transport properties. The fiberglass hull of a boat is held together by an epoxy resin. Application of a paint coating reduces frictional drag by incorporating biocides that impede the growth of marine organisms. Tires are made from vulcanized rubber and reinforced with carbon black filler for improved mechanical properties.

changed. Figure 0.1 illustrates various polymeric materials interfacing with vacuum, gas, liquid, and solid environments.

Since the mid-1990s, researchers in the Somorjai group have conducted several studies aimed at understanding polymer interface behavior, using sum frequency generation (SFG) vibrational spectroscopy and atomic force microscopy (AFM). The overarching theme of this research, and in my graduate career, in particular, has been one of increasing structural complexity (reference Figure 0.2). The reasoning is two-fold: (1) The interrogation of more complex materials allows us to test and refine earlier conclusions regarding which parameters control polymer surface behavior (and to what extent); and, not coincidentally, (2) more complex materials are inherently more interesting and find wider application in biomaterials science. This dissertation begins with the surface molecular and mechanical characterization of simple polymer/air and polymer/liquid interfaces and ends with in situ studies of protein adsorption on polymer surfaces. These latter studies seek to identify what can be learned by exporting the tools and methods of surface science to address outstanding questions in biology and medicine. After all, most biological phenomena (e.g., enzymatic reaction, biomineralization, and molecular adsorption, adhesion, recognition, and transport) occur not within an aqueous medium, but at an interface.

The fact that polymeric surfaces have been exploited and optimized by nature is not surprising. Despite the inherent complexity of biological systems and their interactions with synthetic biomaterials, the basic concepts of surface science still apply.[6,13] Surfaces offer a readily accessible and low-energy pathway for chemical

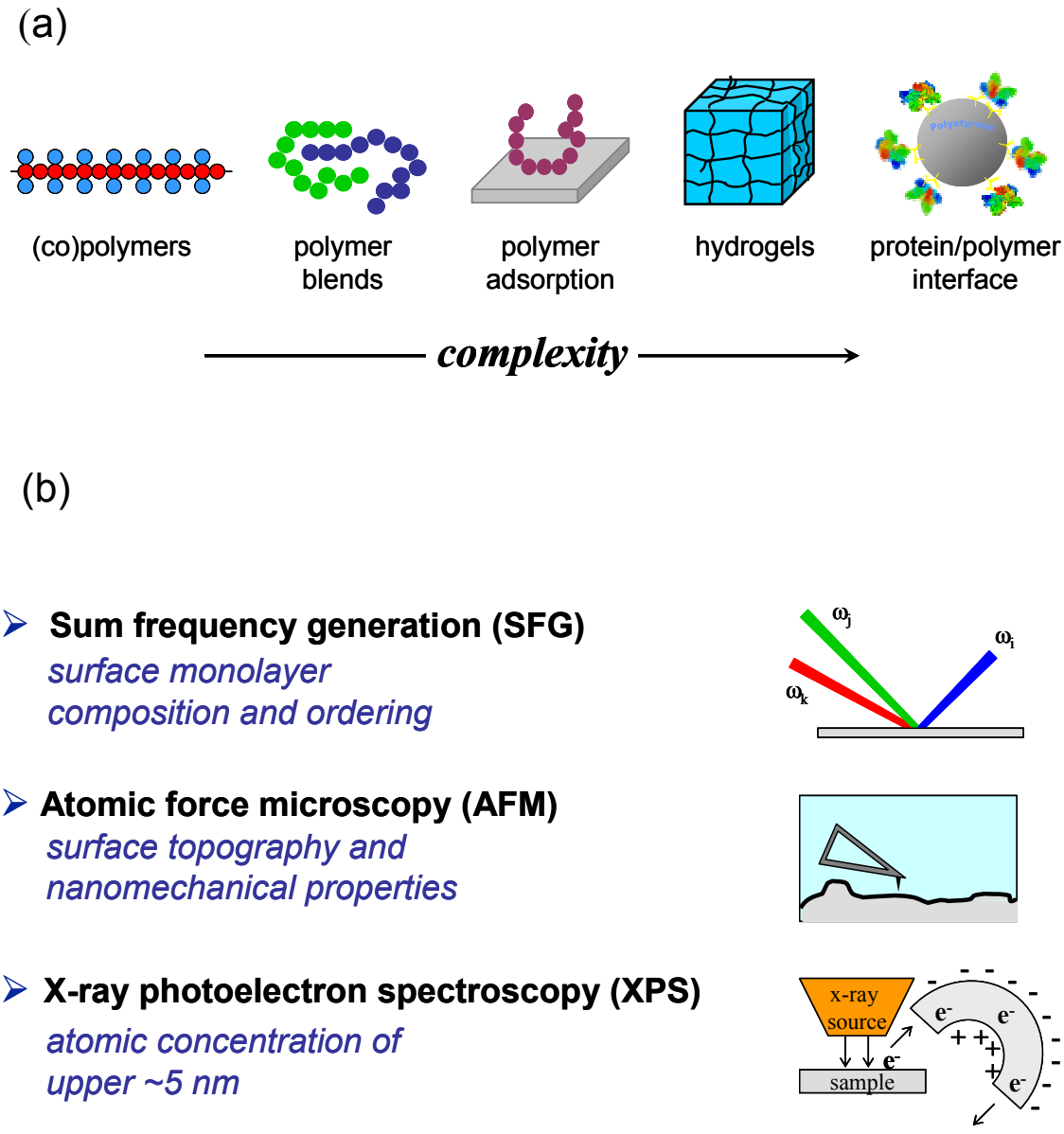

Figure 0.2: (a) Increasing structural complexity of polymer systems explored in this dissertation and (b) the primary surface analytical tools used to interrogate them.

conversion that is unavailable in aqueous solution.[14] High surface area geometries can be used to drive complex or energetically unfavorable biological reactions toward higher turnover rates.[15] Surfaces also offer opportunities for precise molecular self-assembly and epitaxial growth.[16] A more complete understanding of the molecular surface structure and mechanical properties of biopolymers and how they are affected by protein adsorption, mechanical deformation, or changes in the local environment is needed because these factors define what it means for a material to be biocompatible.[17-20]

A major hurdle in developing a surface science model for biomedical systems has been the limitation imposed by traditional electron-based, surface analytical tools.[21,22] Atomic and molecular-level studies of the surface monolayers of solids often require the use of very low background pressures or even ultrahigh vacuum to allow electrons and other probes to reach or leave a free surface unimpeded. Biology, however, involves surfaces exposed to more routine pressures or the meeting of two condensed phases to create a buried interface. The development of optical and scanning probe techniques which could be conducted outside of a vacuum, along with preparation methods which leave fragile samples chemically and morphologically unaltered, have allowed researchers to study more interesting systems under biologically-relevant conditions.[23-29]

SFG and AFM have emerged as powerful in situ surface analytical tools to deduce structure/property relationships in a host of model polymer systems.[30-36] SFG vibrational spectroscopy, as an optical technique, provides a chemical description of the surface – what functional groups are present, their orientation, and the general state of molecular order. In turn, polymer surface chemistry underlies phenomena such as adsorption, wettability, friction, lubrication, adhesion, and, ultimately, biocompatibility.

By determining the morphology and mechanical properties associated with certain surface chemical compositions and environmental variables, AFM can complement the spectroscopic data collected by SFG and paint a clearer portrait of what is occurring at the surface.

Chapter 1 describes the theory and application of the primary surface analytical tools used in the experiments described in the dissertation. SFG, as a method to collect surface vibrational spectra, and AFM, as a tool for imaging and a probe of surface mechanical properties, are introduced. Representative SFG spectra are shown which highlight the effect of side branch length, surface energy, and sterics, as well as ambient environment (e.g., air, liquid, or vapor), on the molecular configuration of various polymer surfaces. Molecular-level conclusions made from an analysis of SFG spectra concerning the surface enrichment or hydrophobicity of copolymers and blends can often be corroborated by AFM mechanical testing. The basic features of an AFM force vs. distance curve, which are used to measure surface stiffness, viscoelasticity, and adhesion, are presented in this context.

Chapter 2 discusses the effects of hydrophobicity and solvent polarity on the orientation and ordering of amphiphilic neutral polymers, in an *adsorption* experiment at the solid/liquid interface. SFG spectra indicate that poly(propylene glycol) (PPG) and poly(ethylene glycol) (PEG) adsorb with their hydrophobic moieties preferentially oriented toward hydrophobic polystyrene surfaces. However, the hydrophobic moieties in PPG and PEG disorder when adsorbed at the hydrophilic silica/water interface. Water is a critical factor for mediating the orientation and ordering of hydrophobic moieties in polymers adsorbed at hydrophobic interfaces. When methanol is substituted in place of

water solvent, neither PPG nor PEG displays structural ordering when adsorbed on polystyrene substrates. We demonstrate that hydrophobic surfaces and water solvent are required to molecularly order functional groups in adsorbed amphiphilic neutral polymers at the solid/liquid interface.

In Chapters 3 and 4, the role of surface water on the surface mechanical properties of poly(2-hydroxyethyl methacrylate)-based [poly(HEMA)] hydrogel contact lenses is monitored as functions of humidity and bulk polymer formulation by AFM. Surface stiffness, adhesion, and viscoelastic effects are extracted from AFM force vs. distance interaction curves and are found to be strongly dependent on the bulk water content of the hydrogel and on the relative humidity. SFG is also used to assess whether the surface chemical composition of the hydrogel at the air interface biases interfacial water retention. At low relative humidity, the surface region has mechanical properties similar to those measured on totally dehydrated hydrogels. As the relative humidity exceeds ~60% and surface evaporation decreases, the hydrogel surface softens and the viscoelastic relaxation time decreases. In an ocular environment, although the bulk of the poly(HEMA) contact lens is hydrated, the surface region may be in a transition between a dehydrated glassy state and a hydrated rubbery state.

The surface mechanical properties of neutral poly(HEMA) are also compared with an ionic poly(HEMA+MA) hydrogel (MA = methacrylic acid), which has a greater equilibrium *bulk* water content. A lag in the onset of viscoelastic behavior at the poly(HEMA+MA) surface, relative to poly(HEMA), was found. This suggests that poly(HEMA) actually possesses greater *interfacial* water content than the more hydrophilic poly(HEMA+MA) material. The loss in surface water content in

poly(HEMA+MA) is only exacerbated by adsorption and penetration of lysozyme into the hydrogel matrix; ionic HEMA-based materials, which carry a negative charge at ocular pH, are known to stabilize deposition through electrostatic interactions with positively-charged protein.

Structural investigations of bare and surface-modified polystyrene beads by SFG and AFM are reported in Chapters 5 and 6 and build on the adsorption studies of Chapter 2. Bead surfaces are modified by either the covalent linking of immunoglobulin G (IgG) and bovine serum albumin (BSA) or the nonspecific adsorption of a Pluronic surfactant. SFG signals in the aliphatic CH-stretch region are detected at both the air/liquid and air/solid interfaces, indicating that some amino acid residues in proteins adopt preferred orientations. SFG results indicate that the hydrophobic PPG moieties in the adsorbed Pluronic triblock copolymer order, whereas hydrophilic PEG groups align to a lesser extent. This suggests a conformation in which the central PPG section of the block copolymer is physisorbed onto the bead surface and the PEG chains are in solution, which allow the surfactant to retard subsequent protein adsorption.

SFG spectra also show that the phenyl rings of bare polystyrene beads in contact with air or liquid are ordered, with a dipole component directed along the surface normal, but become less ordered after the adsorption of either protein or surfactant. Molecular orientation and ordering at the bead surface affect its hydrophobicity and aggregation behavior, as observed in AFM imaging. The strength of protein adsorption, measured via the torque acting on the AFM tip, was also found to vary at the polymer/liquid and polymer/air interfaces. Differences in the friction values suggest that BSA interacts more strongly with the bead at the air/solid interface.

References

(1) Wicks Z. W., *Organic Coatings: science and technology*; Wiley: New York, 1992.

(2) Goodwin J. W.; Buscall R., *Colloidal Polymer Particles*; Academic Press: London, 1995.

(3) Kawaguchi H., *Prog. Polym. Sci.* **2000**, *25*, 1171.

(4) Israelachvili. J. *J. Vac. Sci. Technol. A* **1992**, *10*, 2961.

(5) Aoike T.; Uehara H.; Yamanobe T.; Komoto T. *Langmuir* **2001**, *17*, 2153.

(6) Castner, D. G.; Ratner B. D. *Surf. Sci.* **2002**, *500*, 28.

(7) Karp, J. M.; Dalton P. D.; Shoichet, M.S. *MRS Bull*. **2003**, *28*, 301.

(8) Davis K. A.; Anseth K. S. *Crit. Rev. Ther. Drug.* **2002**, *19*, 385.

(9) Ito, H.; Tagawa, S.; Horie, K., *Polymeric Materials for Microelectronics Applications: Science and Technology*; American Chemical Society: Washington, D.C., 1994.

(10) Wuff, G. *Chem. Rev.* **2002**, *102*, 1.

(11) Kralik, M.; Biffis, A. *J. Mol. Catal. A-Chem.* **2001**, *177*, 113.

(12) Akmal, N.; Usmani A.M. *Polymers in sensors: theory and practice*; American Chemical Society: Washington, D.C., 1998.

(13) Kasemo, B. *Surf. Sci.* **2002**, *500*, 656.

(14) Dabrowski, A. *Adv. Colloid Interfac.* **2001**, *135*, 93.

(15) Berg, O. G. *Interfacial Enzyme Kinetics*; Wiley: New York, 2002.

(16) Otsuka, H.; Nagasaki, Y.; Kataoka, K. *Curr. Opin. Colloid. In*. **2001**, *6*, 3.

(17) Ratner, B. D.; Castner, D. G. *Surface Modification of Polymeric Biomaterials*; Plenum: New York, 1996.

(18) Recum, A. F. *Handbook of Biomaterials Evaluation: Scientific, Technical, and Clinical Testing of Implant Materials*; Macmillan: New York, 1986.

(19) Park, J. B.; Lakes, R. S. *Biomaterials: An Introduction*; Plenum: New York, 1992.

(20) Tirrell, M.; Kokkoli, E.; Biesalski, M. *Surf. Sci.* **2002**, *500*, 61.

(21) Woodruff D.; Delchar, T. *Modern Techniques of Surface Science*; Cambridge University Press: Cambridge, 1986.

(22) Somorjai, G. A. *Introduction to Surface Chemistry and Catalysis*; Wiley: New York, 1994.

(23) Shen, Y. R. *The Principles of Nonlinear Optics*; Wiley: New York, 1984.

(24) Shen, Y. R. *Nature* **1989**, *337*, 519.

(25) Eisenthal, K. B. *Chem. Rev.* **1996**, *96*, 1343.

(26) Binnig, G.; Quate, C. F.; Gerber, C. *Phys. Rev. Lett.* **1986**, *56*, 930.

(27) Cohen, S. H.; Lightbody, M. L. *Atomic Force Microscopy/Scanning Tunneling Microscopy 3*, Kluwer, New York, 1999.

(28) Rider, K. B.; Hwang, K. S.; Salmeron, M.; Somorjai, G. A. *Phys. Rev. Lett.* **2001**, *86*, 4330.

(29) Lindsay, S. M.; Nagahara, L. A.; Thundat, T.; Knipping, U.; Rill, R. L. *J. Biomol. Struct. Dyn.* **1989**, *7*, 279.

(30) Miyamae, T.; Nozoye, H. *Surf. Sci.* **2003**, *532*, 1045.

(31) Ye, S.; Noda, H.; Morita, S.; Uosaki, K.; Osawa, M. *Langmuir* **2003**, *19*, 2238.

(32) Chen, C.; Wang, J.; Woodcock, S. E.; Chen, Z. *Langmuir* **2002**, *18*, 1302.

(33) Amitay-Sadovsky, E.; Komvopoulos, K.; Tian, Y.; Somorjai, G. A. *Appl. Phys. Lett.* **2002**, *80*, 1829.

(34) Salmeron, M. *Tribol. Lett.* **2001**, *10*, 69.

(35) Zhang, D.; Gracias, D. H.; Ward, R.; Gauckler, M.; Tian, Y.; Shen, Y. R.; Somorjai, G. A. *J. Phys. Chem. B* **1998**, *102*, 6225.

(36) Kim, S. H.; Marmo, C.; Somorjai, G. A. *Biomaterials* **2001**, *22*, 3285.

Chapter 1

Application of SFG Vibrational Spectroscopy and AFM to the Study of Polymer Surfaces and Polymer/Protein Interfaces

1.1 Introduction to SFG for polymer surface studies

Experimental studies of vibrationally-resonant SFG were pioneered in the early 1980s by Yuen-Ron Shen at UC Berkeley. The theoretical and phenomenological framework of SFG has been treated extensively in publications by his group[1-4] and by Hirose[5]. SFG spectra are obtained by spatially and temporally overlapping two intense electric fields at an interface and measuring the light generated at the sum frequency by the second-order, nonlinear process. Eq. 1-1 shows that the intensity of this light, $I(\omega_s)$, is proportional to the square of the nonlinear susceptibility, $\vec{\vec{\chi}}^{(2)}$, a third-rank tensor which characterizes the effect of the applied electric fields on the nonlinear optical polarization,

$\vec{P}^{(2)}$. Eq. 1-1 also reveals that SFG signal intensity from a centrosymmetric medium is parity-forbidden. Under the electric-dipole approximation, the 27 components of $\vec{\vec{\chi}}^{(2)}$ will equal or cancel out to zero in a material that possesses inversion symmetry or that is randomly oriented in the bulk. However, if the molecular groups in a material adopt a preferred anisotropic orientation, symmetry is broken in the interfacial plane and some components of $\vec{\vec{\chi}}^{(2)}$ will become non-zero. Measurement of $\vec{\vec{\chi}}^{(2)}$ is specifically sensitive to this type of polar ordering, and its magnitude will depend, in part, upon the transmission Fresnel coefficients of the two media forming the interface.

$$I(\omega_s) \propto \left|\vec{P}^{(2)}(\omega_s)\right|^2 = \left|\varepsilon_0 \vec{\vec{\chi}}^{(2)}(\omega_s = \omega_1 + \omega_2) : \vec{E}(\omega_1)\vec{E}(\omega_2)\right|^2 \qquad (1\text{-}1)$$

In SFG vibrational spectroscopy, one of the input fields is a tunable infrared (IR) beam; the second beam is fixed at 532 nm. The vibrationally-resonant contribution to the surface nonlinear susceptibility, $\vec{\vec{\chi}}_R^{(2)} = n_s \left\langle \vec{\vec{\alpha}}_R^{(2)} \right\rangle_f$, is enhanced when the IR beam (ω_2) is tuned near a vibrational mode belonging to one of the molecular groups at the interface (ω_q). Here, $\vec{\vec{\alpha}}_R^{(2)}$ is the molecular hyperpolarizability. The non-resonant term, $\vec{\vec{\chi}}_{NR}^{(2)}$, originates from an electronic interaction of the visible beam with the substrate; $\vec{\vec{\chi}}_{NR}^{(2)}$ can interfere with the resonant term to produce lineshapes similar to those observed in coherent anti-Stokes Raman spectroscopy. The oscillator strength for the q^{th} vibrational mode ($\vec{\vec{A}}_q$) is related to the number density of contributing oscillators (n), an orientation-averaged transformation between laboratory (i, j, k) and molecular (l, m, n) coordinate systems, and the product of both the dynamic dipole and polarizability ($a_{q,lmn}$), as shown in Eqs. 1-3 and 1-4. This constrains SFG to vibrational modes that obey both IR and

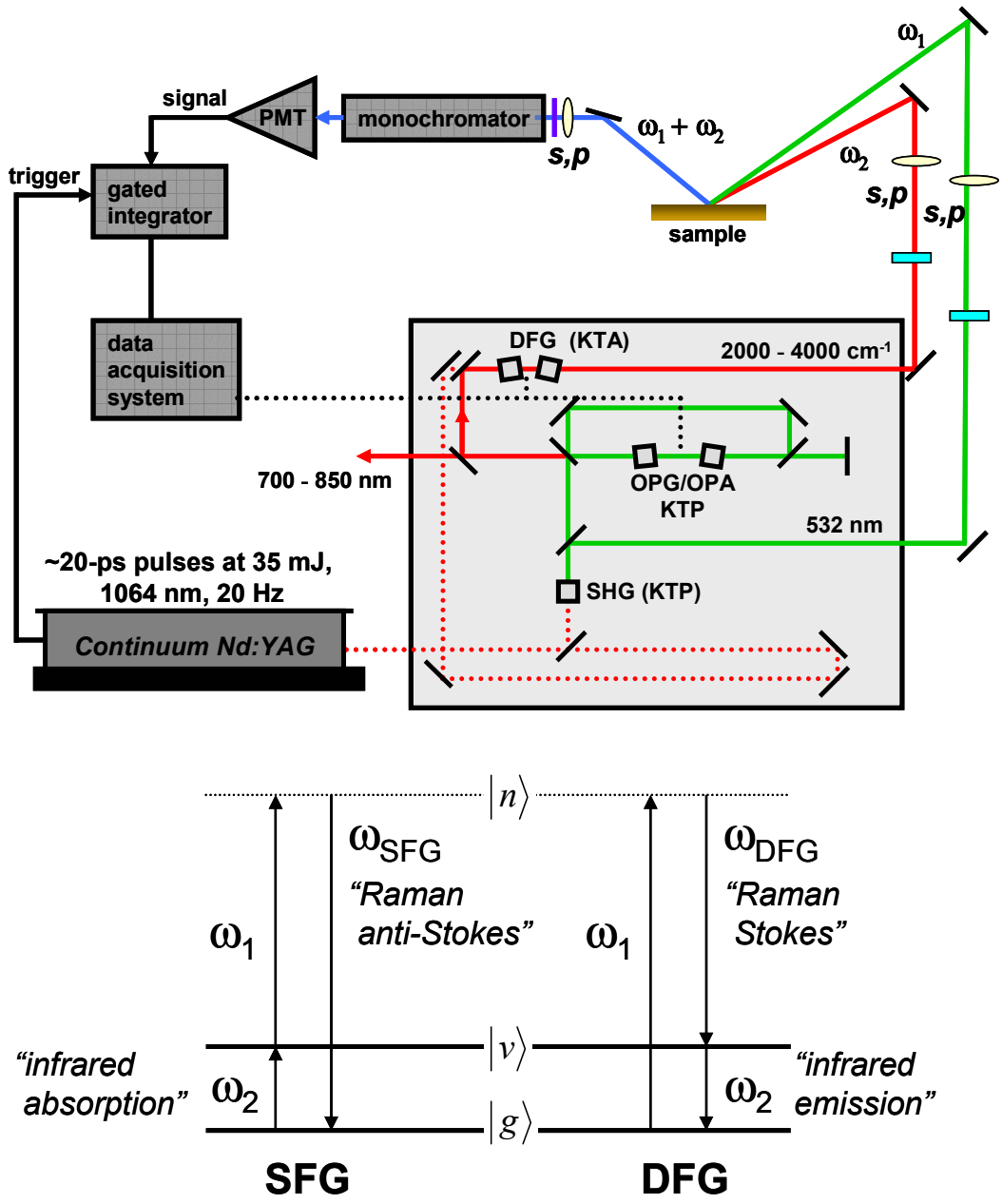

Figure 1.1: Schematic of the SFG optical and data acquisition setup, including the OPG/OPA tunable infrared source. Also shown is an energy level diagram for sum and difference frequency generation. SFG involves transitions into excited vibrational, $|v\rangle$, and virtual, $|n\rangle$, states and then relaxation back to the vibrational ground state, $|g\rangle$, through what can be pictured as a Raman anti-Stokes process.

Raman selection rules, as depicted in the energy level diagram in Figure 1.1.

$$\vec{\vec{\chi}}^{(2)} = \vec{\vec{\chi}}^{(2)}_{NR} + n_s \left\langle \vec{\vec{\alpha}}^{(2)}_{R} \right\rangle_f = \vec{\vec{\chi}}^{(2)}_{NR} + \sum_q \frac{\vec{\vec{A}}_q}{\omega_2 - \omega_q + i\Gamma_q} \tag{1-2}$$

$$\vec{\vec{A}}_{q,ijk} = n_s \left\langle \vec{\vec{a}}_q \right\rangle_f = n \sum_{lmn} \vec{\vec{a}}_{q,lmn} \left\langle (\hat{i} \cdot \hat{l})(\hat{j} \cdot \hat{m})(\hat{k} \cdot \hat{n}) \right\rangle \tag{1-3}$$

$$\vec{\vec{a}}_{q,lmn} = -\frac{1}{2\varepsilon_o \omega_q} \frac{\partial \mu_n}{\partial Q_q} \frac{\partial \alpha_{lm}}{\partial Q_q} \tag{1-4}$$

Vibrational spectra presented in this dissertation are obtained in the CH-stretching region (2700–3100 cm^{-1}), using the $s_{sfg}s_{vis}p_{ir}$ (*ssp*) polarization combination, which specifically probes the *yyz* (or *xxz*) component of $\vec{\vec{A}}_q$. Spectra are fit to a Lorentzian model using Eqs. 1-1 and 1-2 in order to extract the position and strength for each mode. If the components of $\vec{\vec{a}}_q$ for a vibrational mode are known (estimation methods are given in references 2 and 5), then the fitted values for $\vec{\vec{A}}_q$ can be used to estimate the number density and orientation of the ordered molecular groups giving rise to the vibration. In Eq. 1-2, Γ_q is an additional parameter which defines the spectral line-width associated with each mode. Appendix A describes the background of SFG in further detail and uses a geometric bond additivity model to treat simple CH and CH_2 vibrations.

Figure 1.2 presents simulated SFG spectra expected from a surface made up of a collection of CH_2 oscillators. The CH_2 groups have tilt angle orientation distributions centered at 0° (upright) and 60° (tilted), with Gaussian distribution widths of 2° (well-ordered) and 40° (less-ordered). This figure shows that the ratio of the CH_2(s)/CH_2(a) peak intensities will be largest in the $s_{sfg}s_{vis}p_{ir}$ spectrum if the CH_2 groups are upright and

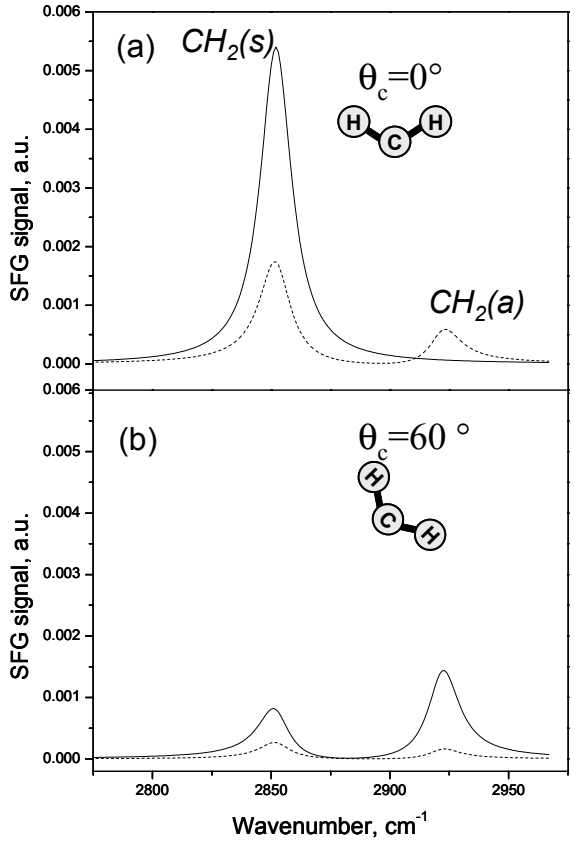

Figure 1.2: Simulated SFG spectra ($s_{sfg}s_{vis}p_{ir}$ polarization) showing the CH_2(s) and CH_2(a) peak intensity dependencies on tilt (θ_c) and randomness ($\Delta\theta$). Solid lines are the spectra expected for a narrow distribution of orientations ($\Delta\theta$ = 2°, Gaussian), dashed lines are the spectra expected for a broad distribution of orientations ($\Delta\theta$ = 40°, Gaussian).

well-ordered. The ratio will be smaller for less-ordered surfaces and also if the CH_2 groups are tilted. Additional spectra can be obtained using other polarization combinations ($s_{sfg}p_{vis}s_{ir}$ and $p_{sfg}p_{vis}p_{ir}$) in order to further define the orientation and ordering or molecular groups. In many cases, SFG spectra can be used to significantly restrict the possible orientations of the species at an interface to a narrow range of values.

1.2 SFG optical setup

Figure 1.1 provides a schematic of the optical layout used in SFG vibrational spectroscopy. Spectra are obtained with a passive-active mode-locked Nd:YAG laser (Leopard, Continuum, Santa Clara, CA) equipped with a negative feedback loop in the oscillator cavity to enhance shot-to-shot stability. The 1064-nm light generated has a pulse width of 21 ps and the laser operates at a 20-Hz repetition rate. Radiation is sent to an optical parametric generator/amplifier (OPG/OPA) stage (LaserVision, Bellevue, WA) where tunable IR radiation is produced in addition to frequency-doubled radiation at 532 nm. The OPG/OPA consists of two parts. The first is an angle-tuned potassium titanyl phosphate (KTP) stage pumped with 532-nm light to generate near-IR radiation between 1.35–1.85 μm. This output is then mixed with the 1064-nm fundamental in an angle-tunable potassium titanyl arsenate (KTA) stage to produce an IR beam that can be tuned between 2000–4000 cm^{-1} (7 cm^{-1} FWHM). The IR and visible electric fields are polarized in either *s* or *p* just prior to arriving at the sample.

The tunable IR beam is spatially and temporally combined with 532-nm radiation at the interface at incident angles of 51° and 42°, respectively, with respect to the surface

normal. SFG photons produced from the sample pass through a polarizer; the *s*- or *p*-polarized component is detected by a photomultiplier tube, sent to a gated integrator, and stored digitally. For each scan, data are collected with 200 shots/data point in 5 cm^{-1} increments and normalized by the IR beam intensity measured at the sample stage.

1.3 Application of SFG to polymer/protein studies

Several surface-sensitive techniques have been used to study biological interfaces, each possessing certain advantages and drawbacks. Contact angle measurement[6] is a standard method to monitor macroscopic changes in surface energy, but yields no molecular information. Fourier-transform infrared (FTIR) and Raman spectroscopies possess good wavenumber resolution but lack the inherent surface sensitivity of SFG.[7-9] X-ray photoelectron spectroscopy (XPS) and secondary ion mass spectroscopy (SIMS) are surface sensitive but require a vacuum (even with a cold stage).[10-12] SFG is one the principal analytical methods in our laboratory to collect molecular information at interfaces under *ambient conditions*.

SFG, as a powerful and versatile in situ surface probe, not only permits the identification of surface molecular species, but also provides a means to calculate the spatial orientation of functional groups by comparing mode strengths. Recall that this high surface specificity and sub-monolayer resolution arise from the fact that even-ordered nonlinear processes vanish in centrosymmetric media under the electric-dipole approximation. In general, for bulk-amorphous polymer surfaces, signal is generated solely from the surface. Only proteins adsorbed on a material surface – and the surface

itself – will on average break inversion symmetry to give SFG; because proteins in bulk solution are distributed isotropically, they do not produce signal.

The spatial orientations of amino acid residues in adsorbed proteins on solid substrates play an important role in subsequent biological events (e.g., replacement, coagulation, and the formation of an adsorption-resisting layer against other encroaching proteins and cells).[13,14] This is especially critical to biofouling and biocompatibility applications; the coagulation of protein followed by cell adhesion is the first step in bacterial growth, contamination, and implant rejection. Studies of surface structure, such as amino acid orientation in adsorbed proteins, are necessary to understand and predict complex adsorption behavior, with the ultimate goal of designing surfaces that either prevent protein adsorption or form highly-oriented protein layers.

Future application of SFG to dynamic biological processes must address the need for increased sensitivity in the time domain. A Ti:sapphire-based optical parametric amplifier system can generate mid-IR pulses with femtosecond pulse duration. There are two advantages to using femtosecond IR pulses: First, the bandwidth of IR pulses generated in this system is on the order of 100 to 200 cm^{-1}. A typical SFG spectrum covers around 200 cm^{-1}. By using a charge-coupled device (CCD) area detector, the entire SFG spectrum can be monitored at the same time, substantially reducing the data acquisition time. At a 1-kHz repetition rate, a spectrum can be collected within a few seconds. With this data acquisition rate, the dynamics of surface-induced protein denaturation or secondary structure change in peptides can be probed. Additionally, most energy transfer processes at surfaces occur on picosecond to femtosecond timescales. By employing pump-probe methods, vibrational energy transfer mechanisms can be studied.

1.4 Examples of SFG spectra obtained from polymer/air interfaces

SFG spectra obtained from polymer interfaces are sensitive to the number density and orientation of ordered molecular groups in the interface region, and are uniquely sensitive to the polymer configuration at an interface. Like molecules in liquids,[3] many polymers have been observed by SFG to preferentially orient the lowest surface energy structural unit at the polymer/air interface. A major difference between polymers and molecules in liquids, however, is that the configuration of a polymer chain is restricted by the connectivity of chain segments along the backbone. Polymers do not have the conformational freedom that molecules in liquids have and, consequently, the equilibrium surface structure reflects a compromise between ordering a particular structural unit at the interface and steric restrictions imposed by the polymer chain. Many polymers are capable of restructuring their surfaces in response to a change in environment (e.g., in liquid contact).[15] SFG surface vibrational spectroscopy is capable of probing the types of molecular rearrangements that occur at buried polymer/liquid interfaces.

1.4.1 Atactic polypropylene/air and aspecific poly(ethylene-*co*-propylene) rubber/air interfaces

SFG spectra obtained from polymers with short methyl side branches, *a*PP and *a*EPR, are shown in Figure 1.3. In each of these spectra, the strongest resonant feature is at 2883 cm^{-1} and is assigned as the CH_3(s) stretch from the methyl side branches.[16,17] The feature at 2968 cm^{-1} is assigned to the CH_3(a) stretch from the side branch. The features at 2850 cm^{-1} and 2920 cm^{-1} are assigned as the CH_2(s) and CH_2(a) stretches from the

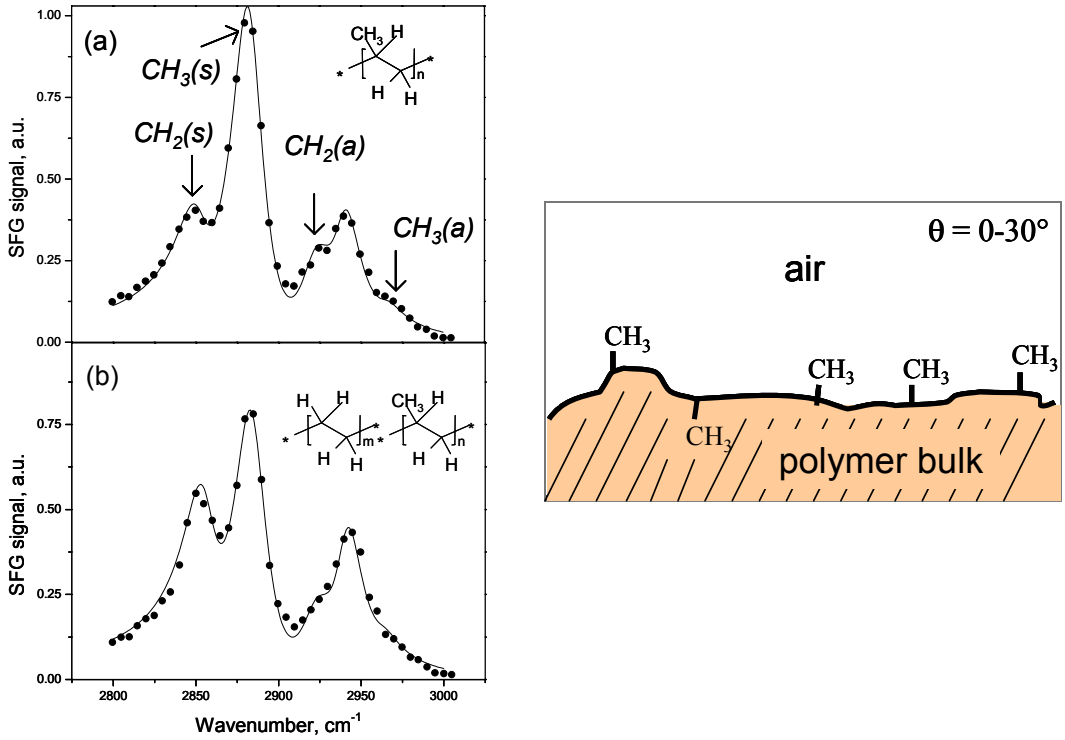

Figure 1.3: SFG spectra ($s_{sfg}s_{vis}p_{ir}$ polarization) of the (a) atactic polypropylene (*a*PP)/air interface and (b) poly(ethylene-*co*-propylene) rubber (*a*EPR)/air interface. The large intensity of the peak associated with the CH_3(s) vibration suggests side branches are ordered at the polymer/air interface for both polymers. The ethylene-rich *a*EPR orients excess side branches at the interface, relative to the bulk composition.

polymer backbone, respectively. The strong CH_3(s) peak suggests that the methyl side branches have a tendency to order at the polymer/air interface. In contrast, for hydrocarbon polymers without short side branches (e.g., polyethylene[16] and polyethylene glycol[18]), backbone CH_2 units, which have a slightly higher surface tension than CH_3 groups, have been observed to preferentially order at the polymer/air interface. Like the CH_2(s) peak, the peak associated with the CH_3(s) vibration will be strongest if the methyl groups are oriented upright; the large ratio of the CH_3(s)/CH_3(a) peaks observed in the *a*PP and *a*EPR spectra is interpreted as an indication of an upright orientation.

An important observation in the SFG spectrum of *a*EPR is the small reduction in absolute intensity of the peak associated with the CH_3(s) vibration, as compared to its intensity in the spectrum of *a*PP. The *a*EPR copolymer is comprised of ~60% propylene monomers randomly incorporated in the polymer chain, and a given chain length has ~60% as many methyl side branches as *a*PP. For this situation, Eq. 1-3 predicts the intensity of the peak associated with the CH_3(s) vibration from *a*EPR should be ~36% as intense (the oscillator strength, A_q, should be 60% as large) as that from *a*PP. That the *a*EPR CH_3(s) peak is enhanced in intensity suggests one of three possibilities: (1) *a*EPR orders a higher percentage of methyl side branches at the surface compared to *a*PP, (2) the methyl side branches are oriented more upright at the *a*EPR surface than they are at the *a*PP surface, or (3) the methyl side branches are more tightly ordered for *a*EPR than they are for *a*PP. Detailed analysis of the oscillator strengths, A_q, extracted from the SFG spectra shows that the most likely scenario is (1) and that the ethylene-rich *a*EPR copolymer oriented ~50% surface excess methyl branches compared to *a*PP.[17] This

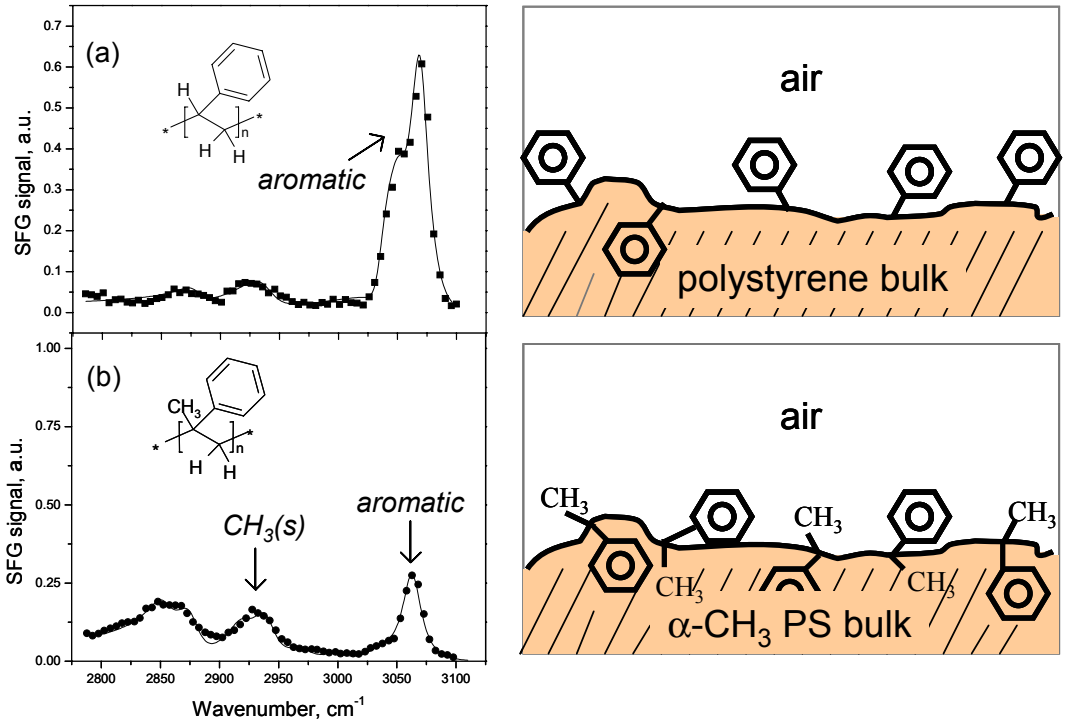

Figure 1.4: SFG spectra ($s_{sfg}s_{vis}p_{ir}$ polarization) of the (a) polystyrene/air interface and (b) poly(α-methyl)styrene/air interface. Neither side branch displays a strong upright orientation at the poly(α-methyl)styrene/air interface.

conclusion is reasonable because polymers with more ethylene in the backbone tend to have a higher degree of conformational flexibility than highly-branched polymers. This example shows that the number of side branches oriented at the polymer/air interface is limited by the steric restrictions imposed by the chain architecture.

1.4.2 Polystyrene/air and poly(α-methyl)styrene/air interfaces

An SFG spectrum of a polystyrene film is shown in Figure 1.4(a). The SFG spectrum of polystyrene has been widely studied[19-22] and the dominant feature at ~3060 cm^{-1} has been assigned to the symmetric v_2 stretch from the aromatic side group, which, at a basic level, indicates that phenyl side branches, like the alkyl branches in polyolefins, preferentially order at the polystyrene/air interface.

In contrast, an SFG spectrum of poly(α-methyl)styrene, which has both a methyl and phenyl branch attached to the same backbone carbon atom, is shown in Figure 1.4(b). The overall vibrational intensities in this spectrum are significantly lower those those measured for polypropylene or polystyrene. The phenyl branch peak at ~3060 cm^{-1} is visible. Yet its intensity is significantly weaker than that observed in the spectrum of pure polystyrene. Similarly, the CH_3 side branch peak at ~2880 cm^{-1} is visible, but it is much weaker than the CH_3(s) mode of polypropylene. This suggests that neither side branch is strongly oriented upright at the interface. The methyl side branch is expected to have a slightly lower surface energy than the aromatic side branch,[23] but the aromatic branch is slightly larger. This suggests that for polymers with multiple side branches per repeat unit, differences in the surface energy of the individual side branches and in the size of the side branches may both be important in determining the surface structure in air.

SFG data suggest that if the difference in surface tension of the two side branches is large, than the side branch with lower surface tension will tend to aggregate at the polymer/air interface. This is evident from SFG results obtained from the surface of poly(2-hydroxyethyl methacrylate) (poly(HEMA)).[24] Analysis of the SFG spectra of poly(HEMA), which has a methyl side branch and a larger, more hydrophilic hydroxyethyl side branch, has shown that the *smaller*, low surface energy methyl branch preferentially orders at the polymer/air interface. In contrast, if the difference in surface tension of the components is small and the difference in size of the side branches is large, then the contribution from the larger side branch will dominate the SFG spectra. This is evident from SFG results obtained from the surface of polymethylmethacrylate (PMMA) by Chen.[25] SFG studies of PMMA, which has a small methyl side branch and a much larger methyl methacrylate side branch, have shown that the dominant spectral feature is associated with the terminal methyl group in the larger ester side branch – indicating that the *larger* methyl ester side branch preferentially orients at the interface.

1.5 Examples of SFG spectra obtained from polymer/liquid interfaces

1.5.1 Polystyrene/toluene interface

Polymer surfaces restructure when they are placed in contact with a liquid. An example is the case of polystyrene exposed to toluene.[26] Toluene is a solvent for polystyrene and will readily penetrate a polystyrene film at ambient temperature. An SFG spectrum obtained from the toluene liquid/vapor interface is shown in Figure 1.5(a). A spectrum obtained from a polystyrene film exposed to a vapor pressure of toluene (22 torr

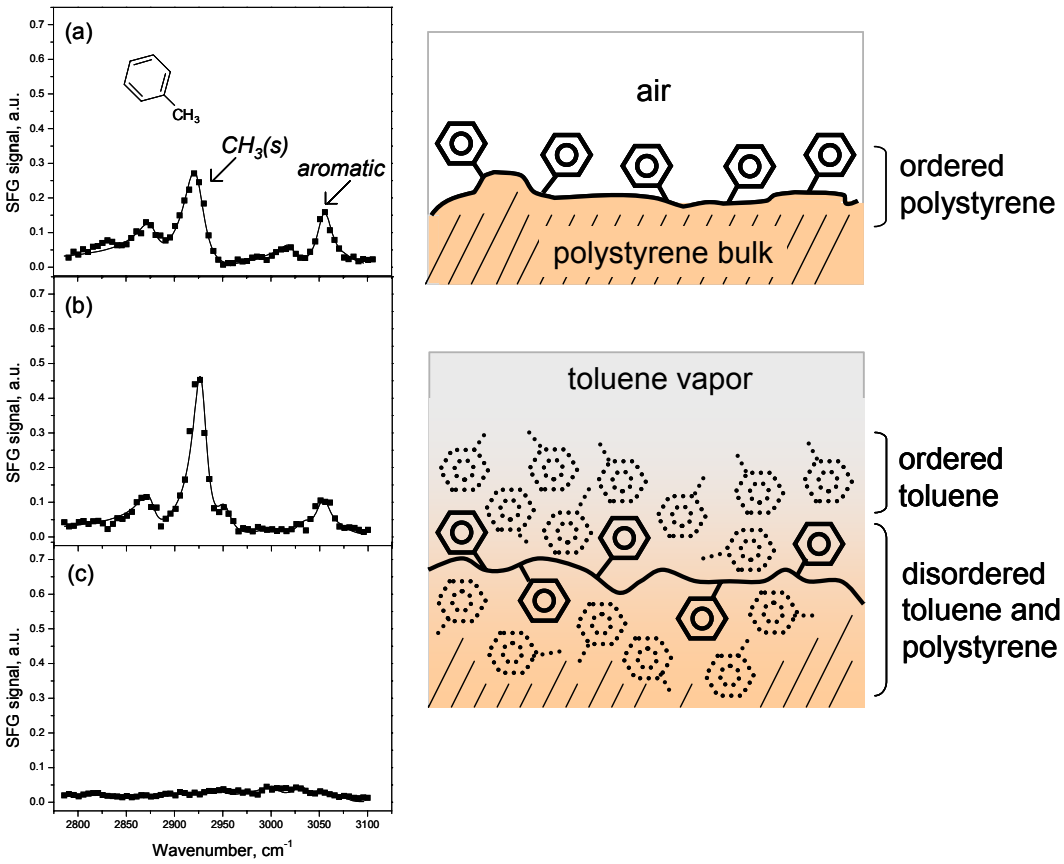

Figure 1.5: SFG spectra ($s_{sfg}s_{vis}p_{ir}$ polarization) of the (a) toluene liquid/vapor interface, (b) polystyrene exposed to toluene vapor, and (c) polystyrene exposed to deuterated toluene vapor. Toluene coats and disrupts the ordering of the underlying polystyrene.

at 20 °C) is also shown in Figure 1.5(b). These two spectra are qualitatively similar, indicating that when polystyrene is exposed to toluene vapor, toluene orders at the interface. This observation can be understood by the relative difference in surface tension of the two components – 27 dyne/cm for toluene [27] vs. 40 dyne/cm for polystyrene[28]. Figure 1.5(c) shows an SFG spectrum obtained from a polystyrene film exposed to fully deuterated (d_8) toluene. The use of deuterated toluene removes spectral interferences between toluene and polystyrene. Here, very little sum-frequency signal is generated in the CH-stretching region, showing that in addition to coating the surface of polystyrene, toluene penetrates and disrupts the ordering of the underlying polystyrene film.

1.5.2 Polypropylene/methanol interface

An ordered interface is formed between polypropylene and methanol. Methanol is a not a good solvent for polypropylene. Figure 1.6(a) shows an SFG spectrum obtained from the methanol liquid/vapor interface. The feature at 2830 cm^{-1} is assigned to the CH_3(s) stretch arising from methanol and the features at 2920 cm^{-1} and 2940 cm^{-1} have been assigned as Fermi resonances between the CH_3(s) stretch and overtones of CH_3 bending vibrations.[29] An SFG spectrum collected from the *a*PP/methanol interface is shown in Figure 1.6(b). The best fit of the data to Eq. 1-2 is obtained using a combination of vibrational peak assignments from *a*PP and from methanol – indicating that both the *a*PP and methanol components are ordered at the interface. Resonant features in an SFG spectrum can constructively or destructively interfere with one another, depending on the orientation of the two molecular groups giving rise to the resonant features.[30] In these spectra, the best fit for the SFG spectrum of the *a*PP/methanol interface is obtained if the

CH_3(s) stretch from the *a*PP and the CH_3(s) stretch from methanol destructively interfere with one other – indicating that at the *a*PP/methanol liquid interface, the CH_3 groups from methanol orient toward the CH_3 side branches from *a*PP.

Analysis of SFG spectra shows that the configuration of *a*PP methyl side branches is similar at the *a*PP/air and *a*PP/methanol interfaces. Air is generally considered to provide a hydrophobic interface. Because amphiphilic methanol molecules align with their methyl groups oriented toward the interface, methanol is also believed to produce a 'hydrophobic' interface. Recent studies by Wilson et al. indicate that the configuration of polystyrene phenyl side branches at polystyrene/air and polystyrene/hydrophobic solid interfaces is similar.[31] On hydrophilic interfaces, the phenyl branches were shown to adapt a different orientation, suggesting that polystyrene side branches readily reorient at hydrophobic or hydrophilic interfaces. The results obtained from polypropylene support the notion that the hydrophobicity of the interface plays a key role in influencing the configuration of polymer side branches at buried interfaces.

1.5.3. Polypropylene/water interface

The importance of interface hydrophobicity is further supported by data obtained from the *a*PP/water interface. An SFG spectrum collected from the *a*PP/water interface is shown in Figure 1.6(c). The overall intensity of the CH_3(s) vibration is significantly lower than it is in the spectrum collected from the *a*PP/air interface. Additionally, the intensity of the CH_3(s) peak decreases in magnitude, relative to the CH_3(a) peak. This indicates that *a*PP methyl side branches are not well-oriented toward the liquid phase,

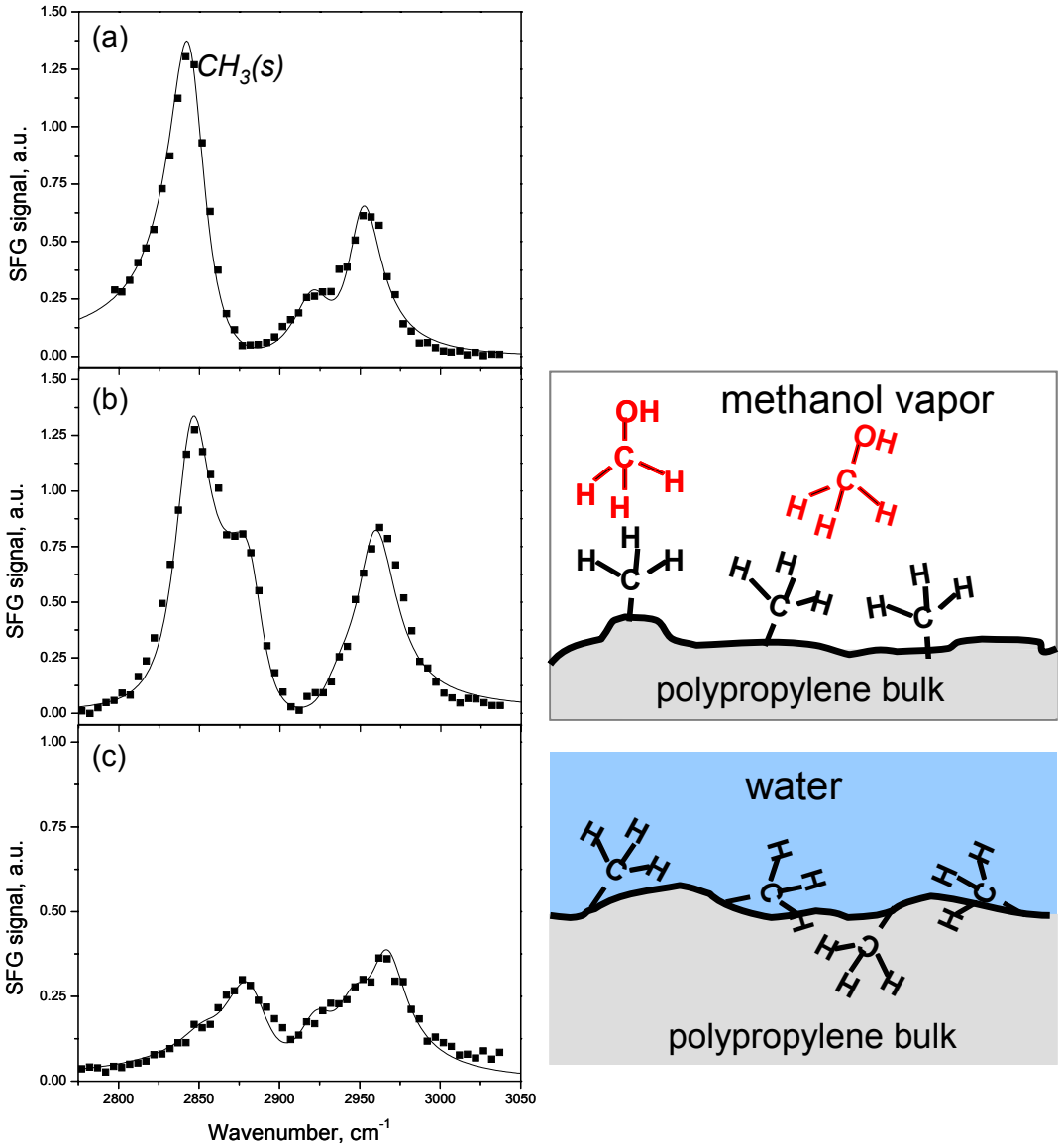

Figure 1.6: SFG spectra ($s_{sfg}s_{vis}p_{ir}$ polarization) of the (a) methanol liquid/vapor interface, (b) *a*PP/methanol liquid interface, and (c) *a*PP/water interface. Methyl groups are observed to order through hydrophobic interactions.

compared to the *a*PP/methanol and *a*PP/air interfaces. The methyl groups at the interface are either more randomly distributed or are tilted away from the water interface. Results by Wang et al. from the poly(butyl methacrylate) (PBMA)/water interface have shown that the orientation of the ester side branch changes when PBMA is placed in water.[32] An important distinction between PBMA and *a*PP is that the ester side branch of PBMA is capable of hydrogen bonding with the water. Thus, the PBMA side branches may restructure due to favorable interactions at the polymer/water interface.

1.6 Introduction to contact-mode AFM

The examples above demonstrate the unique sensitivity of SFG experiments to the global molecular order and structure of an interface and the ability to observe the restructuring that occurs as a result of environmental change. When more local-scale information obtained from AFM probe microscopy is correlated with that obtained from SFG spectroscopy, the picture of polymer surface behavior becomes more robust and the interpretation of data more meaningful.

AFM, a member of the family of scanned probe microscopes (SPM), was developed in 1986 by Gerd Binnig and Christoph Gerber of IBM Zurich and Cal Quate of Stanford.[33] This instrument uses a sharp tip to collect topographic and surface mechanical information with sub-Ångstrom vertical (*z*-direction) resolution, and is sensitive to forces in the piconewton range. The technique is well-suited to biology, as nonconductive surfaces are studied in situ (i.e., in air or aqueous environments).[34] The tip (radius of curvature < 20 nm) sits at the free end of a long, flexible cantilever (~100 μm), which is microlithographically fabricated from silicon. The tip is typically made of a hard material

(e.g., silicon nitride) so that it will not deform during sample penetration or imaging. The force constant (k) of the cantilever can be varied by altering its thickness or geometry.

The cantilever itself is mounted to the end of a chip for macroscopic handling. Chip (and, consequently, tip) movement is coupled to the motion of piezoelectric actuators, which are ceramics whose solid state structure is altered in response to an applied voltage. This structural distortion occurs at roughly 50Å/V, and is properly calibrated by imaging a grating with known step size features. All piezo motion is driven by an SPM controller, which independently delivers identical or varying voltages to each actuator. This allows the piezos to shrink or expand uniformly during an approach/retract cycle or buckle left and right during imaging. As the piezos lower the tip or raster it across the surface, cantilever motion is carefully monitored with a photodiode. In the setup illustrated in Figure 1.8, a laser beam is bounced off the top-side of the cantilever and is reflected into a photodiode, which measures the beam intensity separately in each of four areas. By comparing beam intensities (measured as voltages) in each quadrant, the up-and-down and lateral movement of the tip is registered simultaneously. Cantilevers are typically coated with a thin and reflective metallic layer to boost signal strength.

During approach, any combination of attractive (negative) van der Waals, electrostatic, or capillary forces can cause the tip to abruptly make contact within a few nanometers of the surface. Once the sudden change in cantilever deflection is registered by the photodiode, the approach is halted and the tip is backed slightly away from the surface. A set force can then be reapplied by gently lowering the tip into the sample via the piezos. Positive forces, originating from electron-electron repulsion, are measured as the tip is driven further into the surface and the material beneath it becomes compressed.

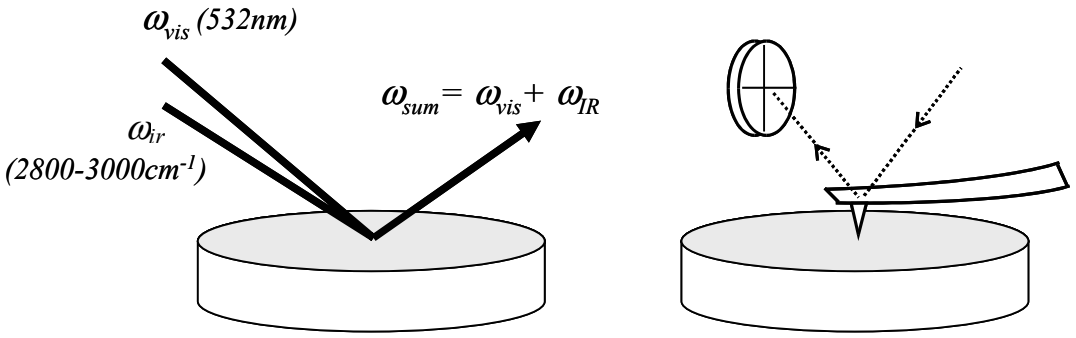

SFG	AFM
Surface sensitivity: monolayer	Surface sensitivity: subnanometer to several hundred nanometers
Surface monolayer composition	Imaging of surface lateral morphology (submicron to several micron)
Interface ordering of molecular groups	Surface mechanical behavior (stiffness, viscoelasticity) Friction and adhesion

Figure 1.7: Experimental information and sensitivity available by SFG vibrational spectroscopy and AFM.

When the tip encounters elevated and depressed features on a surface during imaging, the piezos are raised and lowered via a feedback loop to maintain a *constant cantilever deflection*, which implies a *constant load* (for known *k*). A three-dimensional topographic map is generated by spatially recording this piezo motion. Tip bluntness limits resolution in the lateral (*x*-*y*) plane to a nanometer at best. Friction is tracked by measuring the torque on the tip during a line-scan; the reported value is the average of the absolute voltage signals in both directions. This stress originates from a local chemical contrast or surface slope. Thus, it is important to relate friction maps to the corresponding topography to ensure that any frictional differences are not topographic artifacts.

1.7 Application of AFM to polymer surface studies

Figure 1.7 juxtaposes the information that can be accessed with SFG and AFM. The AFM imaging (topographic and frictional) and force experiments described in this dissertation were performed by two instruments. A commercial force microscope (Park Instruments) was primarily used to collect topography, while a second AFM system was used to determine the mechanical properties of the polymer samples. This homebuilt, walking-style AFM scanning head, controlled by RHK electronics (Troy, MI) is completely enclosed within a 30-L glass bell jar.[35] The experiments on hydrogels, described in Chapters 3 and 4, require the control of humidity within the AFM chamber. The relative humidity in this system can be varied by balancing the evaporation of water from a reservoir within the jar with a steady flow of nitrogen through the chamber. Decreasing the flow rate of nitrogen increases the experimental humidity, which is measured by a digital hydrometer placed inside the chamber.

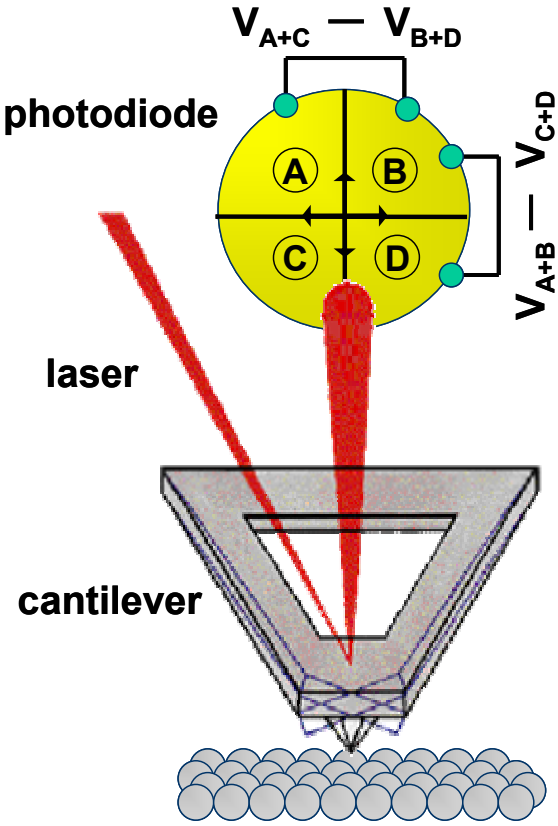

Figure 1.8: Laser reflection geometry in AFM. Cantilever motion is reflected in the location of the laser spot that falls on a photodiode. The ratio of the path length between the cantilever and the photodiode to the length of the cantilever itself produces a mechanical amplification. As a result, the system can detect sub-Ångstrom vertical movement of the cantilever tip. Vertical motion is registered by comparing the voltages in the upper and lower quadrants, while the voltage difference between left and right quadrants indicates the amount of torque on the cantilever.

Because plastics are soft (i.e., elastic moduli in the MPa range, and generally no greater than 1 GPa), the AFM tip can easily deform the surface.[36] With the proper choice of cantilever force constant (appreciable to the stiffness of the sample of interest), one can easily differentiate between different components that have segregated to the surface. Care must be exercised to prevent irreversible damage to the polymer (e.g., chain scission) with large loads.

Force-displacement curves (refer to Figure 1.9) are used to extract qualitative and sometimes quantitative surface mechanical behavior.[37] The curve measures the bending of the cantilever as it is pressed against a surface (no feedback loop is maintained). The amount of bending can be converted into a load if k is known for the cantilever. The magnitude of the attractive van der Waals interaction on the tip increases as the tip nears the surface. An instability occurs when this interaction force (the gradient of the interaction potential) exceeds the cantilever stiffness. The tip is said to 'snap into' the surface. As the tip presses against the surface, the cantilever bends and the polymer surface is usually deformed (where the degree of strain depends on the value of k).

If the polymer responds as a perfectly elastic material (which is normally the case in the limit of low loads), then there is no hysteresis between approach and retract curves. The shape and slope of the approach curve depend primarily on the coupled elastic behavior of the cantilever and the sample. If the polymer does not deform at all ($k_{lever} < k_{polymer}$), the response of the force-distance curve reflects only cantilever bending. For this situation, any differences in surface mechanical behavior will be poorly resolved; it is, however, appropriate for imaging, since the lower relative force of the cantilever prevents the occurrence of deformation-induced topographic artifacts. The slope of the tangent to

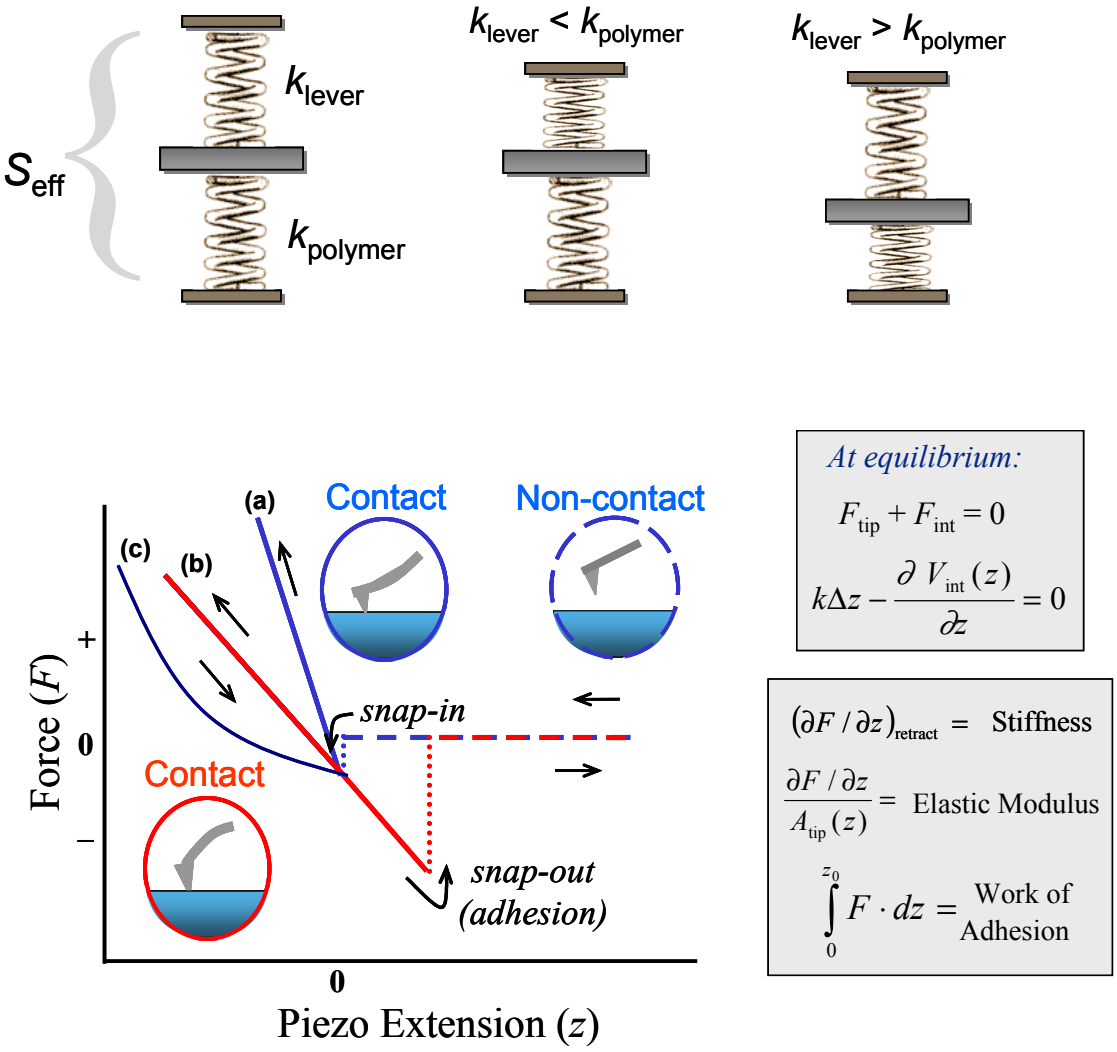

Figure 1.9: Schematic of an AFM force vs. distance plot. Lines (a) and (b) represent idealized elastic behavior as the cantilever is brought into contact with the surface in the loading cycle. The slope of the retract curve provides the stiffness. Curve (a), with a greater slope than (b), represents the response of a stiffer material. The measured effective stiffness (S_{eff}) is the response of two elastic elements (cantilever and polymer) connected in series. The response in (c) is indicative of viscoelastic behavior. The work of adhesion is measured by the area bounded in either the loading or unloading well.

the retract curve gives the instantaneous material stiffness. Deformation mechanics, however, are properly described by an elastic modulus – the proportionality constant between the stress brought by the AFM tip and the strain induced in the material.

The Hertz model for the indentation of a half-sphere into a plane can be used to extract the elastic modulus by normalizing S to the tip-sample contact area.[38] Variables involved in the relationship are identified in Figure 1.10. Because this model neglects adhesive effects, the contact area can be underestimated. Eq. 1-5 shows that the total travel of the z-piezo (Δz) is the sum of sample deformation (δ) and cantilever bending (Δd). The far right-hand side of Eq. 1-5 assumes the deformation is Hertzian, allowing δ to be expressed as a function of Δd. In this model, the contact area (a) is a function of the cantilever force constant (k), tip radius of curvature (R), and elastic modulus (E), as shown in Eq. 1-6. Indentation data, however, is normally collected as $F(\Delta z) = k(\Delta d)$; thus, an expression in terms of the experimentally measured surface stiffness ($\partial(\Delta F)/\partial z$) must be obtained. This is done by taking the derivative with respect to z after solving Eq. 1-5 for Δd. Hooke's Law can then be used to rewrite $\partial(\Delta d)/\partial z$ as the stiffness.

$$\Delta z = \delta + \Delta d = a(\Delta d)^{2/3} + \Delta d \tag{1-5}$$

$$a = \left(\frac{9k^2}{16RE^2} \right)^{1/3} \tag{1-6}$$

$$\frac{\partial(\Delta d)}{\partial z} = \frac{\partial(\Delta F / k)}{\partial z} = \frac{1}{k}\frac{\partial(\Delta F)}{\partial z} \tag{1-7}$$

The work of adhesion (γ) is estimated by integrating the force over the snap-in or snap-out distance. In a purely elastic loading cycle, the work gained bringing two surfaces together equals the work expended in pulling them apart – no energy dissipation

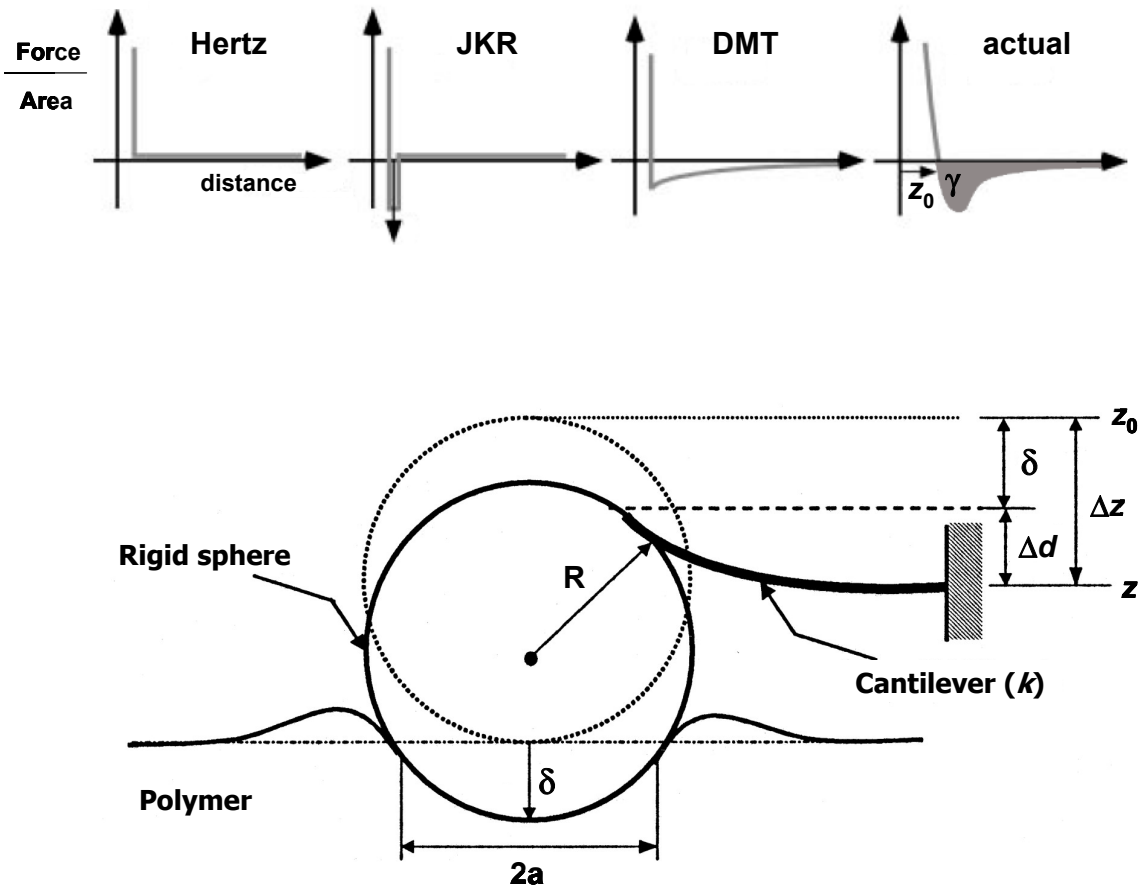

Figure 1.10: Schematic of an AFM indentation experiment, where Hertzian mechanics are used to estimate the elastic modulus. This model uses a hard-wall repulsive contact and neglects adhesion forces that could lead to increased tip-surface contact areas. The Johnson–Kendall–Roberts (JKR) and Derjaguin–Müller–Toporov (DMT) models use short- or long-range adhesion forces, respectively, to better approximate the surface potential between the half-sphere and plane.

occurs (e.g., viscoelastic creep). Large values for γ often indicate a strong capillary force (~100 nN) acting on the tip, and will increase with the ambient humidity as the adsorbed water layer thickens. The capillary force balances out to zero for measurements performed with the tip fully immersed in water. Further details of the procedures and assumptions involved in these measurements are provided in Chapters 3 and 4.

These chapters also discuss a procedure which probes the soft hydrogel surface at different rates to study polymer relaxation processes. Hydrogels, due to the presence of water, exhibit strongly time-dependent viscoelastic behavior under mechanical deformation.[39] Relaxation times are related to the cooperative motion of the polymer-water system under stress. By identifying the probing rate at which a polymer surface undergoes a mechanical transition (e.g., from viscoelastic to elastic), an estimate of the timescale of polymer motion can be established.

1.8 Conclusion

SFG and AFM, together with complementary surface diagnostic tools such as XPS and contact angle goniometry, constitute a powerful methodology to study the surface structure and surface mechanical properties of model polymer and biopolymer materials. These techniques can be used to follow the restructuring of polymer surfaces in response to parameters such as bulk composition, surface energy differences, mechanical strain, or chemical environment. If one expects to acquire meaningful data, surfaces must be studied in situ, under the conditions in which biopolymers may be employed.

AFM, as a tool to correlate surface molecular composition with the nanoscale elastic behavior and topography, is a recurring approach in the studies that follow. It is

hoped that these techniques, in concert, may be able to assess synthetic schemes which attempt to improve, for example, surface water retention in contact lenses, or the biocompatible response of implant materials.

Forthcoming examples will better illustrate the advantages of connecting data gathered by SFG surface spectroscopy and AFM probe microscopy to interpret interfacial phenomena occurring in polymer systems. Efforts must be made, however, to overcome certain experimental limitations in SFG. The time resolution of SFG must be decreased to seconds to be able to follow more dynamic phenomena and the frequency range for a given scan must also be expanded to access greater molecular structure information. To strengthen correlation arguments, the spatial resolution of SFG experiments (several hundred square microns) must also be improved to match the <50 nm spatial resolution of AFM experiments. Despite these hurdles, SFG and AFM remain among the most promising technologies to study biopolymer surfaces in realistic environments.

1.9 Appendix A: SFG and the bond additivity model

An induced dipole, $\vec{\mu}$, in the presence of weak (non-laser) light is expressed as

$$\vec{\mu}(\omega) = \vec{\mu}^{(0)}(\omega) + \alpha\vec{E}(\omega), \qquad \text{(A-1)}$$

where $\vec{\mu}^{(0)}$ is the static molecular dipole, α is the polarizability (a 3x3 tensor), and $\vec{E}$ is the electric field of the incident radiation. This expression describes the linear optical response of a dipole, which is exploited in conventional IR spectroscopy or ellipsometry.

If the polarization, $\vec{P}$, is defined as the dipole per unit volume ($\vec{P} = \vec{\mu}/V$) then the polarization can be written as:

$$\vec{\mu}(\omega)/V = \vec{\mu}^{(0)}(\omega)/V + \alpha\vec{E}(\omega)/V \tag{A-2}$$

$$\vec{P}(\omega) = \vec{P}^{(0)}(\omega) + \varepsilon_0\chi^{(1)}\vec{E}(\omega)\ . \tag{A-3}$$

The static polarizability, $\vec{P}^{(0)}$, is zero for most materials. The linear susceptibility for *N* molecules is

$$\chi^{(1)} = \frac{N\langle\alpha\rangle}{\varepsilon_o V}, \tag{A-4}$$

where $\langle\alpha\rangle$ is the molecular polarizability averaged over all orientations.

Laser radiation (i.e., high electromagnetic field strength) induces an anharmonic response in the dipole moment. Consequently, higher-order nonlinear terms must be included. The expression for the dipole moment now takes the general form:

$$\vec{\mu} = \vec{\mu}^{(0)} + \alpha\vec{E} + \beta : \vec{E}\vec{E} + \gamma\vdots\vec{E}\vec{E}\vec{E} + \cdots. \tag{A-5}$$

Here, β and γ are the first and second hyperpolarizabilties, where $\beta : \vec{E}\vec{E}$ is a summation over the incident electric fields, $\sum_{j,k}\beta_{i,j,k}E_jE_k$.

The expression for the polarizability (assuming the usual case that $\vec{P}^{(0)} = 0$) is now

$$\vec{P}(\omega, 2\omega,...) = \vec{P}^{(0)} + \vec{P}^{(1)} + \vec{P}^{(2)} + \cdots = \varepsilon_0\chi^{(1)}\vec{E}(\omega) + \varepsilon_0\chi^{(2)} : \vec{E}(\omega)\vec{E}(\omega) + \cdots, \tag{A-6}$$

where $\beta = \varepsilon_0\chi^{(2)}$ and $\chi^{(2)}$ is the second-order susceptibility (a third rank tensor). This term describes the lowest-order nonlinear optical response responsible for SHG.

$$\vec{P}^{(2)} = \begin{bmatrix} P_x \\ P_y \\ P_z \end{bmatrix} = \varepsilon_0 \begin{bmatrix} \chi_{xxx} & . & . \\ . & \chi_{yyy} & . \\ . & . & \chi_{zzz} \end{bmatrix} \begin{bmatrix} E_x{}^1 \\ E_y{}^1 \\ E_z{}^1 \end{bmatrix} \begin{bmatrix} E_x{}^2 \\ E_y{}^2 \\ E_z{}^2 \end{bmatrix} \tag{A-7}$$

In a medium with inversion symmetry, the incoming fields E(ω) and −E(ω) must induce polarizations of P(2ω) and –P(2ω), respectively:

$$\vec{P}^{(2)}(2\omega) = \chi^{(2)}\vec{E}(\omega)\vec{E}(\omega) \tag{A-8}$$

$$-\vec{P}^{(2)}(2\omega) = \chi^{(2)}\left(-\vec{E}(\omega)\right)\left(-\vec{E}(\omega)\right) = \chi^{(2)}\vec{E}(\omega)\vec{E}(\omega) \tag{A-9}$$

For Eqs. A-8 and A-9 to be consistent ($\vec{P}^{(2)} = -\vec{P}^{(2)}$), $\chi^{(2)}$ must be zero (SHG-forbidden) within the medium (note that chiral materials are SHG-active because they do not have bulk inversion symmetry).

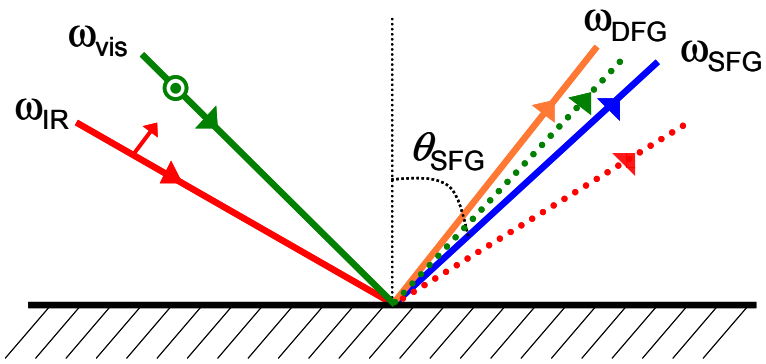

Two polarized electric fields, each of which has the general expression

$$\vec{E}(r,t) = E(r)\cos(\omega t), \tag{A-10}$$

and are incident at frequencies of ω_1 and ω_2 at the same time, t, generate the sum and difference frequencies. By definition, the reflected sum frequency is collected in SFG.

$$\vec{P}^{(2)} = \varepsilon_0\chi^{(2)} : \vec{E}\vec{E} = \varepsilon_0\chi_{i,j}{}^{(2)}\vec{E}_j\vec{E}_k[\cos(\omega_1 t)\cos(\omega_2 t)] \tag{A-11}$$

$$= \frac{1}{2}\varepsilon_0\chi_{i,j}{}^{(2)}\vec{E}_j\vec{E}_k[\cos(\omega_1+\omega_2)t + \cos(\omega_1-\omega_2)t] \tag{A-12}$$

The incident and outgoing beams, each directed at a different angle, θ, from the surface normal, must obey conservation of momentum and energy, given respectively by:

$$\vec{k}_{\text{SFG/DFG}}\sin(\theta_{\text{SFG/DFG}}) = \vec{k}_{\text{vis}}\sin(\theta_{\text{vis}}) \pm \vec{k}_{\text{IR}}\sin(\theta_{\text{IR}}) \tag{A-13}$$

$$\vec{k}_{\text{SFG/DFG}} = \vec{k}_{vis} \pm \vec{k}_{\text{IR}} \tag{A-14}$$

where $\vec{k}$ is the wavenumber $\frac{2\pi}{\lambda}$.

The intensity, *I*, of the SFG signal goes as:

$$I(\omega_{\mathrm{SFG}}) \propto \left|\vec{P}^{(2)}\right|^2 \propto \left|\chi^{(2)}\right|^2 \left|\vec{E}_{\mathrm{vis}}\vec{E}_{\mathrm{IR}}\right|^2 = \left|\chi^{(2)}\right|^2 I(\omega_{\mathrm{vis}})I(w_{\mathrm{IR}}) \tag{A-15}$$

By using or collecting different polarizations of incident and outgoing beams, different components of $\chi^{(2)}$ are measured, with *s*-polarized light comprised of $\vec{E}_y$ and *p*-polarized light comprised of $\vec{E}_x$ and $\vec{E}_z$. In the notation *ssp*, for example, the first term refers to *s*-polarized SFG light being collected and the second and third terms refer to *s*- and *p*-polarized visible and IR beams impinging on the sample. Thus, for *ssp*, 2 combinations of $\chi^{(2)}$ exist: $\chi_{\mathrm{yyx}}{}^{(2)}$ and $\chi_{\mathrm{yyz}}{}^{(2)}$.

For an isotropic surface, x = y, x = –x, and x = –y. $\chi_{\mathrm{yyx}}{}^{(2)}$ vanishes, whereas $\chi_{\mathrm{yyz}}{}^{(2)}$ survives at an isotropic surface ($z \neq -z$)

$$\chi_{\mathrm{yyx}} = \chi_{\mathrm{yyy}} = \chi_{\mathrm{yy(-x)}} = -\chi_{\mathrm{yyx}} = 0 \tag{A-16}$$

$$\chi_{\mathrm{yyz}} = \chi_{\mathrm{(-y)(-y)z}} = \chi_{\mathrm{yyz}} \tag{A-17}$$

$\chi_{\mathrm{yyz}}{}^{(2)}$ vanishes in the bulk where either effective (random dipoles, e.g., a liquid) or true (ordered lattice) inversion symmetry exists. $\chi^{(2)}$ is made up of resonant and non-resonant terms and exists for each normal mode of a molecule. It can be mathematically approximated by a Lorentzian function:

$$\chi^{(2)} = A_{\mathrm{NR}} + \frac{A_{\mathrm{R}}}{\omega_{\mathrm{IR}} - \omega_0 - i\Gamma} \tag{A-18}$$

A_{NR} appears as a background signal within a spectrum, but it can also interfere as a cross-term with A_{R}, as implied when expression A-18 is squared; whether the interference is constructive or destructive depends on the relative sign of the two terms

and whether A_{NR} is real or imaginary. A_R is proportional to the number of molecules giving rise to the vibration, their orientational average, and the strength of their IR and Raman transition moments:

$$A_R \propto N\langle\beta\rangle = N\left\langle\left(\frac{\partial\alpha}{\partial q}\right)\left(\frac{\partial\mu}{\partial q}\right)\right\rangle \tag{A-19}$$

Both the polarizability (α) and dipole moment (μ) must vary with bond length distortion (q) for a molecule to be SFG-active (i.e., it must be Raman- and IR-active). To deal with such vibrations, we must transform the coordinates of the laser (its x-, y-, and z-polarization) to the molecule's reference frame.

$$\chi_{yyz}^{\text{macro}} = N\langle\beta^{molec}\rangle \tag{A-20}$$

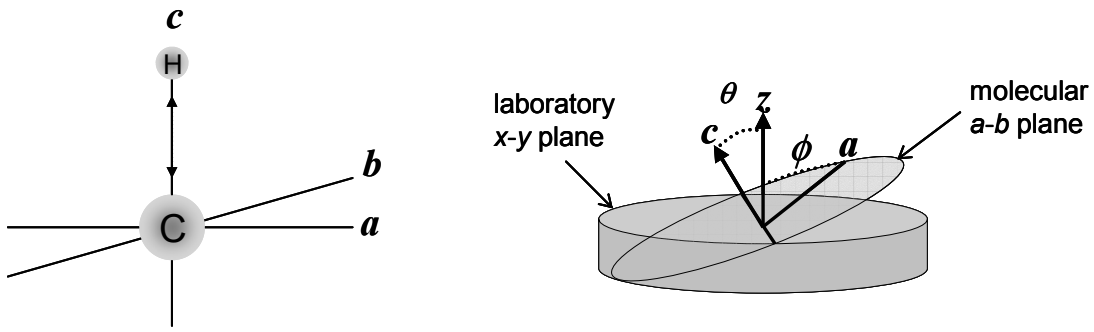

For a CH-stretch, a coordinate system where vibrational motion is restricted to the *c*-axis can be established. In this configuration, dipole and polarizability components existing in the *c*-*a* or *c*-*b* planes do not enter into the expression for $\chi_{yyz}^{(2)}$. We are concerned with only 1 (out of a total of 27) tensor elements. The neglected terms are exceedingly small. By using the following relationships:

$$\beta_{ccc} = \left(\frac{\partial\alpha_{cc}}{\partial q}\right)\left(\frac{\partial\mu_c}{\partial q}\right) \tag{A-21}$$

$$\vec{P} = \begin{bmatrix} \alpha_{aa} & . & . \\ . & \alpha_{bb} & . \\ . & . & \alpha_{cc} \end{bmatrix} \begin{bmatrix} E_a \\ E_b \\ E_c \end{bmatrix} \approx \vec{P}_c = \alpha_{cc}\vec{E} \tag{A-22}$$

$$\chi_{\mathrm{yyz}}^{(2)} = N\left\langle \sum_{\substack{i,j,k= \\ a,b,c}} \beta_{i,j,k} \right\rangle \approx N\langle \beta_{ccc} \rangle \tag{A-23}$$

the angular components of $\langle \beta_{ccc} \rangle$ can be resolved separately of the magnitude:

$$N\langle \beta_{ccc} \rangle = N\langle \hat{y}\cdot\hat{c}\rangle\langle \hat{y}\cdot\hat{c}\rangle\langle \hat{z}\cdot\hat{c}\rangle |B_{ccc}| = N\left\langle \frac{\cos\theta - \cos(3\theta)}{8}(1-\cos(2\chi)) \right\rangle |B_{ccc}|. \tag{A-24}$$

Additional components of $\chi^{(2)}$ are accessed using different polarization combinations (e.g., $\chi_{\mathrm{yzy}}^{(2)}$ or $\chi_{\mathrm{zzz}}^{(2)}$ from *sps* or *ppp*). Ratios between these expressions can be taken to evaluate the orientational terms independently of the number density. Each tensor element $\chi_{\mathrm{ijk,q}}^{(2)}$ is a linear combination of $\langle \cos\theta \rangle$ and $\langle \cos^3\theta \rangle$ terms and takes the form:

$$\chi_{ijk,q}^{(2)} = u_{abc,q}\langle \cos\theta \rangle + w_{abc,q}\langle \cos^3\theta \rangle. \tag{A-25}$$

The coefficients $u_{abc,q}$ and $w_{abc,q}$ are related to the molecular hyperpolarizability tensors. The angular brackets reflect the orientational distribution of each oscillator and are evaluated as integrals over a distribution function, $f(\theta)$ (typically a Gaussian, as in eq. A-28). The first and third moments of the distribution function can be rewritten so that the integrals are evaluated as functions of $\langle \cos^n\theta \rangle$ to simplify the analysis.

$$\langle \cos\theta \rangle = \int_0^{\pi} \cos\theta\, f(\theta) \sin\theta \,\mathrm{d}\theta = \int_{-1}^{1} \cos\theta\, f(\cos\theta) \sin\theta \,\mathrm{d}(\cos\theta) \tag{A-26}$$

$$\langle \cos^3\theta \rangle = \int_0^{\pi} \cos^3\theta\, f(\theta) \sin\theta \,\mathrm{d}\theta = \int_{-1}^{1} \cos^3\theta\, f(\cos\theta) \sin\theta \,\mathrm{d}(\cos\theta) \tag{A-27}$$

$$f(\theta) = C\exp\left[-\frac{(\theta-\theta_0)^2}{2\sigma^2}\right] \tag{A-28}$$

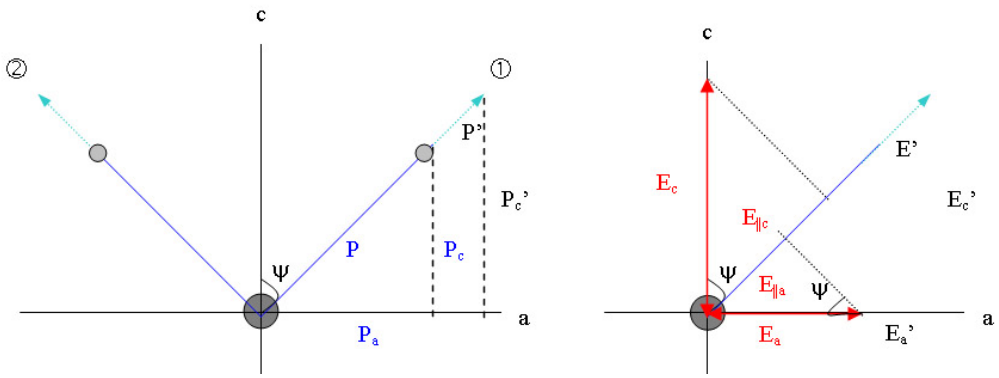

To analyze a CH_2 symmetric stretch, the molecule is treated as a combination of two C-H bonds using a bond additivity model. Here, the molecule is oriented in the *c*-*a* plane so that net dipole is directed along the *c*-axis. The geometry on the right reflects how the *c*- and *a*-components of the electric field vector (pointed out of the *c*-*a* plane and in the laboratory reference frame) act parallel to the bond.

BOND ①

$$\cos\psi = \frac{P_c}{P} = \frac{P_c'}{P'} \tag{A-29}$$

Using the subscript notation *cc* and *aa* to imply the parallel and *a*-components of the electric field, we have

$$P = \alpha_{cc} E_{\|c} \tag{A-30}$$

The geometric relationship in (29) can be substituted into (30) to give

$$P_c = P\cos\psi = (\alpha_{cc} E_{\|c})\cos\psi \tag{A-31}$$

$$E_{\|c} = E_c\cos\psi \tag{A-32}$$

Finally, using (32) to find an expression in terms of E_c

$$P_c^{(1)} = \alpha_{cc} E_c \cos^2\psi\,, \tag{A-33}$$

where the superscript on P_c explicitly indicates we are dealing with the first bond.

To treat the *a*-component of polarizability, we have:

$$\sin\psi = \frac{P_a}{P} = \frac{P_a'}{P'} \tag{A-34}$$

We find P_a as before,

$$P_a = \alpha_{aa} E_{||a} \tag{A-35}$$

$$P_a = P\sin\psi = (\alpha_{aa} E_{||a})\sin\psi \tag{A-36}$$

$$E_{||a} = E_a \sin\psi \tag{A-37}$$

$$P_a^{(1)} = (\alpha_{aa} E_{||a})\sin\psi = \alpha_{aa} E_a \sin^2\psi \tag{A-38}$$

Finding the off-diagonal contributions to the polarizability is straightforward:

$$P = \alpha_{ca} E_{||a} \tag{A-39}$$

The expression in (29) replaces *P* on the left and (37) replaces $E_{||a}$ on the right

$$\frac{P_c}{\cos\psi} = \alpha_{ca}(E_a \sin\psi) \tag{A-40}$$

Cross-multiplying gives

$$P_c^{(1)} = \alpha_{ca} E_a \sin\psi\cos\psi \tag{A-41}$$

Likewise, for the *ac* tensor,

$$P = \alpha_{ac} E_{||c} \tag{A-42}$$

The expression in (34) replaces *P* on the left and (32) replaces $E_{||c}$ on the right

$$\frac{P_a}{\sin\psi} = \alpha_{ac}(E_c \cos\psi) \tag{A-43}$$

$$P_a^{(1)} = \alpha_{ac} E_c \cos\psi\sin\psi \tag{A-44}$$

BOND ②

The second bond is simply a reflection of the first across the *a*-axis. This introduces changes in sign for components involving *a* (as we have gone from +*a* to –*a*). Consequently, the only relationships that will differ from those above are

$$P_a = -P\sin\psi \tag{A-45}$$

$$E_{\|a} = -E_a \sin\psi \tag{A-46}$$

Using the same math, we have for bond 2:

$$P_c^{(2)} = \alpha_{cc} E_c \cos^2\psi \tag{A-47}$$

$$P_a^{(2)} = \alpha_{aa} E_a \sin^2\psi \tag{A-48}$$

$$P_c^{(2)} = -\alpha_{ca} E_a \sin\psi\cos\psi \tag{A-49}$$

$$P_a^{(2)} = -\alpha_{ac} E_c \cos\psi\sin\psi \tag{A-50}$$

Finally, the expression for the total polarizability for the CH_2(s) mode is given by

$$P_c^{(CH_2,sym)} = \sum_{n=1,2} P_c^{(n)} = 2\alpha_{cc} E_c \cos^2\psi \tag{A-51}$$

$$P_a^{(CH_2,sym)} = \sum_{n=1,2} P_a^{(n)} = 2\alpha_{aa} E_a \sin^2\psi \tag{A-52}$$

Solving for α_{cc} and α_{aa}:

$$\alpha_{cc} = \frac{P_c^{(CH_2,sym)}}{2E_c\cos^2\psi} \tag{A-53}$$

$$\alpha_{aa} = \frac{P_a^{(CH_2,sym)}}{2E_a\cos^2\psi}. \tag{A-54}$$

References

(1) Shen, Y. R., *The Principles of Nonlinear Optics*; Wiley: New York, 1984.

(2) Wei, X.; Hong, S. C.; Zhuang, X. W.; Goto, T.; Shen, Y. R. *Phys. Rev. E* **2000**, *62*, 5160.

(3) Miranda, P. B.; Shen, Y. R. *J. Phys. Chem. B* **1999**, *103*, 3292.

(4) Zhuang, X.; Miranda, P. B.; Kim, D.; Shen, Y. R. *Phys. Rev. B* **1999**, *59*, 12632.

(5) Hirose, C.; Akamatsu, N.; Domen, K. *Appl. Spect.* **1992**, *46*, 1051.

(6) F.M. Fowkes, *Contact Angle, Wettability, and Adhesion*; American Chemical Society: Washington, D.C., 1964.

(7) Cole, K. C.; Guevremont, J.; Ajji, A.; Dumoulin, M. M. *Appl. Spectrosc.* **1994**, *48*, 1513.

(8) Yui, N.; Suzuki, Y.; Mori, H.; Terano, M. *Polym. J.* **1995**, *27*, *614*.

(9) Kip, B. J.; van Eijk, M. C. P. *J. Polym. Sci. B* **1991**, *29*, 99.

(10) Castner, D. G.; Ratner, B. D. *Surf. Interface Anal.* **1990**, *15*, 479.

(11) Briggs, D. *Br. Polym. J.* **1989**, *21*, 3.

(12) Brown A.; Vickerman, J. C. *Surf. Interface Anal.* **1986**, *8*, 75.

(13) *Proteins at Interfaces II: Fundamentals and Applications*; Horbett, T. A., Brash, J. L., Eds.; American Chemical Society: Washington, D. C., 1995.

(14) *Proteins at Interfaces: Physicochemical and Biochemical Studies*; Brash, J. L., Horbett, T. A., Eds.; American Chemical Society: Washington, D. C., 1987.

(15) Wang, J.; Paszti, Z.; Even, M. A.; Chen, Z. *J. Am. Chem. Soc.* **2002**, *124*, 7016.

(16) Zhang, D.; Shen, Y. R.; Somorjai, G. A. *Chem. Phys. Lett.* **2002**, *281*, 394.

(17) Opdahl, A.; Phillips, R. A.; Somorjai, G. A. *J. Phys. Chem. B* **2002**, *106*, 5212.

(18) Chen, Z.; Ward, R.; Tian, Y.; Baldelli, S.; Opdahl, A.; Shen, Y. R.; Somorjai, G. A.; *J. Am. Chem. Soc*. **2000**, *122*, 10615.

(19) Zhang, D.; Dougal, S. M.; Yeganeh, M. S. *Langmuir* **2000**, *16*, 4528.

(20) Gautam, K. S.; Schwab, A. D.; Dhinojwala, A.; Zhang, D.; Dougal, S. M.; Yeganeh, M. S. *Phys. Rev. Lett*. **2000**, *85*, 3854.

(21) Briggman, K. A.; Stephenson, J. C.; Wallace, W. E.; Richter, L. J. *J. Phys. Chem. B* **2001**, *105*, 2785.

(22) Oh-e, M.; Hong, S. C.; Shen,Y. R. *Appl. Phys. Lett*. **2002**, *80*, 784.

(23) *Polymer Handbook, 4th Edition*, Brandup, J., Immergut, E. H., Grulke, E. A, Eds.; Wiley: New York, 1999.

(24) Kim, S. H.; Opdahl, A.; Marmo, C.; Somorjai, G. A. *Biomaterials* **2002**, 23, 1657.

(25) Wang, J.; Chen, C.; Buck, S. M.; Chen, Z. *J. Phys. Chem. B* **2001**, *105*, 12118.

(26) Opdahl, A.; Somorjai, G.A. *Langmuir* **2002**, *18*, 9409.

(27) Froba, A. P.; Leipertz**,** A**.** *Int. J. Thermophys*. **2001**, *22*, 41.

(28) Wu, S. *Polymer Handbook - 4th edition*, Brandup, J., Immergut, E. H., Grulke, E. A., Eds.; Wiley: New York, 1999; p. 521.

(29) Superfine, R.; Huang, J. Y.; Shen, Y. R. *Phys. Rev. Lett.* **1991**, *66*, 1066.

(30) Ward, R. N.; Duffy, D. C.; Davies, P. B.; Bain, C. D. *J. Phys. Chem.* **1994**, *98*, 8536.

(31) Wilson, P. T.; Richter, L. J.; Wallace, W. E.; Briggman, K. A.; Stephenson, J. C. *Chem. Phys. Lett.* **2002**, *363*, 161.

(32) Wang, J.; Woodcock, S. E.; Buck, S. M.; Chen, C.; Chen, Z. *J. Am. Chem. Soc.* **2001**, *123*, 9470.

(33) Binnig, G.; Quate, C.F.; Geber, C. *Phys. Rev. Lett.* **1986**, *56*, 930.

(34) Sheiki, S. S. *Adv. Poly. Sci.* **2000**, *151*, 61.

(35) Gracias, D. H.; Zhang, D.; Lianos, H.; Ibach, W.; Shen, Y. R.; Somorjai, G. A. *Chem. Phy.* **1999**, *245*, 277.

(36) Carpick, R. W., Salmeron. M. *Chem. Rev.* **1997**, *97*, 1163.

(37) VanLandingham, M. R., Villarrubia, J. S., Guthrie, W. F., Meyers, G. F. *Macromol. Symp.* **2001**, *167*, 15.

(38) Hertz, H. *J. Reine Angew. Math.* **1881**, *92*, 156.

(39) Jhon, M. S.; Ma, S. M.; Hattori, S.; Gregonis, D. E.; Andrade, J. D. *Hydrogels for Medical and Related Applications*, Andrade, J. D., Ed.; American Chemical Society: Washington, D. C., 1976; pp 60-68.

Chapter 2

Solvent-Mediated Hydrophobic Interactions of Polymers at the Solid/Liquid Interface

2.1 Introduction

When a synthetic material is placed in a biological environment, its surface immediately interacts with the biological molecules that are present in the surrounding media. The proteins and minerals contained in the contacting interstitial fluids (i.e., in the blood and tears) can react specifically or non-specifically with the surface. Over the past 30 years, extensive efforts have been made to determine the forces influencing these reactions. A major hurdle, however, has been the inability to accurately assess, either in real time or in situ, the structure of the adsorbing or adsorbed macromolecule. This would allow us to address what biocompatibility means at a molecular level.

Proteins are intrinsically surface active and tend to concentrate at interfaces, in part because of their polymeric structure and in part because of their amphoteric nature.[1] The polar, charged, and nonpolar amino acid side chains in proteins provide multiple

modes of binding with many different types of surfaces. The thermodynamic tendency for nonpolar residues to be internalized in the native protein requires structural alterations in the protein upon adsorption in order to maximize the number of contacts with the surface.[2] Macromolecular adsorption on a hydrophobic surface, for example, involves entropically-driven conformational changes to optimize the various bonding interactions between the hydrophobic and hydrophilic sites of the protein and surface and the water phases of the interface, respectively. Real-time FTIR analysis of proteins binding to surfaces has identified conformational changes in proteins as they first adhere and then adsorb to the material;[3,4] this technique, however, has been unable to discern the specific molecular structures associated with each conformational change.

Many years of biomaterials research have focused on determining material surface characteristics, such as charge, energy, and roughness, which influence specific protein deposition. The degree of ionization and solvation of the surface and solutes and the concentration of various solutes in the surrounding media are important.[5,6] The surface energy of the material determines the thermodynamic free energy of adhesion for solutes in the surrounding media in the absence of any specific biochemical interactions.[7,8] Studies involving cells in culture have shown that positively-charged surfaces enhance cell proliferation and adhesion relative to negatively-charged or non-ionic hydrogel surfaces.[9] Other studies have shown that microscopically roughened surfaces of a given material demonstrate enhanced cell adhesion and migration rates, compared with smooth surfaces of the same material.[10, 11]

Not surprisingly, hydrophobic interactions resulting from entropy changes are also a major driving force for the aggregation of nonpolar (or amphiphilic) non-biological

molecules in aqueous solution.[12-16] Examples are found in the formation of meso-sized micelles by diblock copolymers[17] and the well-controlled formation of polymer brushes.[18, 19] In order to better understand these macroscopic phenomena, it is necessary to have systematic experimental evidence of adsorbate/substrate interactions at a molecular level. In this chapter, the factors that are involved in the alignment of model amphiphilic neutral polymers adsorbed on hydrophobic and hydrophilic surfaces are explored by SFG. These results, together with those presented in Chapter 1 concerning simpler polymer/air and polymer/liquid interfaces, establish a foundation on which to study the adsorption of more complicated macromolecules in Chapters 5 and 6.

2.2 Experimental procedures

To understand the effects of substrate hydrophobicity and solvent polarity on the ordering and orientation of adsorbed polymers at the solid/liquid interface, model polymer systems are studied under a unique SFG collection geometry. Specifically, the adsorption of amphiphilic neutral polymers, polypropylene glycol (PPG), polyethylene glycol (PEG), and a triblock PEG-PPG-PEG copolymer, from solution onto hydrophobic *per*-deuterated polystyrene (PS) and hydrophilic silica substrates (structures are presented in Figure 2.2(b)) are considered. Two different solvents, water and methanol, are used in the adsorption studies (polymer concentration of 10% w/w).

2.2.1 SFG Data Collection

SFG spectra were obtained at the solid/liquid interfaces using the experimental configuration shown in Figure 2.1. In this geometry, co-propagating visible and tunable

IR laser pulses are overlapped at the polymer/liquid interface and the induced sum-frequency signal is measured in the reflected direction. For each scan, data is collected with 200 shots/data point in 5 cm^{-1} increments in the 2775 – 3025 cm^{-1} range and normalized by the SFG intensity from a Z-cut quartz crystal measured at the sample stage. For a given condition, SFG measurements were repeated at least three times and data were averaged to produce the final spectra. The frequency of the IR beam was calibrated to ±2 cm^{-1} by the use of a polystyrene standard absorption spectrum. SFG spectra presented in this chapter were collected using the $s_{sfg}s_{vis}p_{ir}$ polarization combination.

2.2.2 Materials

Polypropylene glycol (PPG, Polysiciences, Inc.), polyethylene glycol (PEG, Polysciences, Inc.), a triblock copolymer of PEG and PPG (PEG-PPG-PEG, Aldrich-Signa), and polydiallyldimethylammonium chloride (PDDA, Aldrich-Sigma) were prepared in solution concentrations of 10.0% (w/w). All polymer solutions were prepared using deuterium oxide (D_2O, 99.9%, Cambridge Isotope Laboratories) and methanol (normal and deuterated) for control experiments. Although PEG and PDDA are soluble in D_2O, PPG and PEG-PPG-PEG form stable colloidal solutions that do not aggregate or precipitate over time. All polymers are well-dispersed in methanol.

Hydrophilic IR-grade fused silica windows (diameter 1", thickness 1/8", Esco Products) were cleaned in hot chromic acid for several hours, rinsed with copious amounts of purified water, and dried at room temperature before use. Hydrophobic polystyrene surfaces were prepared by spin-casting the polymer solutions at 3000 rpm

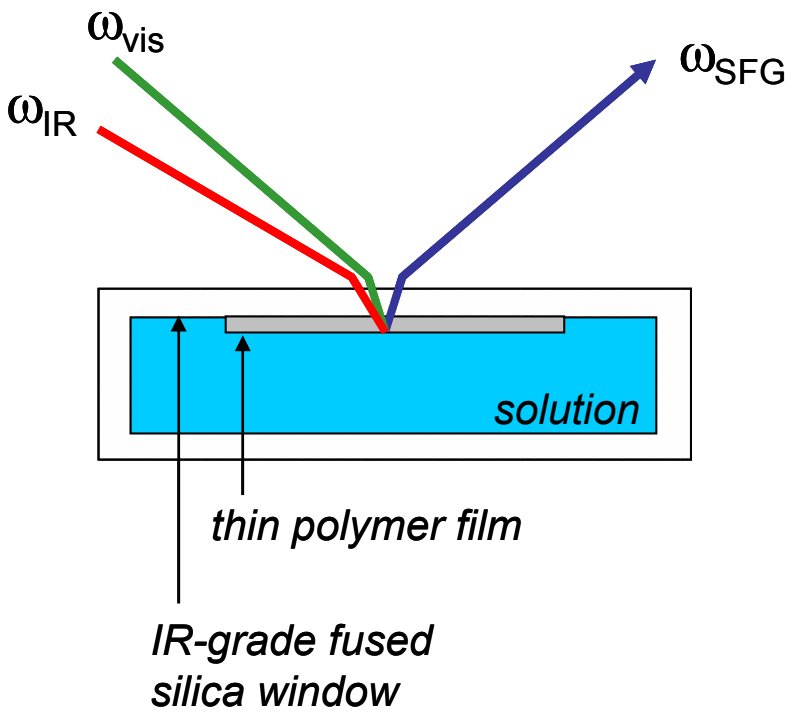

Figure 2.1: Schematic of setup used for SFG experiments at the polymer/liquid interface. The incoming beams (ω_{vis} and ω_{IR}) pass through a silica window and mix at the solid/liquid interface to generate ω_{sfg}, which is measured in a reflection geometry.

onto clean, IR-grade fused silica substrates. Polymer solutions of *per*-deuterated polystyrene (PS-d_8, MW ~ 372,000, Polymer Source, Inc.) in toluene (Aldrich, 99.8% spec. grade) were prepared with a concentration of ca. 5.0 wt %. After casting, the films were annealed at 70 °C for 12 hours and cooled at ~1.0 °C/min back to room temperature. Ellipsometry measurements and AFM topographs show the thickness of the films to be about 300 nm.

2.3 Results and discussion

2.3.1 Adsorption of amphiphilic polymers on polystyrene

In a first set of experiments, the structures of amphiphilic neutral PPG, PEG, and a PEG-PPG-PEG triblock copolymer adsorbed on hydrophobic PS surfaces were investigated at the solid/water interface. SFG spectra ($s_{sfg}s_{vis}p_{ir}$ polarization combination) in the CH-stretch region at the PS/water interface with adsorbed polymers (shown in Figure 2.2(a)). The SFG spectrum for PPG contains features around 2840, 2870, 2940, and 2970 cm^{-1}. They are assigned to the CH_2 symmetric (CH_2(s)), CH_3 symmetric (CH_3(s)), CH_3 Fermi resonance (CH_3(F)), and CH_3 asymmetric (CH_3(a)) modes, respectively.[20] Figure 2.2(a) also shows the SFG spectrum of adsorbed PEG at the PS/water interface. PEG is more hydrophilic and has a higher solubility in water, compared to PPG. This spectrum contains vibrational features centered around 2865 and 2935 cm^{-1}, corresponding to the CH_2(s) and CH_2(F) modes, respectively.[21] The result suggests that adsorbed PPG and PEG molecules adopt a conformation with their hydrophobic moieties pointing toward the PS surface at the interface.

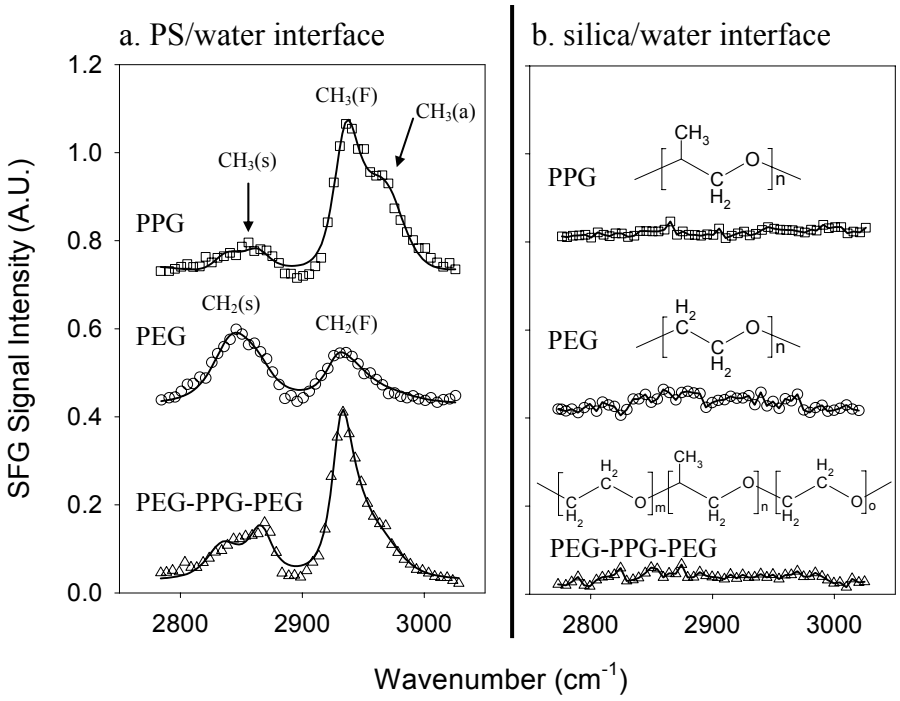

Figure 2.2: SFG spectra for adsorbed PPG (□), PEG (○), and PEG-PPG-PEG (Δ) at the (a) PS/water and (b) silica/water interfaces. The solid lines are calculated fits to the data using a Voigt function from which peak positions, widths, and oscillator strengths can be obtained. The structures of PPG, PEG, and a triblock PEG-PPG-PEG copolymer are shown in Figure 2.2(b). The intensities in the SFG spectra indicate ordering at the hydrophobic PS surface and no ordering at the hydrophilic silica surface.

The SFG spectrum for a triblock copolymer (PEG-PPG-PEG) adsorbed on hydrophobic PS surfaces contains features similar to the spectrum obtained from PPG (Figure 2.2(a)). The general structure of this class of copolymers consists of a central section of more hydrophobic PPG units flanked by less hydrophobic PEG segments. The SFG spectrum suggests that the more hydrophobic PPG center block preferentially adopts an anisotropic orientation, generating SFG, whereas the more hydrophilic PEG end blocks disorder when the triblock copolymer adsorbs at the interface. A similar molecular orientation was found for adsorbed surfactants on hydrophobic surfaces.[22]

2.3.2 Adsorption of amphiphilic polymers on hydrophilic silica surfaces

To test the role that the hydrophobic surface plays in amphiphilic neutral polymer alignment, a similar set of experiments was conducted, using a silica surface in place of PS. These results are presented in Figure 2.2(b). Clean silica is generally regarded as hydrophilic because its surface is terminated by silanol groups (Si-OH).[23] SFG spectra in Figure 2.2(b) show no spectral features for any of the polymers adsorbed at the silica/water interface. There are at least two possibilities that explain the absence of CH-stretching features in the SFG spectra: (1) no polymer adsorbs at the interface or (2) the polymer adsorbs, but the hydrophobic moieties disorder at the interface.

To confirm the presence of adsorbed polymer, SFG spectra were collected from the silica substrates after they were removed from the polymer solutions, rinsed with polymer-free water, and dried. The spectra contain CH-stretch modes consistent with the respective adsorbed polymer, as presented in Figure 2.3. The general peak positions in

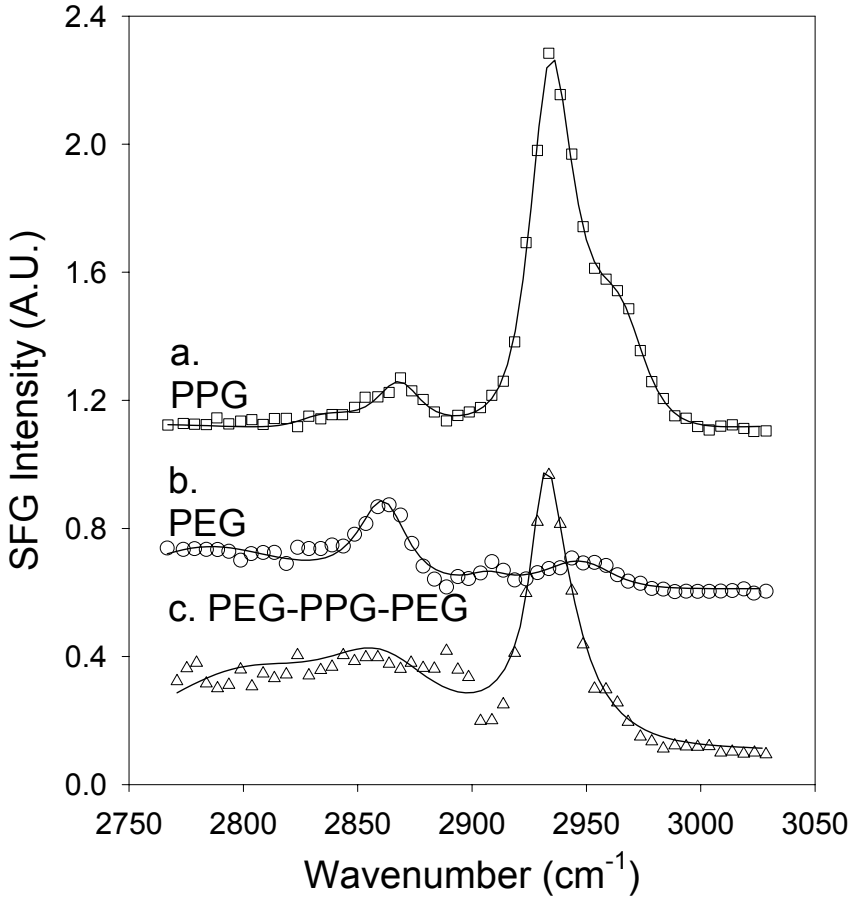

Figure 2.3: SFG spectra at the air/silica interface for (a) PPG (□), (b) PEG (○), and (c) PEG-PPG-PEG (Δ). Silica substrates were prepared by adsorption of polymer, washing, and removal of solvent.

the SFG spectrum at the polymer/air interface are comparable to those in the data at the PS/water interface in Figure 2.2(a), but the relative peak intensities are not the same, indicating that all of the polymers order, to different extents, at silica/air interfaces. This indicates that amphiphilic neutral polymers, PPG, PEG, and PEG-PPG-PEG, adsorb on hydrophilic surfaces, but that they no longer preferentially orient their hydrophobic moieties on contact with water.[21,24] Although the relative adsorption amounts of polymers on surfaces are different (e.g., ca. 0.5 and 0.3 mg/m^2 of PEG was adsorbed on PS and silica, respectively), previous studies have shown that SFG intensity is insensitive to the adsorption amount.[25] The experimental results suggest that hydrophobic surfaces are required for amphiphilic neutral polymers to order their hydrophobic moieties at the interface.

2.3.3 The role of water in polymer adsorption

In a final set of experiments, the role that water solvent plays in mediating the alignment of adsorbed polymers at the solid/liquid interface was investigated. For this purpose, polymer solutions using methanol (10% w/w) were prepared. An SFG spectrum obtained from the hydrophobic PS surface in contact with a solution of PPG in methanol is presented in Figure 2.4(a). The SFG spectrum is dominated by features from methanol (Figure 2.4(a)); the CH_3(s) and CH_3(F) modes at 2840 and 2960 cm^{-1}, respectively, are comparable to data obtained at the air/methanol interface.[26] No observable SFG signal was detected from PPG. This was confirmed by experiments using deuterated methanol, with the SFG spectrum presented in Figure 2.4(b).

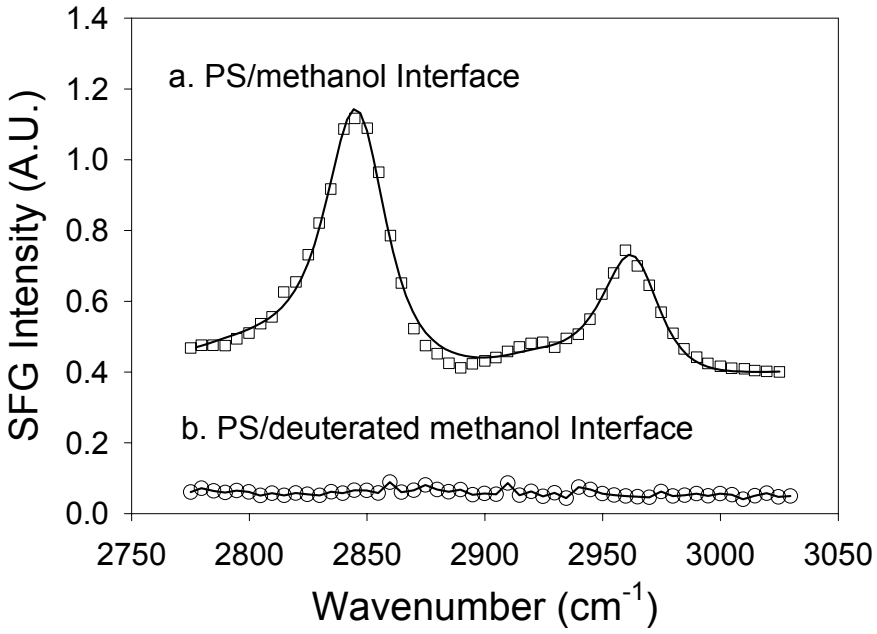

Figure 2.4: SFG spectra for PPG adsorbed at the (a) polystyrene/methanol (□) and (b) polystyrene/deuterated methanol (○) interfaces. Almost identical SFG data are obtained for PEG and the triblock copolymer. Note the absence of SFG signal from the adsorbed polymers.

At the hydrophilic silica/methanol interface, the SFG spectrum also contains features for methanol, although the peak intensity is more attenuated. Experiments using deuterated methanol show no observable SFG signal from PPG. Similar results are obtained for the other two polymers, PEG and the triblock PEG-PPG-PEG copolymer. SFG spectra obtained from the solid/air interface, after removing the substrates from the methanol solutions, are similar to those presented in Figure 2.3, within experimental error. They confirm the presence of adsorbed polymers in the interfacial regime. The results indicate that polymers at the solid/methanol solution interface are disordered regardless of the surface hydrophobicity, and that water is critical for observing interfacial ordering in adsorbed polymers.

SFG experiments were also carried out using a positively-charged polymer, polydiallyldimethylammonium chloride (PDDA), adsorbed at the PS/water, silica/water, PS/methanol, and silica/methanol interfaces. The SFG results show no evidence of ordered PDDA at any of these interfaces. Positively-charged PDDA requires other experimental conditions for it to become aligned. It has been reported that PDDA shows ordering at the silica/water interface at pH greater than 9.0, where nearly all silanol groups ($pK_a \sim 3.5$) will carry a negative charge.[27, 28]

2.4 Conclusion

SFG results indicate that hydrophobic surfaces along with water solvent are required for the anisotropic ordering of adsorbed amphiphilic neutral polymers. SFG studies have revealed that PPG, PEG, and the triblock PEG-PPG-PEG copolymer preferentially order when they adsorb at the hydrophobic PS/water interface. These

polymers are randomly oriented at hydrophilic silica/water and hydrophobic PS/methanol interfaces. From this series of experiments, it is likely that the ordering of adsorbed amphiphilic neutral polymers depends on surface hydrophobicity and solvent polarity via hydrophobic interactions. Further systematic investigations as functions of solvent composition, polymer molecular weight, and substrate hydrophobicity will paint a more complete portrait of the mechanisms which govern polymer adsorption.

References

(1) MacRitchie, R. *J. Colloid Interface Sci.* **1972**, *38*, 484.

(2) Hoffman, A. S. *Biomaterials: Interfacial Phenomena and Applications*, Cooper, S. L., Peppas, N. A., Eds.; American Chemical Society: Washington, D. C., 1982; p. 3.

(3) Castillo, E.L.; Koenig, J. L.; Anderson, J. M.; Lo, J. *Biomaterials* **1984***, 5*, 319.

(4) Pitt, W. J.; Spiegelberg, S. H.; Cooper, S. L. *Proteins and Interfaces: Physicochemical and Biochemical Studies*, Brash, J. L., Horbett, T. A., Eds.; American Chemical Society: Washington, D. C., 1977; p. 324.

(5) Schmitt, A.; Dreyer, F.; John, C. *J. Colloid Interface Sci.* **1983***, 92*, 25.

(6) Helmus, M. N.; Gibbons, D. F.; Jones, R. D. *J. Biomed. Mater. Res.* **1984***, 18*, 165.

(7) Lymann, D. J.; Muir, W. M.; Lee, I. T. ; *Transact. Am. Soc. Artif. Intern. Organs* **1965,** *XI*, 301.

(8) Absolom, D. R.; Zing, W.; van Oss, C. J.; Neumann, A. W. *Biomater. Med. Dev. Artif. Organs* **1984/85***, 12*, 235.

(9) Hattori, S.; Andrade, J. D.; Hibbs, J. B.; Gregonis, D. E.; King, R. N. *J. Colloid Interface Sci.* **1985**, *104*, 72.

(10) Lampin, M.; Werocquier-Clérout, R.; Legris, C.; Degrange, M.; Sigot-Luizard, M. F. *J. Biomed. Mater. Res.* **1997**, *36*, 99.

(11) Goodman, S. L.; Sims, P. A.; Albrecht, R. M. *Biomaterials* **1996**, *17*, 2087.

(12) Tanford, C. *The Hydrophobic Effect: Formation of Micelles and Biological Membranes*, 2nd ed.; Krieger: Malabar, FL, 1991.

(13) Zhang, X.; Zhu, Y.; Granick, S. *J. Am. Chem. Soc.* **2001**, *123*, 6736.

(14) Eisenberg, D.; McLachlan, A. D. *Nature* **1986**, *319*, 199.

(15) Raschke, T. M.; Tsai, J.; Levitt, M. *Proc. Natl. Acad. Sci. USA* **2001**, *98*, 5965.

(16) Hummer, G.; Garde, S.; García, A. E.; Pratt, L. R. *Chem. Phys*. **2000**, *258*, 349.

(17) Zhang, L.; Yu, K.; Eisenberg, A. *Science* **1996**, *272*, 1777.

(18) Park, J.-W.; Thomas, E. L. *J. Am. Chem. Soc*. **2002**, *124*, 514.

(19) *Proteins at interfaces II: Fundamentals and applications*; Horbett, T. A., Brash, J. L., Eds.; American Chemical Society: Washington, D. C., 1995.

(20) Fontyn, M.; van't Riet, K.; Bijsterbosch, B. H. *Colloids Surf*. **1991**, *54*, 349.

(21) Chen, C.; Even, M. A.; Wang, J.; Chen, Z. *Macromolecules* **2002**, *35*, 9130.

(22) Ward, R. N.; Duffy, D. C.; Davies, P. B.; Bain, C. D. *J. Phys. Chem*. **1994**, *98*, 8536.

(23) Iler, R. K. *The Chemistry of Silica*, Wiley, New York, 1979.

(24) Dreesen, L.; Humbert, C.; Hollander, P.; Mani, A. A.; Ataka, K.; Thiry, P. A.; Peremans, A. *Chem. Phys. Lett*. **2001**, *333*, 327.

(25) Chen, Z.; Ward, R.; Tian, Y.; Baldelli, S.; Opdahl, A.; Shen, Y. R.; Somorjai, G. A. *J. Am. Chem. Soc*. **2000**, *122*, 10615.

(26) Stanners, C. D.; Du, Q.; Chin, R. P.; Cremer, P.; Somorjai, G. A.; Shen, Y. R. *Chem. Phys. Lett.* **1995**, *232*, 407.

(27) Kim, J.; Cremer, P. S. *J. Am. Chem. Soc*. **2000**, *122*, 12371.

(28) Kim, J.; Kim, G.; Cremer, P. S. *J. Am. Chem. Soc*. **2002**, *124*, 8751.

Chapter 3

Viscoelastic Mechanical Properties as a Probe of Surface Water Content in Hydrogels

3.1 Introduction

We now turn our attention to an actual polymeric biomaterial: the soft contact lens. As part of the hydrogel family, contact lenses are insoluble, cross-linked polymer networks swollen in water and have been used for vision correction for over 30 years. In spite of the many advances that have been made to improve the comfort and biocompatibility of contact lenses, their interfacial properties are not well understood. An example is the hydration state of the surface region of a contact lens.[1] It is commonly observed that the bulk water content affects both the oxygen permeability and the mechanical properties of a hydrogel – and consequently affects overall lens comfort.[2] At the contact lens surface, it is believed that a high water content and high surface hydrophilicity are desirable properties, in order to increase the wettability of tear

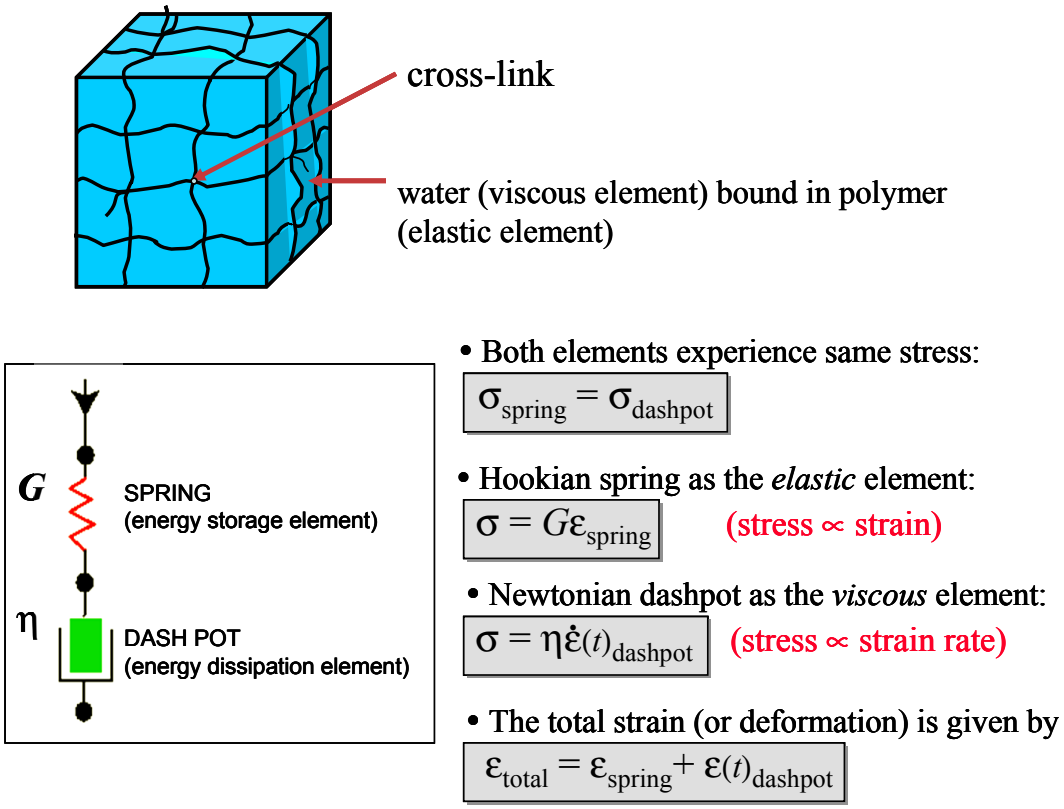

Figure 3.1: Diagram of the viscous and elastic properties of a hydrogel. Viscoelasticity can be mathematically treated as a spring and dashpot connected in series (other combinations, including those is parallel, exist).

films.[3] Although many strategies have been developed to increase surface hydrophilicity,[2] measurements of the water content of the surface region have not been made and the concentration of water at the surface, relative to the bulk water content, is uncertain.

The surface water content is particularly important for understanding the comfort-related properties of poly(hydroxyethyl)methacrylate [poly(HEMA)] based contact lenses, where oxygen permeability increases as the bulk water content increases.[2] These types of lenses tend to dehydrate when they are on the eye,[4] and if the water content at the hydrogel/air interface is significantly less than the bulk water content due to dehydration, then oxygen diffusion may be limited at the interface. The water content of the near-surface region also affects the surface mechanical properties – including viscoelasticity and friction – of poly(HEMA), which is rigid and glassy in its dry state but is soft and flexible in its fully-hydrated state.

AFM has been shown to be capable of characterizing the surface mechanical properties of fully-hydrated poly(HEMA) hydrogels.[5] In an effort to better understand the role of dehydration at the hydrogel/air interface, this chapter presents a method for characterizing the mechanical properties of bulk-hydrated poly(HEMA) hydrogels as a function of humidity, at the hydrogel/air interface. Increasing or decreasing the humidity changes the rate of dehydration from the surface and changes the viscoelastic mechanical response of the surface (see Figure 3.1). Thus, measurements of the surface mechanical properties can be related to the water content of the surface region. In these experiments, AFM is used to probe the adhesive and viscoelastic properties of poly(HEMA) hydrogels to a depth of up to 150 nm.

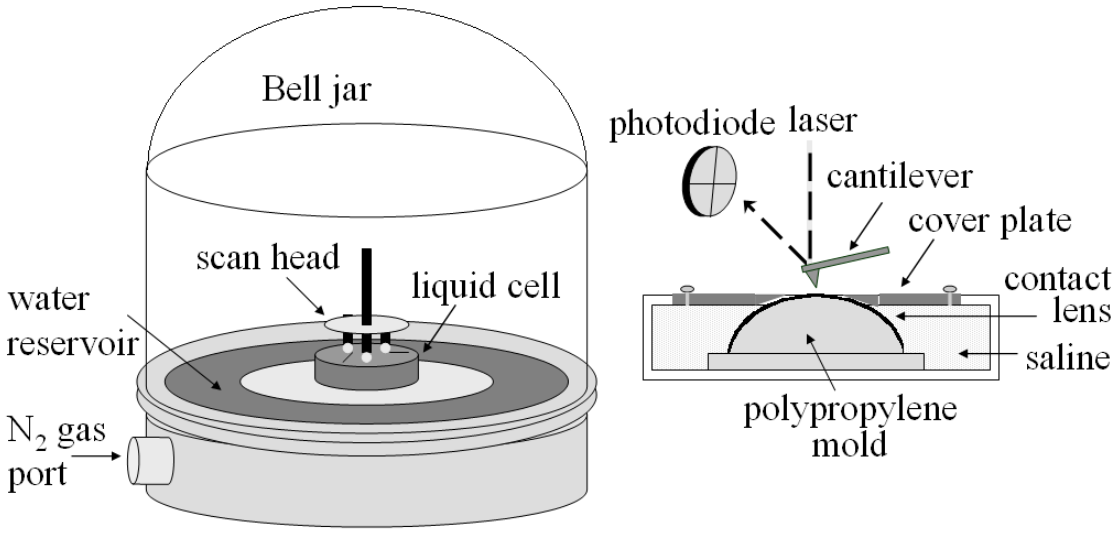

Figure 3.2: Schematic view of the AFM instrument used to measure the surface mechanical properties of hydrogels as a function of humidity. Relative humidity inside the bell jar increases as water evaporates from the reservoir and is maintained by adjusting the flow rate of low-humidity nitrogen gas through the bell jar. On the right is a close-up view of the sample stage, showing a contact lens sitting on a polypropylene mold, saline reservoir, and stainless steel cover plate.

3.2 Experimental procedures

3.2.1 Materials

The commercial hydrogel contact lenses used in this study were made of a homopolymer of 2-hydroxyethyl methacrylate, poly(HEMA), (Polymacon^{TM}, Ocular Sciences, FDA Group-I) and were cross-linked using ethylene glycol dimethacrylate as the cross-linking agent. The lenses were polymerized in a polypropylene mold. When swollen in saline solution (0.15 M NaCl, buffered at pH = 7), the poly(HEMA) lens contains 38% water (wt/wt). The lenses received no further surface treatment and were thoroughly washed with fresh saline solution prior to AFM measurements.

3.2.2 AFM data collection and analysis methods

The AFM experimental setup is shown in Figure 3.2 and is designed to mimic, as closely as possible, an ocular environment.[5] The homebuilt walking-style AFM scanning head, controlled by RHK electronics, is enclosed within a 30-L glass bell jar.[6] The contact lens is supported on a polypropylene mold, immersed in saline solution, and covered by a stainless steel cover plate. The cover plate was machined to have an inside curvature of 8.6 mm and an outside orifice diameter of 4 mm. The inside curvature secures the contact lens without distortion and the outside orifice allows AFM measurements of the contact lens surface exposed to air.

The air-exposed surface region of the hydrogel reaches a steady-state condition, where water evaporation from the hydrogel surface is equilibrated with water replenishment by diffusion from the bulk. In subsequent discussion, this type of hydrogel

Bulk hydrated (bulk mod. 0.3 MPa)			Bulk dehydrated (bulk mod. 1 GPa)		
Rel. humidity	Surface stiffness, N/m	Surface elastic mod., MPa	Rel. humidity	Surface stiffness, N/m	Surface elastic mod., MPa
43%	0.76±0.02	45±7	40%	1.03±0.02	>70
50%	0.73±0.02	35±7	50%	1.02±0.03	>70
63%	0.68±0.03	25±7	68%	0.99±0.02	>70
75%	0.68±0.02	25±7	85%	1.01±0.02	>70

Table 3.1: Average stiffness (*S*) and elastic modulus values at various relative humidities for bulk-hydrated and dehydrated hydrogels. A stiffness value of 1 N/m represents the limiting value that can be measured with a 1 N/m cantilever. Elastic modulus values are presented only as order of magnitude estimates.

is referred to as *bulk-hydrated*. For comparative purposes, AFM experiments were also performed on dehydrated hydrogels – where there is no saline solution in the reservoir. For these experiments, the contact lens was placed on a polypropylene mold and allowed to dry overnight under ambient conditions prior to AFM measurement. This type of hydrogel is referred to as *bulk-dehydrated*.

Relative humidity was controlled by competition between the evaporation of water from a secondary reservoir in the bell jar and the flow of low humidity nitrogen gas through the bell jar. After adjusting the humidity, the hydrogels were allowed to stabilize for 30 minutes prior to AFM measurement. The surface region of the bulk-hydrated hydrogel swells when the humidity is increased and contracts when the humidity is decreased. The swelling and contraction of the surface is easily monitored with the AFM. When the surface stops 'moving' toward or away from the AFM cantilever, it is assumed that steady state has been reached. Typically, this was found to take only a few minutes after stabilization of the humidity and was also assessed by evaluating the reproducibility of force vs. distance (f-d) curves over time.

Force vs. distance curves were obtained by recording the normal deflection signal of the cantilever (force constant 1 N/m, silicon nitride tip, ND-MDT) during the tip approach (loading) and retract (unloading). The detector signal was calibrated by adjusting the slope of the f-d curve measured against a reference surface to the nominal spring constant of the cantilever. A hydrophilic glass surface was used as a reference and was prepared by treating a glass slide with Piranha solution (9 parts of conc. H_2SO_4 and 1 part of 30% H_2O_2).

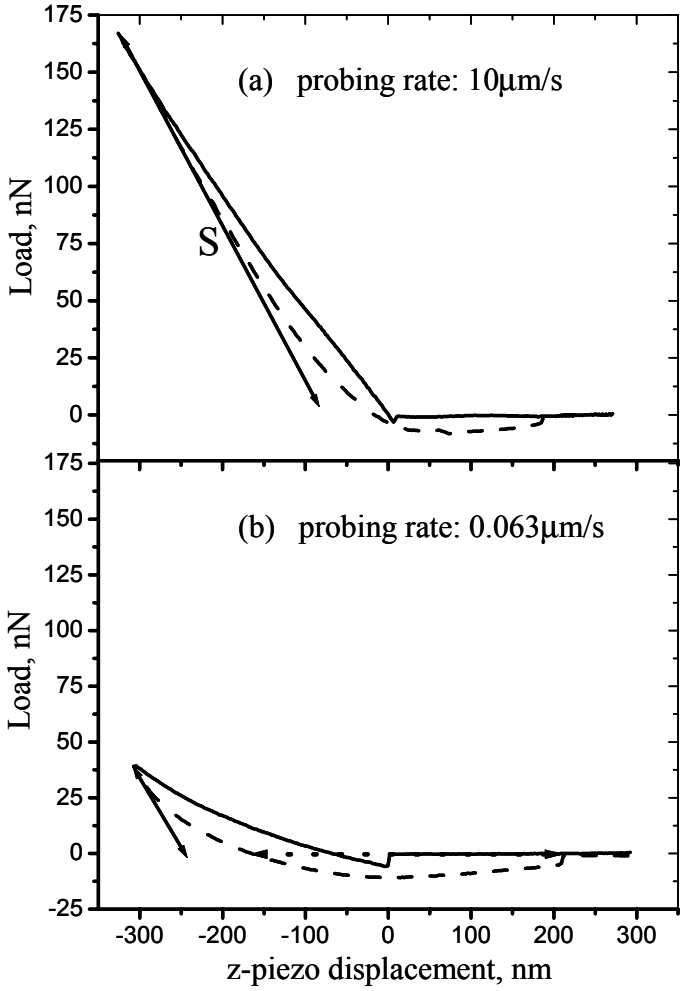

Figure 3.3: Comparison of AFM load vs. *z*-piezo travel distance (force vs. distance) curves collected at (a) fast and (b) slow probing rates on a bulk-hydrated poly(HEMA) hydrogel (75% relative humidity). The solid line is the approach (loading) curve, the dashed line is the retract (unloading) curve, and the solid arrow line represents the best-fit slope of the initial part of the retraction curve (the stiffness). Curve (b) collected at 0.063 μm/s reaches a lower maximum load, indicating viscous relaxation of the polymer dominates the deformation of the hydrogel surface at slow probing rates.

Typical force (load) vs. distance curves are shown in Figure 3.3 and measure the dependence of AFM cantilever bending on the motion of the piezoelectric actuator. The f-d curve contains information related to the elastic, viscous, and adhesive properties of the hydrogel surface. As the piezoelectric actuator presses the AFM tip against the hydrogel surface, there are three major deformation components: bending of the cantilever (the load), elastic strain of the hydrogel, and viscous strain of the hydrogel. When the cantilever is initially retracted from the surface, the viscous strain component is minimized and the primary deformation components are recovery of the cantilever bending and elastic recovery of the hydrogel. Thus, the difference between the loading and unloading curves qualitatively reflects the magnitude of the viscous strain component.

The stiffness, *S*, is defined here as the initial slope of the unloading curve and contains all of the elastic deformation information (from both the cantilever and the hydrogel recovery).[7] If a contact model is assumed, then the elastic modulus can be estimated from the stiffness value. The Hertz model has been used as a first approximation to describe the contact area in our calculation of elastic modulus.[7] Since this type of contact model neglects adhesive effects and underestimates the true contact area, the elastic modulus values reported are overestimates of the true values and are presented only to show the approximate magnitude of the surface elastic modulus. Additional details of the procedure used for transforming stiffness values into elastic modulus can be found in reference 8.

The measurement of the viscous component has a strong time dependence associated with it, whereas the hydrogel elastic strain and cantilever bending have little or

no time dependence.[9] The contribution of the viscous strain component to the deformation process can be assessed as a function of piezoelectric actuator driving rates. F-d curves were collected at actuator drive rates from 0.06 to 20 μm/s. The two force curves in Figure 3.3 were collected at actuator rates of 0.06 and 10 μm/s and highlight the time dependence of the viscous strain component. The loading curve collected at 0.06 μm/s reaches a lower maximum load than the curve collected at 10 μm/s, indicating that the cantilever bends less and the tip sinks more deeply into the surface under slow probing rates. Collecting force curves at faster and faster rates decreases the magnitude of the viscous component in the deformation process, until it is not detectable in the f-d measurement.

3.3 Results

3.3.1 Stiffness and elasticity

Loading and unloading slopes extracted from the f-d curves of the bulk-hydrated and bulk-dehydrated hydrogels at probing rates between 0.06 μm/s to 20 μm/s are shown in Figures 3.4(a) and (b), respectively. The average stiffness (*S*), as a function of humidity for both the bulk-hydrated and dehydrated hydrogels, is presented in Table 3.1. The corresponding elastic modulus values calculated from the stiffness values are also presented in Table 3.1. A stiffness value of 1 N/m represents the highest value that can be measured with the 1-N/m cantilever used in the experiments and indicates that the hydrogel surface was not measurably deformed. A stiffness value of zero reflects complete compliance of the hydrogel (no cantilever bending). Using the procedure

outlined in reference 8, these stiffness limits of the 1-N/m cantilever translate into a sensitivity range of elastic modulus values that are between 10 and 70 MPa.

The stiffness is independent of the measurement rate for both bulk-hydrated and bulk-dehydrated hydrogels. Additionally, the stiffness of the bulk-dehydrated hydrogel remains relatively constant as the humidity is increased. Since the stiffness values of the bulk-dehydrated hydrogel saturate the scale at ~1 N/m, the calculated minimum surface elastic modulus is at least 70 MPa. The elastic modulus is likely much greater than this and is probably similar to the bulk value obtained from dry poly(HEMA) (~1 Gpa), suggesting that the surface of bulk-dehydrated poly(HEMA) exposed to moderate humidity is in a glassy state.

In contrast, the stiffness of the bulk-hydrated hydrogel at 45% relative humidity is measurably lower than the stiffness of the bulk-dehydrated hydrogel at 45% relative humidity. At low relative humidity (~45%), the surface stiffness is 0.76 N/m and the calculated surface elastic modulus is 45 MPa – intermediate to the elastic modulus of totally-dehydrated poly(HEMA) and totally-hydrated poly(HEMA). This indicates that at low humidity, dehydration from the surface is still a significant factor and that the air-exposed surface is stiffer than the bulk of the hydrogel.

As the humidity increases, there is a slight decrease in the stiffness of the surface. At 75% relative humidity, the stiffness decreases to 0.68 N/m, which corresponds to an elastic modulus of 25 MPa. This behavior is consistent with an increase in the water content at the surface, which softens the lens. At room temperature, dry poly(HEMA) is below its glass transition temperature, 50-80°C,[10] and is in a mechanically rigid state.

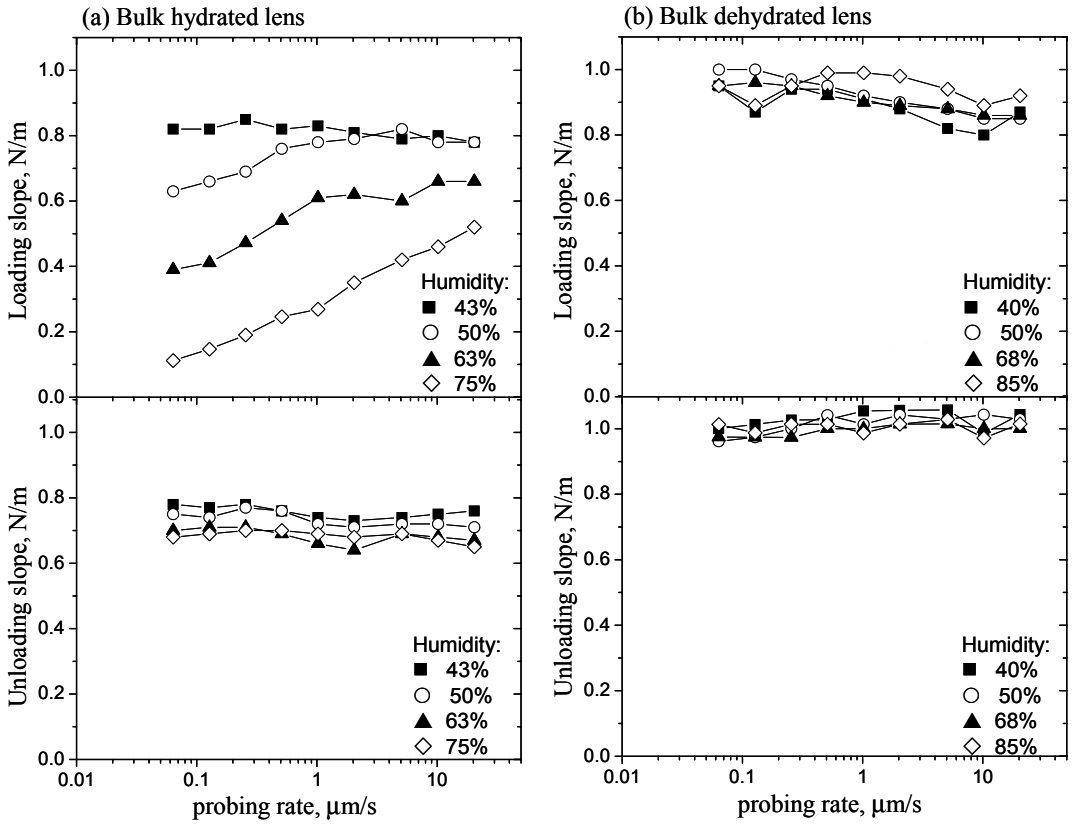

Figure 3.4: Comparison of loading and unloading curve slopes for (a) bulk-hydrated and (b) bulk-dehydrated hydrogels collected at various probing rates and humidity (1-N/m cantilever). The loading curve slope contains contributions from both elastic and viscous deformations while the unloading curve slope contains mainly elastic contributions. The loading curve slope of the bulk-hydrated decreases and has a strong dependence on probing rate at high humidity, indicating an increased presence of water in the surface region.

Water acts as a solvent and plasticizes the surface of the hydrogel. Even though the surface softens as the humidity increases, it is still much stiffer than the surface of the totally-hydrated hydrogel, which has been measured by AFM to have a value ~1.3 MPa.[5] This indicates that even at high humidity, the dehydration rate of the interface is sufficient to affect the mechanical properties of the hydrogel surface.

3.3.2 Viscous behavior

The viscous behavior of the bulk-hydrated hydrogel surface, qualitatively assessed from the loading curve slopes presented in Figure 3.4, also suggests that the concentration of water in the near-surface region increases as the humidity increases. A smaller value of the loading curve slope, and larger differences between the slopes of the loading and unloading curves at a particular probing rate, indicate larger viscous effects.

The loading curve slope is extremely sensitive to changes in humidity. At 45% humidity, there is no measurable difference between the loading and unloading slopes, indicating little viscous deformation of the surface. When the relative humidity is increased above 60%, the magnitude of the viscous deformation increases. The AFM tip sinks further into the surface to reach a given load. This effect is most noticeable at the slower probing rates, which give the hydrogel more time to relax; this makes it more sensitive to the viscous deformation component. The increased viscous behavior indicates that the near-surface region retains more water at high humidity and is consistent with the stiffness measurement, which shows that the surface region softens at high humidity.

In contrast, the loading and unloading slopes presented in Figure 3.4 are very similar for the bulk-dehydrated hydrogel, indicating that the dehydrated hydrogel

undergoes little viscous deformation as a function of humidity. This is consistent with the data for the elastic behavior of the dehydrated hydrogel, which shows that the dehydrated hydrogel remains rigid as the humidity increased. The combination of elastic and viscous data is a strong indication that very little water is present at the surface of the bulk-dehydrated hydrogel – even at high humidity.

It is noted that a detailed calculation of the surface viscosity is not possible using the type of data presented here. In a typical viscosity measurement, the material is held under a fixed loading rate or a fixed strain rate. The AFM f-d measurement is neither a fixed load nor a fixed strain experiment. Although the piezoelectric actuator moves at a fixed rate, the material strain rate varies throughout the experiment.

3.3.3 Adhesive behavior

When the cantilever retracts from the surface, there is an adhesive interaction between the AFM tip and the hydrogel surface. Figure 3.5(a) and (b) show plots of the adhesive snap-out interaction distances as a function of humidity for the bulk-dehydrated and bulk-hydrated hydrogels, collected at a probing rate of 5 μm/s. For force curves collected at slower rates, the snap-out adhesion values are larger, and for faster rates they are lower. The same behavior is observed for the adhesive jump-to-contact force on the loading curve, and is consistent with the work done by Basire et al. on styrene-butadiene copolymers showing that, for soft viscoelastic materials, snap-in adhesive interactions increase as function of measurement time.[11]

The adhesive interactions have no measurable dependence on humidity for bulk-

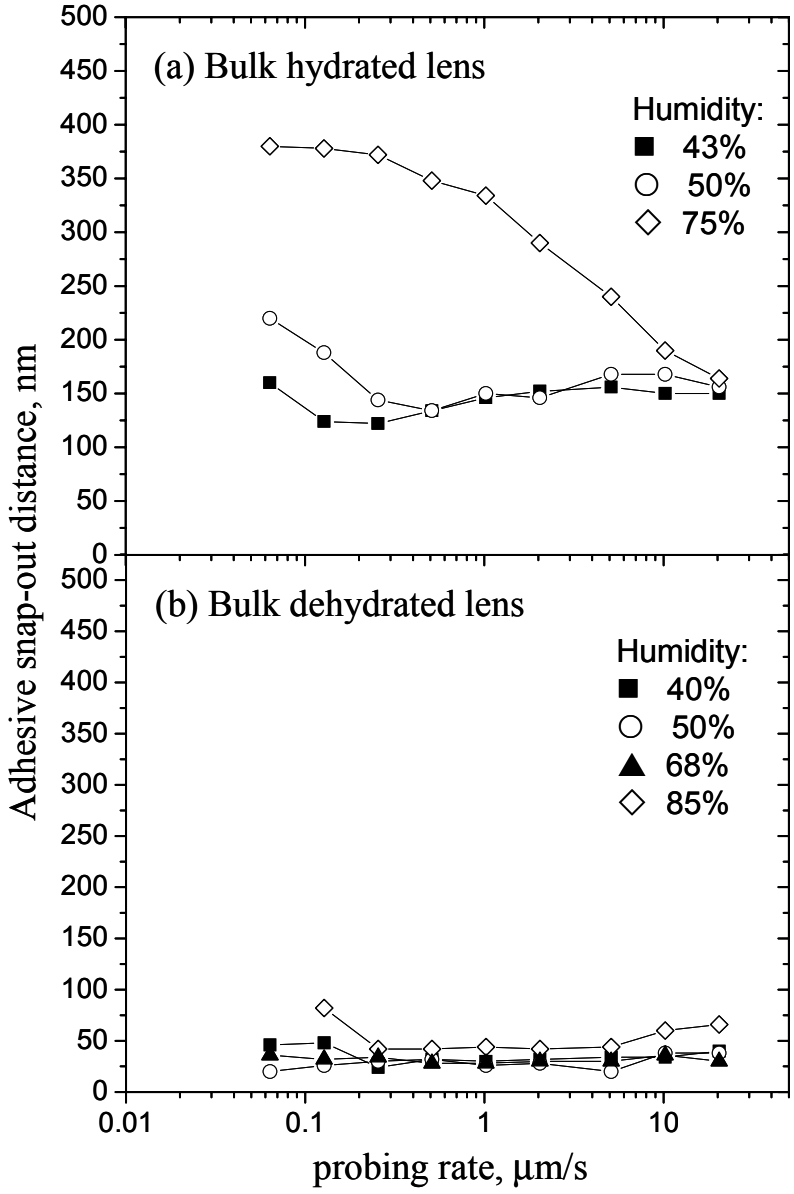

Figure 3.5: Adhesive snap out distance vs. loading rate for (a) bulk-hydrated and (b) bulk-dehydrated hydrogels. The snap-out distances measured on the bulk-dehydrated hydrogel are small for all humidity values and probing rates. The snap out distances while it increases as humidity increases for the bulk-hydrated hydrogel.

dehydrated hydrogels. However, the snap-out adhesive interactions increase in magnitude as the humidity increases for the bulk-hydrated hydrogels. As the hydrogel softens at high humidity, the tip probes more deeply into the surface; this may lead to an increase in the contact area. Additionally, the AFM tip may be pulling material out from the surface as it retracts.[12] That the adhesive properties of the bulk-dehydrated hydrogel show no humidity dependence confirm that there is very little water in the surface region. It also indicates that there is not a layer of water condensing at the surface of the bulk-dehydrated hydogel at high humidity – which would lead to humidity-dependent adhesive behavior from capillary interactions between the AFM tip and the adsorbed water.

3.4 Discussion

The adhesive and viscoelastic properties reported here suggest that the surface mechanical properties and surface water content of poly(HEMA) hydrogels are strongly dependent on the state of bulk hydration and on the relative humidity of the environment. The surface region of a bulk-dehydrated hydrogel remains stiff and dry at all values of humidity measured in these experiments. The surface region of a bulk-hydrated hydrogel is dry under ambient humidity, but becomes softer and contains more water as the humidity is increased – due to a decrease in the rate of dehydration. Figure 3.6 presents the humidity dependencies of surface viscoelasticity for the bulk-hydrated and bulk-dehydrated hydrogels. This plot shows the minimum rate that the AFM loading curves need to be collected at in order to be insensitive to viscous strain effects as a function of humidity. The *minimum actuator rate* is taken as the rate at which the loading curve

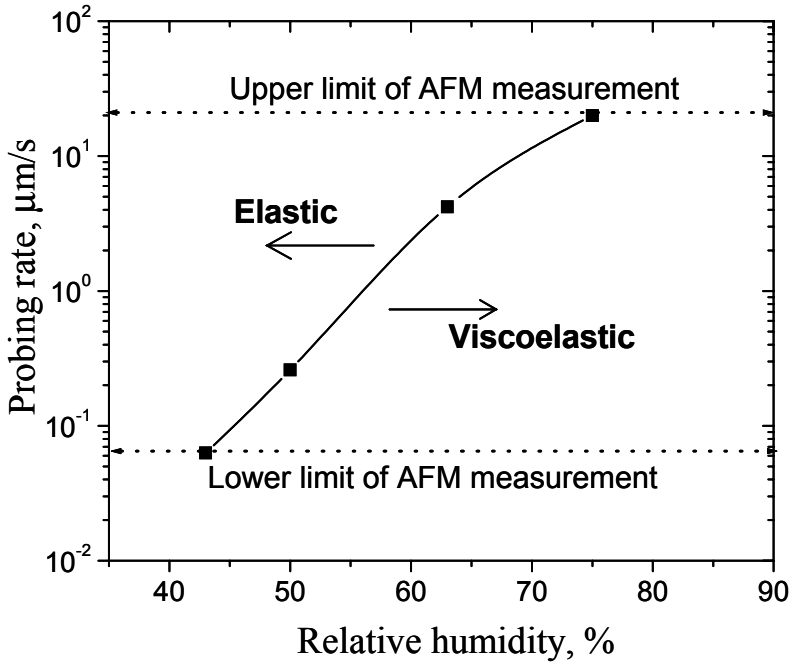

Figure 3.6: Plot of the minimum probing rate needed to remove viscous strain effects from the force vs. distance curves of bulk-hydrated hydrogels as a function of humidity. The surface of a bulk-dehydrated hydrogel is rigid at all measured humidity values. The surface of a bulk-hydrated hydrogel is rigid at ambient humidity but softens when the humidity increases above ~60%.

slope no longer increases – where there is no apparent viscous deformation of the hydrogel surface. For the bulk-dehydrated hydrogel, the surface viscoelastic behavior has no measurable dependence on humidity. In order to be sensitive to possible changes in surface viscoelasticity of the dehydrated hydrogel, force curves would need to be collected at much slower rates or the temperature of the sample would need to be raised.

The stiff surface region measured at all humidities is consistent with water absorption measurements made on poly(HEMA) as a function of humidity, which suggest that although increasing the humidity of the air increases the bulk water content, the largest increases in absorbed water occur do not occur until the relative humidity is above 80−90%.[13]

For the bulk-hydrated hydrogel, at low relative humidity, the surface behaves much like the bulk-dehydrated hydrogel. As the humidity increases, however, the AFM measurement must probe the surface faster and faster in order to become insensitive to the viscous relaxation of the bulk-hydrated hydrogel surface. The greatest change in the viscous behavior is measured between 60% and 85% relative humidity. This suggests that a decreased rate of dehydration increases the water content of the surface region and softens the poly(HEMA) surface.

From a practical standpoint, these results indicate that the air-exposed surfaces of methacrylate-based hydrogels are likely to be quite dry and rigid, and also stiffer than the bulk material. The increased stiffness may affect the interaction between the contact lens and the eyelid and may affect the overall lens movement on the eye. It should be noted that these experiments do not take into account important biological factors such as the presence of protein material at the surface, which has been shown to change the

wettability of the surface[14] or the presence of rewetting tear films. In spite of this, dehydration from the hydrogel has been shown to be a significant factor in controlling the mechanical properties of the surface region.

3.5 Conclusion

Changes in the surface viscoelastic and adhesive properties of bulk-hydrated and dehydrated poly(HEMA)-based hydrogels were monitored as a function of humidity by AFM. Stiffness, elastic modulus, viscous deformation, and adhesion data extracted from AFM force vs. distance interaction curves indicate that the surfaces of bulk-dehydrated hydrogels are dry at humidities up to 85% and that there is very little net diffusion of water into the bulk. For bulk-hydrated hydrogels, the surfaces are rigid and dry under ambient humidity and soften dramatically at ~60% relative humidity, indicating an increased presence of water, which plasticizes the surface layer. This method can be used to compare the surface water content of various hydrogel classes and to test the effectiveness of various surface treatments on hydrogel materials that attempt to enhance the water content of the surface region.

References

(1) McConville, P.; Pope J. M. *Polymer* **2001**, *42*, 3559.

(2) Lai, Y. C.; Friends G. D. *J. Biomed. Mat. Res.* **1997**, *35*, 349.

(3) Lopez-Alemany, A.; Compan, V.; Refojo, M. F. *J. Biomed. Mat. Res. (Appl. Biomater.)* **2002**, *63*, 319.

(4) Pritchard, N.; Fonn, D. *Opthal. Physiol. Opt.* **1995**, *15*, 281.

(5) Kim, S. H.; Marmo, C.; Somorjai, G. A. *Biomaterials* **2001***, 22*, 3285.

(6) Gracias, D. H.; Zhang, D.; Lianos, L.; Ibach, W.; Shen, Y. R.; Somorjai, G.A. *Chem. Phys.* **1999**, *245*, 277.

(7) Pharr, G. M.; Oliver, W. C. *MRS Bulletin* **1992**, *17*, 28.

(8) Opdahl, A.; Somorjai, G.A. *J. Polymer Science B-Polymer Physics* **2001**, *39*, 2263.

(9) Ferry, J. D. *Viscoelastic properties of polymers*, 3rd edition; New York: Wiley, 1980.

(10) Peyser, P. "Glass Transition Temperatures of Polymers," in *Polymer Handbook*; Brandup, J., Ed.; Wiley: New York, 1989.

(11) Basire, C.; Fretigny, C. *Trib. Lett.* **2001**, *10*, 189.

(12) Bliznyuk, V. N.; Assender, H. E.; Briggs, G. A. D. *Macromolecules* **2002**, *35*, 6613.

(13) Refojo, M. F. *Hydrogels for Medical and Related Applications*, Gould, R. F., Ed.; American Chemical Society: Washington, D. C.; 1976, pp 37-51.

(14) Holly, F. J.; Refojo, M. F. *Hydrogels for Medical and Related Applications*; Gould, R. F., Ed.; American Chemical Society: Washington, D. C., 1976; pp 267-282.

Chapter 4

The Effect of Equilibrium Bulk Water Content on the Surface Mechanical Properties of Hydrogels as a Function of Humidity

4.1 Introduction

The surface chemistry of hydrogels is a critical factor in determining the comfort of their use as contact lenses. As we saw in Chapter 3, this is primarily because it dictates the equilibrium water content and mechanical properties at both the lens/air and lens/eye interfaces.[1,2] Consequently, hydrogel surface chemistry must be controlled in order to tune the interfacial water content, lubricate against the shearing action of the eyelid, and ensure a biocompatible response.[3,4] The experiments in the previous chapter demonstrated that the chemical composition and water content near the hydrogel surface, however, are altered on exposure to external environmental variables (e.g., humidity or temperature).[1,5] As the interfacial water content re-equilibrates with changes in the

environment, the surface mechanical properties of the hydrogel will be affected; changes in the surface mechanical response reflect the degree of interfacial hydration.

Water not only influences surface stiffness and tribology, it is also involved in the biodeposition of protein and lipid from tear fluid, mediates oxygen transport to the cornea, and promotes the dimensional stability of the lens.[6-9] Thus, losses in interfacial water content compromise mechanical and physiological performance and lead to decreases in visual acuity – all issues of major concern to contact lens wearers. While many synthetic strategies are aimed at improving lens comfort, the state of bulk and interfacial hydration and its impact on surface mechanics is not well understood.[10-12]

Synthetic hydrogels for biomedical use were developed during the 1960s, with derivatives of hydroxyethyl methacrylate (HEMA) remaining the most popular contact lens materials.[13,14] Cross-linked poly(HEMA) networks are soft and flexible materials, possessing excellent mechanical and optical properties. Figure 4.1 displays the chemical structures of poly(HEMA) and its more hydrophilic copolymer derivative, poly(HEMA) copolymerized with methacrylic acid (poly(HEMA+MA)). The ionic nature of methacrylic acid increases the equilibrium water content in the bulk from 38 to 55%, by weight. Bulk water content is often adjusted via the hydrophilicity of the polymer material or by the degree of covalent cross-linking between polymer chains.[15]

When completely dehydrated at room temperature, poly(HEMA) contracts and adopts a rigid and glassy state, as it is below the glass transition temperature, T_g, (50−80ºC).[16] Water both plasticizes the hydrogel surface and facilitates gas transport – functions essential for a clinically safe and comfortable experience. The water content of hydrogels is that measured when completely immersed in saline solution; in this

environment, the surface water content of the hydrogel is identical to that of the bulk. When placed on the eye, however, contact lenses lose a substantial amount of interfacial water.[17] A gradient between the bulk and surface is rapidly established as the water in the hydrogel equilibrates with that in the air. Recall that the thickness of the interfacial water layer depends on both the atmospheric humidity and bulk water content of the hydrogel, which is determined by the polymer chemistry. [5]

Contact lenses with increasingly hydrophilic character have been developed to improve water retention in the bulk and at the surface. Despite possessing lower friction coefficients and weaker adhesion forces, clinical and experimental studies have revealed that high water content lenses are prone to rapid dehydration.[2,18] These surfaces require an excellent tear film quality to remain in steady-state hydration, otherwise corneal desiccation will occur. That is, water will be drawn from the eye at the posterior surface of the lens to replace that lost to evaporation at the anterior surface.[19,20] Blinking helps to restore the tear film, but, as the ambient humidity falls, the time needed for film break-up to occur shortens.

An enrichment or depletion in surface water content can be gauged by an analysis of the deformation experienced by a hydrogel under the tip of an AFM. This deformation is a combination of the viscoelastic deformation of the polymer chains and the viscous compression of the surrounding water.[5,12] The experiments described in these studies are performed under controlled humidity and simulate both the aqueous ocular environment and variable water content of the air. Specifically, data involving the humidity dependence of the surface stiffness, viscoelasticity, compliance, and stress-relaxation

(a)

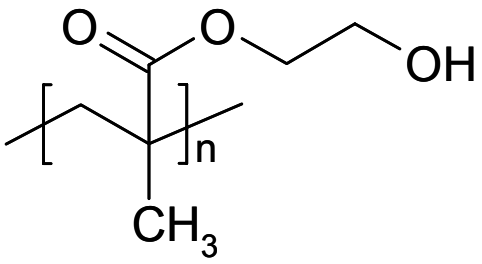

(b)

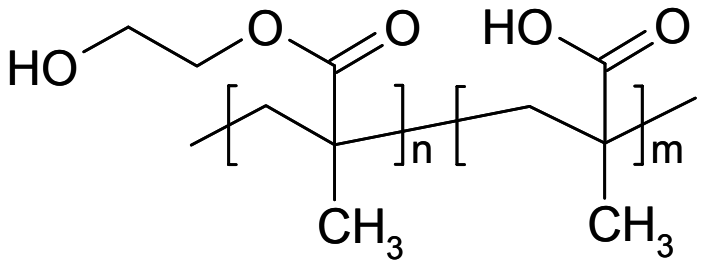

Figure 4.1: Chemical structures of (a) poly(2-hydroxyethyl methacrylate) (poly(HEMA)) and (b) poly(HEMA) copolymerized with a small amount (n << m) of methacrylic acid (poly(HEMA+MA)). The bulk water contents of the hydrogel contact lenses are 38 and 55% (w/w), respectively.

time of hydrogels under a particular load are readily obtained from AFM load vs. displacement plots. The study in Chapter 3 probed changes in the surface mechanical response of hydrogels as a method to gauge changes in interfacial water content as a function of humidity.[5] Here, the humidity dependence of the surface mechanical properties is used to determine how *bulk hydrophilicity* affects interfacial hydration.

4.2 Experimental procedures

4.2.1 Materials

The two types of commercial hydrogel contact lenses in this study are based on a homopolymer of 2-hydroxyethyl methacrylate, poly(HEMA), (Polymacon^{TM}, Ocular Sciences, FDA Group-I), shown in Figure 4.1(a). The lenses were produced through a cast-mold process. The cast mold was made by injection-molding polypropylene into a stainless steel master mold. Ethylene glycol dimethacrylate (0.5 wt%) was used as a cross-linker for poly(HEMA). When swollen in saline solution (0.15M NaCl, buffered at pH = 7), the poly(HEMA) lens retains 38% water (wt/wt). The second lens, a derivative of poly(HEMA), is made by copolymerization in the presence of a small amount of methacrylic acid. The chemical structure of poly(HEMA+MA) (Ocufilcon D^{TM}, Ocular Sciences, FDA Group-II) is shown in Figure 4.1(b). With the addition of this hydrophilic monomer, the bulk water content increases to 55% (wt/wt). The lenses, sealed in containers with buffer solution, received no further surface treatment and were thoroughly washed with fresh saline solution prior to AFM analysis.

4.2.2 AFM experimental setup

The same instrument used to perform the experiments in Chapter 3 is used here. It is a homebuilt, walking-style AFM scanning head, controlled by RHK electronics (Troy, MI), which is enclosed within a 30-L glass bell jar.[21] Relative humidity (RH) is varied by balancing the evaporation of water from a reservoir within the jar with a steady flow of dry nitrogen through the chamber. Decreasing the flow rate of nitrogen increases the experimental humidity, which is read measured by a digital hydrometer placed within the chamber. The humidity directly above the hydrogel will differ somewhat from the measured ambient humidity due to local water transport at the surface. While a dependence exists between the local and ambient humidity, there is no simple way to relate the two.

In contact lenses, water (de)hydration is regulated at two regions: the lens/air interface and the lens/eye interface. Bulk rehydration of saline provided by the eye normally offsets evaporation occurring at the air interface. The steady-state water gradient established between the surface and the bulk creates a partially dehydrated surface, which should lead to distinct mechanical properties for both regions. Figure 4.2 illustrates the liquid cell, which was used to simulate the action of these two interfaces.[2]

In the liquid cell, a contact lens is supported on a contoured polypropylene mold. Surrounding the mold is a liquid reservoir, filled with saline solution, which maintains hydration in the bulk. A cover plate, with a 4-mm aperture, was machined to have a smaller radius of curvature than the polypropylene mold on which the contact lens sits. The difference in curvature holds the contact lens in place without distorting the material. The cover plate also acts as a walking stage for the AFM piezoelectric legs. The AFM tip

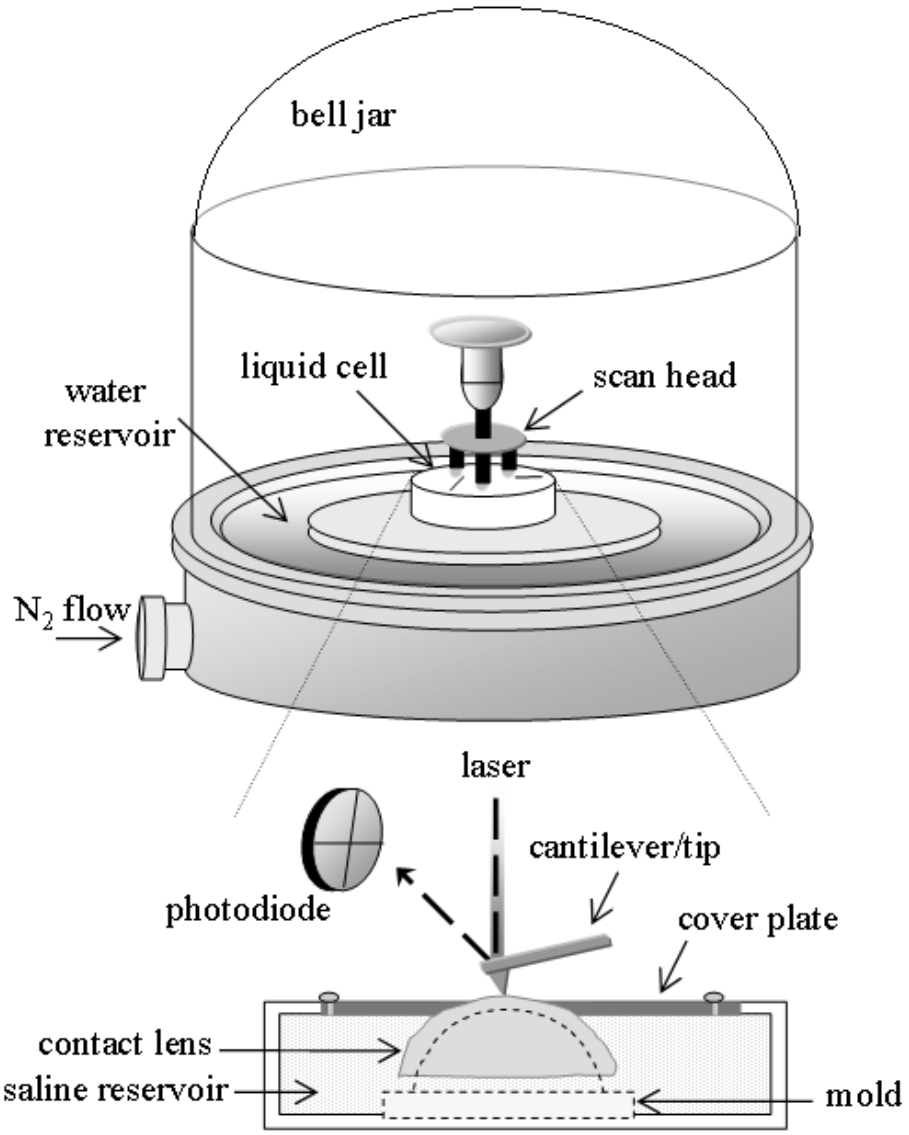

Figure 4.2: AFM experimental setup using a liquid cell. A bell-jar encloses the scan head and Teflon liquid cell. Humidity is controlled by balancing evaporation of water by flow of nitrogen. The liquid cell cross-section (in detail) shows a contact lens supported on a polypropylene mold; the lens is bulk-hydrated from the surrounding saline solution. The AFM tip accesses the anterior surface of the contact lens through a 4-mm aperture in the steel cover plate.

accesses the humidified air/lens interface through the aperture. The force applied by the tip as a function of penetration into the anterior surface of the contact lens is collected.

The lenses were allowed to equilibrate at ambient humidity for 30 minutes prior to making any AFM measurements. This time interval was found to be sufficient, as the mechanical response of the hydrogel surface stabilized after a 15-minute exposure to a set humidity. For comparative purposes, experiments were also performed on bulk-dehydrated hydrogels – in which case there is no saline in the reservoir. This configuration prevents bulk water from replenishing that lost at the lens/air interface. For these experiments, the contact lens was placed on the polypropylene mold and allowed to dry overnight under ambient conditions prior to measurement. The ambient temperature (24±1°C) was monitored within the chamber and remained nearly constant.

4.2.3 Analysis of AFM load-displacement curves

The viscoelastic properties, stress-relaxation times, and the values for stiffness and work of adhesion of the hydrogel surfaces were calculated from load–displacement curves, collected under various probing rates and humidities. The AFM tip is attached to piezoelectric legs that expand and contract in response to an applied voltage. As the piezoelectric legs contract, the tip lowers into the surface at a certain rate, depending on the magnitude of the applied voltage. Thus, the probing rate is the speed with which the AFM tip approaches and strikes the surface. The x-axis in Figures 4.6 and 4.7 refer to this rate. The probing rates used in this study vary from 0.06 to 20 μm/s. Measurements were performed using silicon nitride tips (ND-MDT) with a cantilever force constant of 0.1 N/m. All mechanical properties were analyzed at a load of 2.5 nN.

The load on the hydrogel is obtained by recording the normal deflection signal of the cantilever during a tip approach (loading) and retract (unloading) cycle. A schematic of this cycle is shown in Figure 4.3. As the tip pushes into a sample, cantilever bending reflects the surface stiffness and is quantified by the slope of the AFM approach and retract curves.[22,23] Approach curves for viscoelastic materials are not linear, thus the slope was measured as the tangent to the curve at 2.5 nN. The detector signal (in volts) was calibrated by adjusting the slope of the curve measured against a hydrophilic glass reference to the nominal spring constant of the cantilever.[24] Surface mechanical measurements were repeated with the same cantilever on each of two different poly(HEMA) and poly(HEMA+MA) hydrogel contact lenses, with the error determined from the standard deviation.

Hydrogels exhibit strongly time-dependent viscoelastic behavior under mechanical deformation.[25] In this study, the amount of hydrogel deformation was found to vary with the probing rate and surface water content (via the relative humidity). The total surface deformation performed by the tip is found by subtracting the distance the cantilever has elastically bent (Hooke's law, $\Delta F/k_{\text{lever}}$) from the total travel of the piezoelectric (Δz). This distance represents the total sample deformation – the sum of the elastic and viscous deformations (δ) experienced by the hydrogel. Eq. 4-1 explicitly indicates the time-dependence of the viscous deformation.

$$\Delta z - \Delta F/k_{\text{lever}} = \delta_{\text{elastic}} + \delta(t)_{\text{viscous}} \quad (4\text{-}1)$$

The viscous deformation (δ_{viscous}) for each probing rate can be estimated by subtracting the rate-independent elastic deformation (δ_{elastic}) from the total deformation of the

$$\frac{\partial F}{\partial z} = \text{Stiffness}$$

$$\frac{\partial F / \partial z}{A_{\text{tip}}(z)} = \text{Elastic Modulus}$$

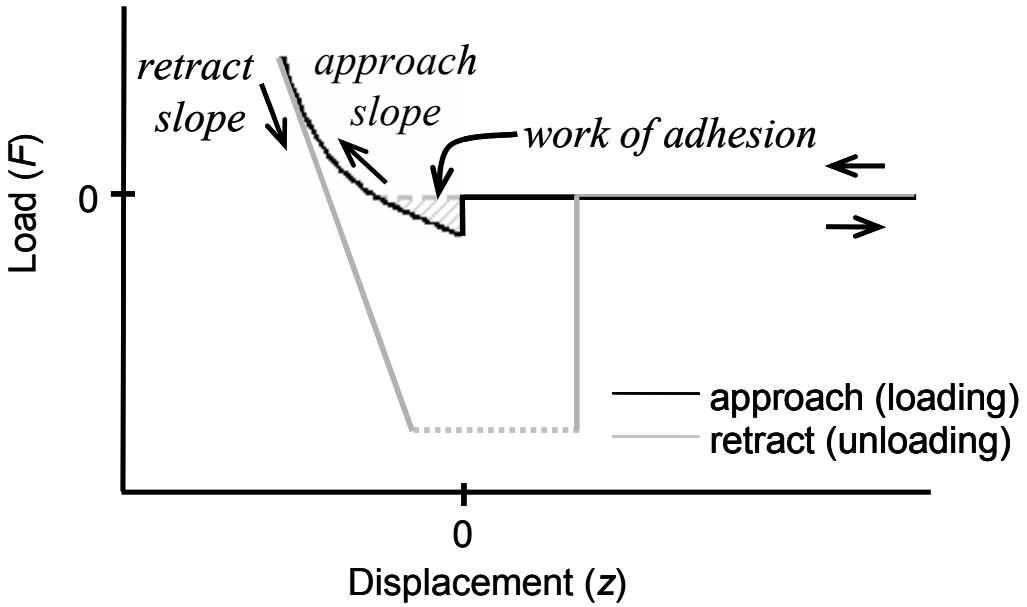

Figure 4.3: Schematic of an AFM load vs. displacement measurement. The arrows indicate the direction of an approach and retract cycle. The area constituting the work of adhesion is highlighted in the snap-in region. The force has been truncated below the dashed line.

polymer. $\delta_{elastic}$ is derived from the *retract* portion of the AFM curve. Here, as the tip begins to pull out from the surface, viscous deformation can be approximately neglected.

The slope of the retract curve, in Newtons per meter, provides the material stiffness and is a convolution of the cantilever and hydrogel mechanical response. Dividing this slope into a given load gives the elastic deformation of the hydrogel-cantilever system at that particular load. Subtracting this elastic deformation from the total *z*-piezo travel (Δz) gives a rough value for the remaining viscous deformation. This approximation is worsened by the extent of adhesion between the tip and surface, which will vary with surface water content.[26]

While stiffness gives a direct measurement of the mechanical response of the material under the AFM tip, the area of contact between the tip and surface is often used to normalize this value. This gives the elastic modulus. The calculation for converting the stiffness into an elastic modulus, in the contact model, involves the tip radius and force constant, with the detailed procedure given elsewhere.[27] The Hertz model has been used in this study to describe the contact area for a half-sphere indenting a plane. The reported elastic modulus values overestimate the true values, since this type of contact model neglects adhesive effects and typically underestimates the true contact area. They are reported only for comparative, order-of-magnitude purposes.

An absolute value for the work of adhesion is determined from the area contained within the snap-in portion of the approach curve, highlighted in Figure 4.3. During snap-in, a combination of van der Waals or electrostatic forces attract the tip. The response of the tip after jumping into contact depends on the material properties of the near-surface region (i.e., the tip will sink further into a softer sample).

4.3 Results and Discussion

4.3.1 Characterization of viscoelasticity in AFM load vs. displacement measurements

The presence of water in the hydrophilic polymer network complicates the physical properties of a hydrogel. It responds as a solid to fast rates of deformation or as a liquid to slow deformation rates – relative to the system's intrinsic relaxation time. That is, the hydrogel responds primarily elastically when mechanical perturbations are swift and viscoelastically when they are slow. At high speeds, the cooperative motion of the cross-linked polymer chains (and the water that surrounds them) cannot relieve the stress as quickly as it is applied.

The AFM load (F) vs. displacement (z) plots, shown in Figure 4.4, highlight the rate-dependent response of the hydrogel surface. The probing rates decrease from left to right. In all three plots, the piezoelectric legs to which the AFM tip is attached travel roughly 150 nm after contacting the surface at $z = 0$ nm. This distance represents the sum of cantilever bending and sample deformation. In Figure 4.4(a), the tip approaches the surface at a velocity higher than the viscous relaxation time of the hydrogel. As a result, the deformation is mostly elastic. The cantilever mostly bends and the tip deforms the surface by only a few nanometers. The approach curve in Figure 4.4(a), from the point of snapping into contact ($z = 0$ nm), is linear (i.e., $\partial F / \partial z$ remains constant). Additionally, the retract curve fully retraces the approach curve in the AFM plot. The absence of hysteresis between the approach and retract curves in Figure 4.4(a) implies that, at a certain probing rate, primarily elastic surface mechanics are observed.

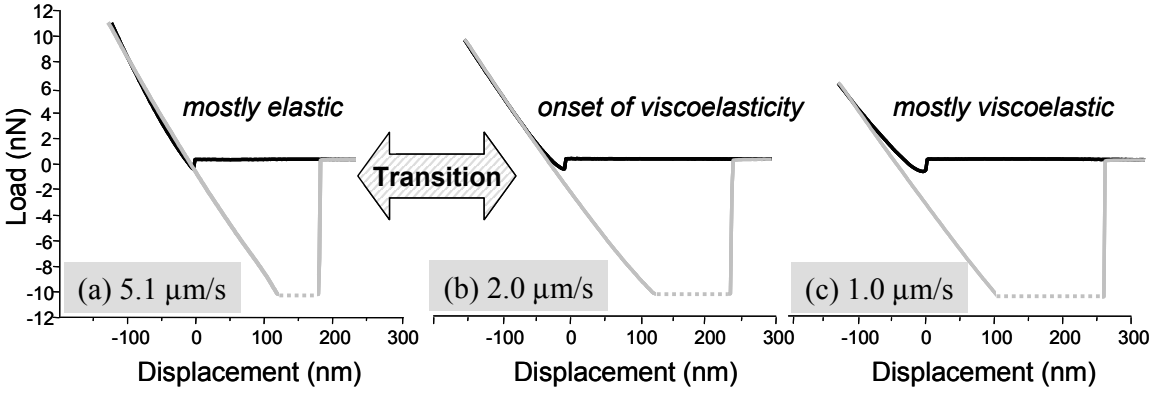

Figure 4.4: AFM load vs. displacement plots taken at (a) 5.1, (b) 2.0, and (c) 1.0 μm/s for bulk-hydrated poly(HEMA+MA) (k = 100 mN/m, T = 25ºC, RH = 72%). The force is truncated below -11 nN. Hysteresis between the approach and retract curves indicates viscoelastic mechanics.

Probing the surface at slower rates causes the measured mechanics to gradually shift from being primarily elastic to viscoelastic. In Figure 4.4(b), the hysteresis between approach and retract curves near the contact region indicates viscoelastic deformation. In Figure 4.4(c) – the slowest rate – the hysteresis is more pronounced; in addition, there is a large degree of curvature in the approach curve. When the experiment is repeated over the same area, identical data is acquired, indicating that the hydrogel surface is recovered for each indentation cycle.

4.3.2 Surface viscoelastic behavior

The data points in Figure 4.5 mark the probing rates which transition between the elastic and viscoelastic measured response for a given humidity. Faster probing causes the hydrogel to respond elastically, while slower probing causes it to respond viscoelastically. Thus, the curves drawn through the data points separate the elastic and viscoelastic regimes. The onset of viscoelasticity is mapped out under a 2.5-nN load for both the bulk-hydrated and bulk-dehydrated hydrogels. The data indicate that the transition between elastic and viscoelastic mechanics depends not only on the probing rate, but also on the humidity and bulk water content of the system.

The hydrogel surface is dehydrated, relative to the bulk, below ~35% RH for poly(HEMA) and 50% RH for poly(HEMA+MA). Even with the slowest probing rate available in the AFM experimental setup, no viscoelastic behavior can be measured in bulk-hydrated hydrogels at these low humidites. Above 60% RH, there is sufficient water present in the near-surface region of both hydrogels to mediate viscoelastic mechanics, as shown in the previous chapter.[5] Further, the bulk-*dehydrated* lens in Figure 4.5(c) shows

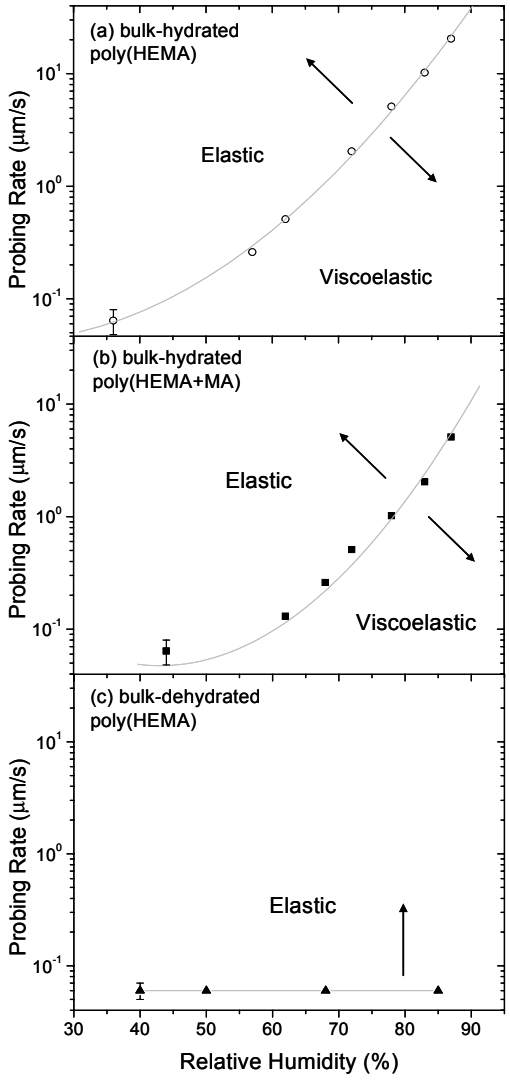

Figure 4.5: Humidity and probing rate dependence on the transition from viscoelastic to elastic behavior for bulk-dehydrated (a) poly(HEMA) and (b) poly(HEMA+MA), contrasted with (c) bulk-dehydrated poly(HEMA), which shows no such dependence. The curves divide the elastic from the viscoelastic regimes under a load of 2.5 nN. Each point marks the rate above which the approach slope remains constant and primarily elastic surface mechanics are observed.

no signs of viscoelastic behavior – even at high relative humidity. Atmospheric moisture, alone, condensing through the surface of the bulk-dehydrated hydrogel is not enough to plasticize the surface. Instead, the condensed water is likely sequestered into the bulk. Given adequate time in a well-humidified environment (> 90% RH), an initially bulk-dehydrated hydrogel will absorb enough water to show surface viscoelastically.[28]

The onset of surface viscoelastic behavior in poly(HEMA+MA) is delayed by 15% RH, relative to poly(HEMA), despite the fact that poly(HEMA+MA) possesses a higher bulk water content. The difference in viscoelastic behavior for poly(HEMA+MA) suggests lower relative water content at the surface for any given humidity above ~40% RH. This observation can also be made by comparing the relative areas separated by the curves. Comparing Figure 4.5(a) to (b), the viscoelastic regime for poly(HEMA) encompasses more area, relative to the same regime in poly(HEMA+MA).

4.3.3 Gauging relative water content with AFM approach curve slopes

In Figure 4.6, the approach slopes are plotted versus probing rate for several values of humidity. These slopes are a measure of surface stiffness. There is a gradual decrease in the value of the *approach* slope as the humidity is increased – the surface softens. The approach slope is humidity-dependent because it is a convolution of both elastic and viscous effects, the latter of which dominates with increased water content. Figure 4.7 deconvolutes the viscous contribution to the surface mechanics by examining the slope of the retract curve as a function of probing rate. Deconvolution is valid because the hydrogel surface recovers elastically as tip pressure is relieved during retraction. The

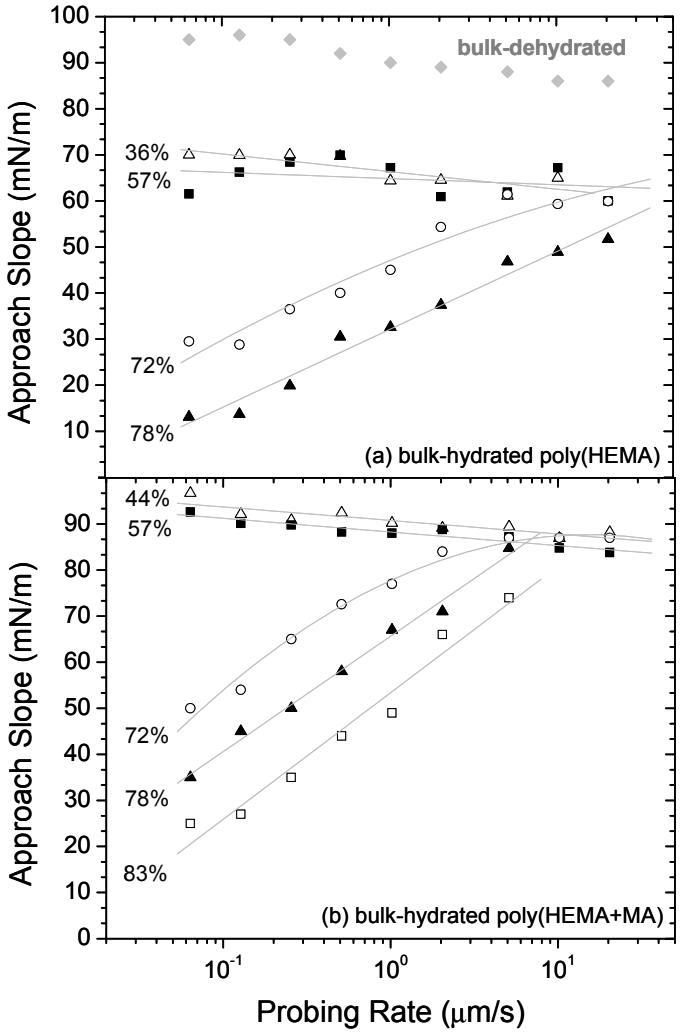

Figure 4.6: Graphs of approach slopes versus AFM probing rates bulk-hydrated (a) poly(HEMA) and (b) poly(HEMA+MA). The relative humidity for each curve is indicated on the left. The slopes are measured under a load of 2.5 nN (k = 100 mN/m). The abrupt change in curve shape marks a change in mechanical response. Data for the bulk-dehydrated hydrogel (overlaid in gray) represent average slope values obtained at each humidity for the given probing rate.

retract slopes do not vary significantly as a function of rate on the same slope scale (0-100 mN/m). The average slope value at any rate during tip retraction remains in the middle of cantilever sensitivity – around 50 mN/m.

While similar trends in mechanical behavior are observed for both hydrogels as the humidity or probing rate is varied, the approach slopes for poly(HEMA+MA) are shifted higher, relative to those for poly(HEMA). That is, poly(HEMA+MA) is stiffer for any given humidity and rate. The slopes for bulk-hydrated poly(HEMA+MA) approach 90 mN/m as the probing rate is increased or the humidity lowered. The slope values for the poly(HEMA) hydrogel also saturate under these conditions, but they are much lower (70 mN/m). This also suggests lower water content in the near-surface region for the hydrogel with higher bulk water content. The elastic modulus normalizes these slope values to the contact area. The elastic moduli for poly(HEMA) range from 0.8 MPa to 1.5 MPa, at 87% and 36% RH, respectively. The surface hardens as interfacial water is lost to the atmosphere. For poly(HEMA+MA), the elastic moduli are much higher: 3 MPa at 87% RH and 8 MPa at 44% RH. These numbers are greater than the bulk elastic moduli of the hydrogels, which measure 0.5−0.7 MPa.

The rate-dependence of the slopes of the approach curves can be used to determine the humidity which transitions between elastic and viscoelastic mechanics. First, in Figure 4.6(a) and (b), the approach slopes for both hydrogels at 57% RH and below do not vary much with rate. As before, the lack of rate dependence in the slopes is due to elastic behavior at low humidity. But, as the humidity is ramped upward, the slopes become increasingly rate-dependent. A transformation in mechanical behavior is

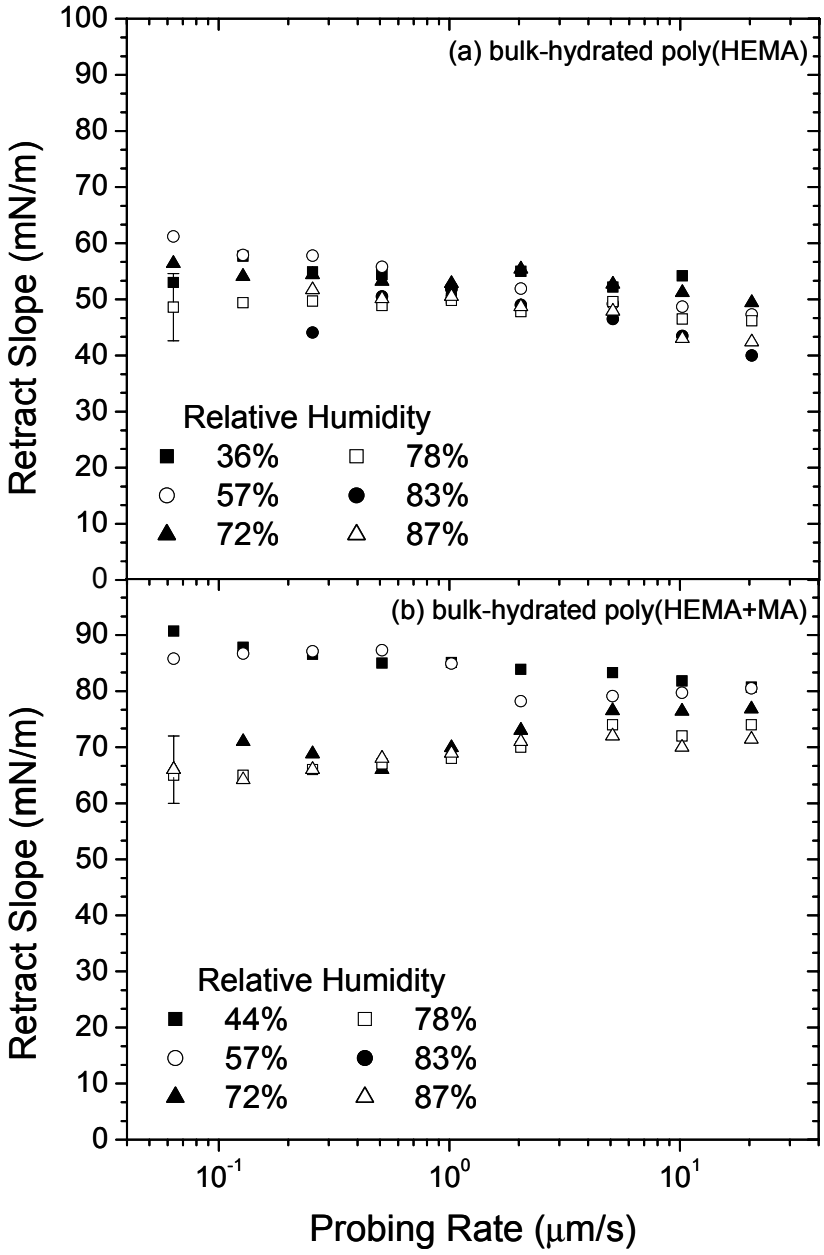

Figure 4.7: Graphs showing the slopes measured during initial tip retraction from (a) poly(HEMA) and (b) poly(HEMA+MA) surfaces versus AFM probing rate. Here, elastic recovery mechanisms dominate. The slopes show almost no dependence on the probing rate because the rate-dependent viscous component is minimized during the retract cycle.

observed between 57% and 72% for both poly(HEMA) and poly(HEMA+MA), as seen in the abrupt change in curve shape. In Figure 4.5, the same transition is also estimated to occur at ~ 60% RH for most probing rates. Above this critical humidity, the surface water concentration keeps the polymer chains well-solvated and allows them to accommodate more stress. In addition, the presence of water should depress the hydrogel's effective T_g.

The approach slopes sweep through a greater range for poly(HEMA+MA). In the experiment conducted at 87% RH, the slope increases from 20 to 70 mN/m. Or if the rate is held constant at 0.06 μm/s, the slope changes from 20 to 95 mN/m as the relative humidity is decreased – a nearly five-fold increase. This variability is not seen in poly(HEMA) and implies more drastic losses in water content. Differences in the mechanical behavior between viscoelastic materials are more sharply resolved under conditions which enhance their viscous behavior (i.e., high humidity or slow probing rate). The trend is reversible, moving from either high to low or low to high humidity.

4.3.4 Relaxation properties and resolution of stress components

An approximate value of the hydrogel relaxation time at the viscoelastic transition can be determined by dividing the surface deformation by the probing rate. The relaxation times shown in Figure 4.8, an analogue of the data presented in Figure 4.5, measure how long the tip has spent performing surface-deforming work at each humidity. The deformation is primarily elastic, since the rate employed in these calculations is that which just follows the viscoelastic transition. Consequently, a load of 2.5 nN must be applied on a timescale longer than those shown in Figure 4.8 for the hydrogel to behave

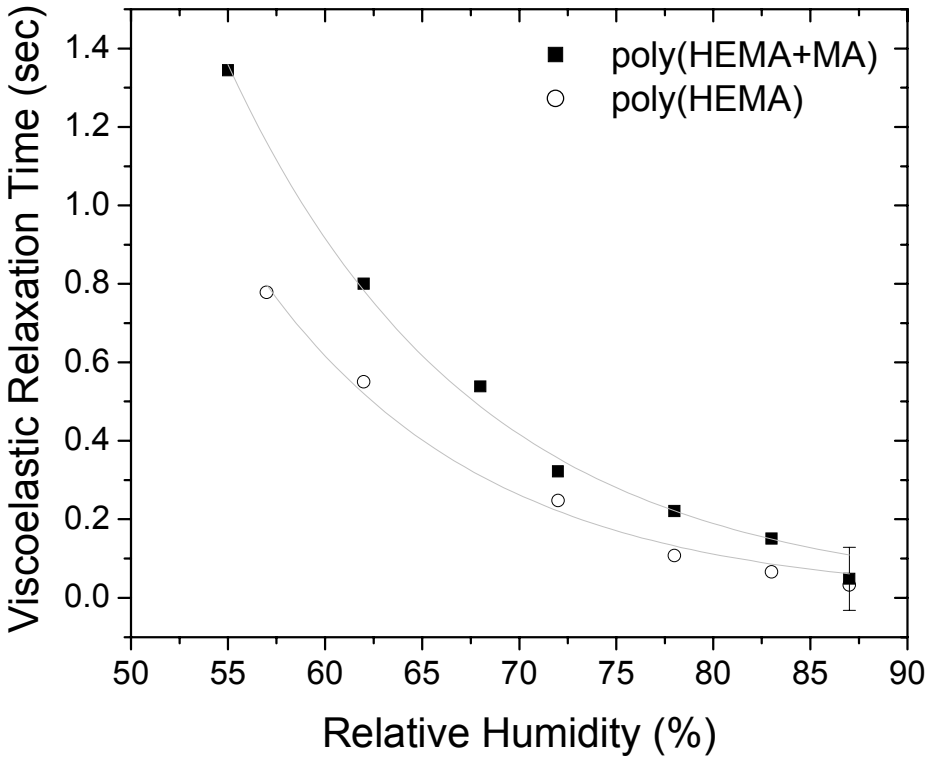

Figure 4.8: Viscoelastic relaxation times at varying relative humidities for bulk-hydrated poly(HEMA) and poly(HEMA+MA) hydrogels. The data measures the deformation time required to transition to primarily viscoelastic behavior under a load of 2.5 nN.

viscoelastically. Relaxation times are related to the cooperative motion of the polymer-water system under stress. At high humidity, the response is quick (~0.2 sec) and the stress is dissipated by polymer chains adopting new conformations. These motions are assisted by the presence of water solvent.

The lag in relaxation times between the two hydrogels becomes more pronounced under low relative humidities; the near-surface region of poly(HEMA+MA) requires an additional 0.2 to 0.3 seconds to absorb a 2.5-nN load. Unlike the case of high humidity, where the tip sinks into the surface, stress-relaxation is more difficult for hydrogels in a low-humidity environment. Under 60% RH, with decreased water content, the surface contracts and the polymer chains entangle. The tip cannot probe as deeply, since polymer chain motion is frustrated. Here, times in excess of a second are required to dissipate the stress. Another method to characterize the viscoelastic work loss vs. RH would be to measure the difference in area between loading and unloading curves due to hysteresis.

Viscoelastic deformation can be separated into its elastic and viscous components to a first approximation using the method outlined in the experimental section. This data is shown in Figure 4.9. Under a 2.5-nN load, the total deformation (the sum of the elastic and viscous components) is higher for poly(HEMA). The poly(HEMA+MA) surface is less compliant for the same load. Prior to the transition at 70% RH, the elastic components of deformation for both hydrogels increase monotonically. No viscous deformation can be extracted below ~60% RH for poly(HEMA) and ~70% RH for poly(HEMA+MA). At high humidities, viscous deformation accounts for most of the stress relaxation with the excess water in poly(HEMA) mitigating more of the surface stress relative to poly(HEMA+MA) for any given humidity.

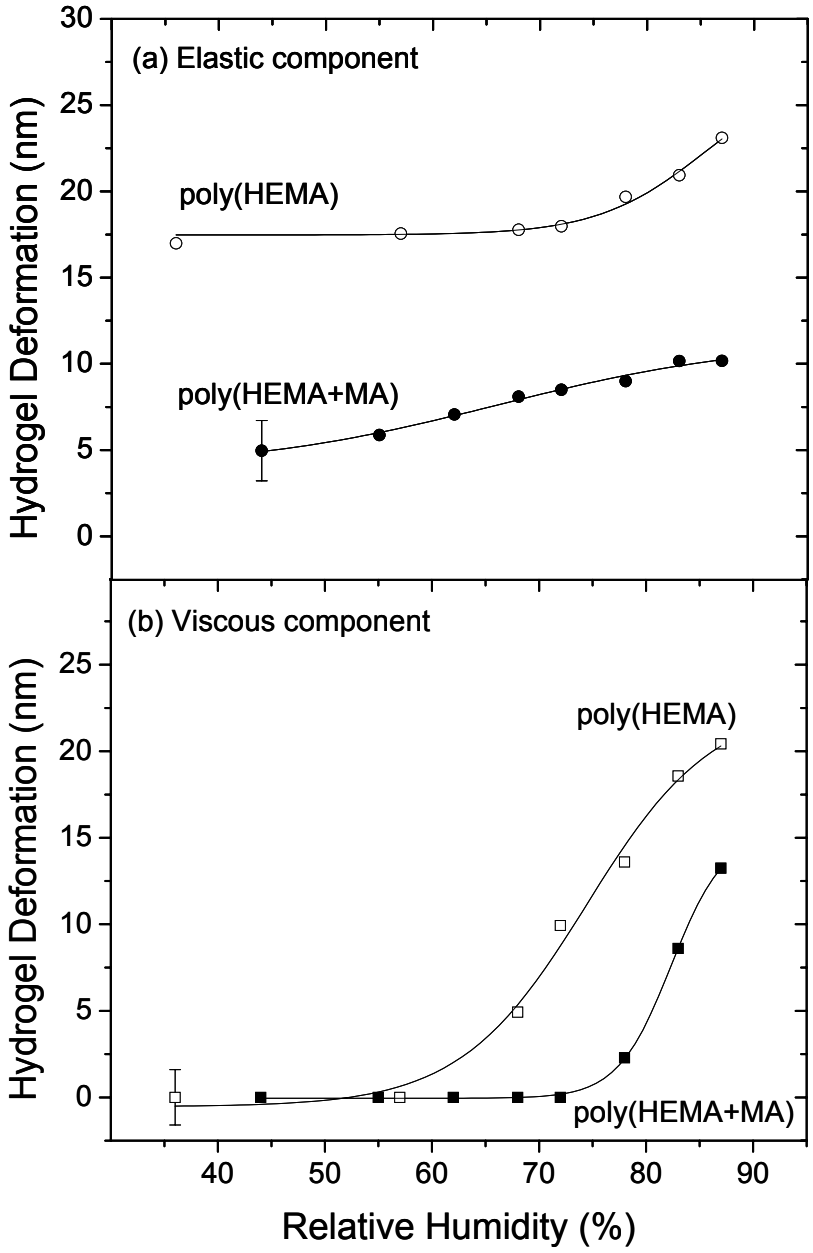

Figure 4.9: Graphs of (a) elastic and (b) viscous deformation components vs. relative humidity under a 2.5-nN load (k = 0.1 N/m, probing rate = 1.02 μm/s).

4.3.5 Surface adhesion effects

The location of water in a hydrogel is of concern when addressing mechanical properties. The AFM data demonstrates that water does not exist as a thin layer atop the polymer surface. The forces required to snap out of the hydrogel surface are significantly less than 100 nN and argue against capillary adhesion. In addition, successive or discontinuous snap-out regions in the retract portion of the load-displacement curve would be observed in the case of two phase-separated regions. The increases in snap-out distance as the humidity is increased reflect changes in the mechanical compliance of the polymer-water *system*, not the presence of a water film at the surface. Indeed, no changes in the snap-out distance are observed for a hydrophilic glass reference as the humidity is changed. The relative surface tensions[16] of poly(HEMA) (dry: 37 dyn/cm, bulk-hydrated: 69.0 dyn/cm) and water (72.8 dyn/cm) support this conclusion, as do previously published SFG vibrational spectra. SFG spectra indicate the presence of only polymer at the hydrogel/air interface.[29] Details of this second-order, nonlinear process can be found in Chapter 1 or in recent review papers.[30,31]

The work of adhesion, calculated from the area constituting the snap-in portion of the AFM approach curve, is presented in Figure 4.10. Although the radius of curvature of the AFM tip is known (~50 nm), the work of adhesion has not been normalized by the maximum area of contact between the sample and AFM tip. This is because the area of contact is likely to be significantly less than the maximum possible (2500π nm^2) for data taken at the fast probing rates, due to the stress-relaxation phenomena discussed previously. The hydrogel surface is not given adequate time to absorb and relieve the

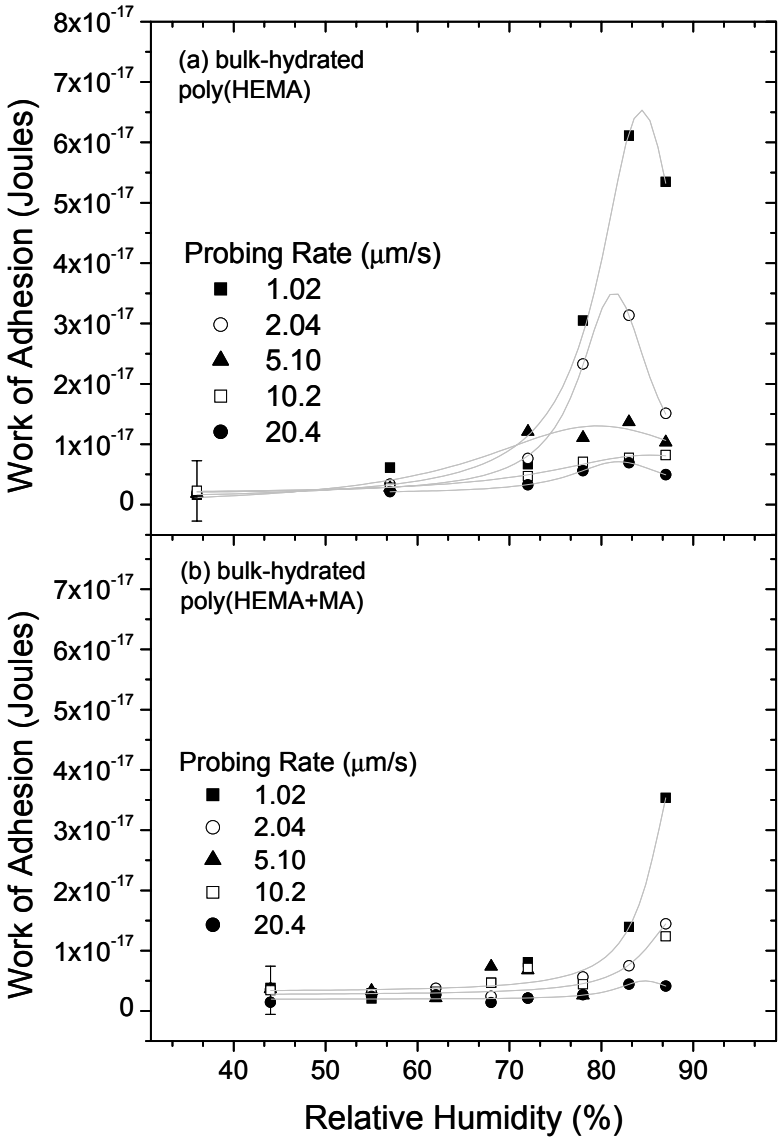

Figure 4.10: Absolute values of the work of adhesion as a function of humidity for bulk-hydrated (a) poly(HEMA) and (b) poly(HEMA+MA) under a load of 2.5 nN. The work is calculated from the area bounded by the snap-in portion of the AFM approach curve.

stress at these fast rates. Consequently, the work of adhesion is presented as an absolute value in Joules.

The surface of poly(HEMA) is most compliant between 80−85% RH for each rate. This is where the product of tip sinking and adhesion forces is maximized (~6.5 x 10^{-17} J). Slower probing rates tend to higher values for the work of adhesion. This is expected, as the surface is given adequate time to reconstruct around the AFM tip. The work of adhesion, however, does not approach an asymptotic value as the humidity is increased. Instead, there is a drop-off at 87% RH. Because the tip penetrates so quickly, this may be a non-equilibrium process, in which case the work is underestimated.

The work of adhesion values for poly(HEMA+MA) follow a similar trend, although they are typically lower than the adhesion values of poly(HEMA). A maximum of ~3.5 x 10^{-17} J is expended for the slowest rate. All of the work values below 80% RH are quite similar for any given rate, however, and suggest a less compliant surface. Smaller snap-out distances for poly(HEMA), which give a direct indication of the adhesive forces acting between tip and sample, also bear this out. The fastest probing rate (20.4 μm/s) appears to have gone through its maximum (0.5 x 10^{-17} J), but the data for any of the remaining rates have not. Thus, relative humidities exceeding 87% are required to achieve a maximum work value for the slower rates. The required increase in humidity for poly(HEMA+MA) also suggests that its surface is water-deprived and less compliant relative to poly(HEMA).

4.3.6 Correlation of surface mechanical to chemical properties

The mechanical data confirms earlier investigations that indicate a surface water deficit exists for poly(HEMA) hydrogels, relative to the water content in the bulk. In addition, as the bulk water content is increased by making the hydrogel material more hydrophilic, the interfacial water content actually declines. The AFM data agrees with clinical studies, which show contact lenses with high bulk water content dehydrate more quickly and to a greater extent than those with lower bulk water content.[18] In order to rationalize this behavior, the control of bulk and interfacial water content by the hydrogel chemistry must be considered. That is, water transport in a hydrogel must be described in terms of the electrostatic interactions between water molecules and the polymer network.

McConville and Pope have made ^{1}H NMR measurements of the spin-spin (T_2) and spin-lattice (T_1) relaxation times to investigate water binding and mobility in HEMA-based hydrogels of varying equilibrium bulk water content.[32] Two correlation times for water protons in their model is consistent with the presence of water molecules in two rapidly-exchanging environments: hydrogen-bonded to polymer and freely diffusing. As the bulk water content of the hydrogel is increased, water molecules are found to actually bind to polymer less strongly. The increased mobility of water molecules in hydrogels with high bulk water content may lead to an increase in the evaporative flux. In the hydrogels they studied, their model indicates that the average mobility of water molecules depends more on the equilibrium bulk water content of the hydrogel than on the specific polymer formulation used to achieve that water content. The calculated water diffusion coefficients in hydrogels having the same equilibrium water content, but different polymer compositions, were only slightly affected by differences in hydrogel

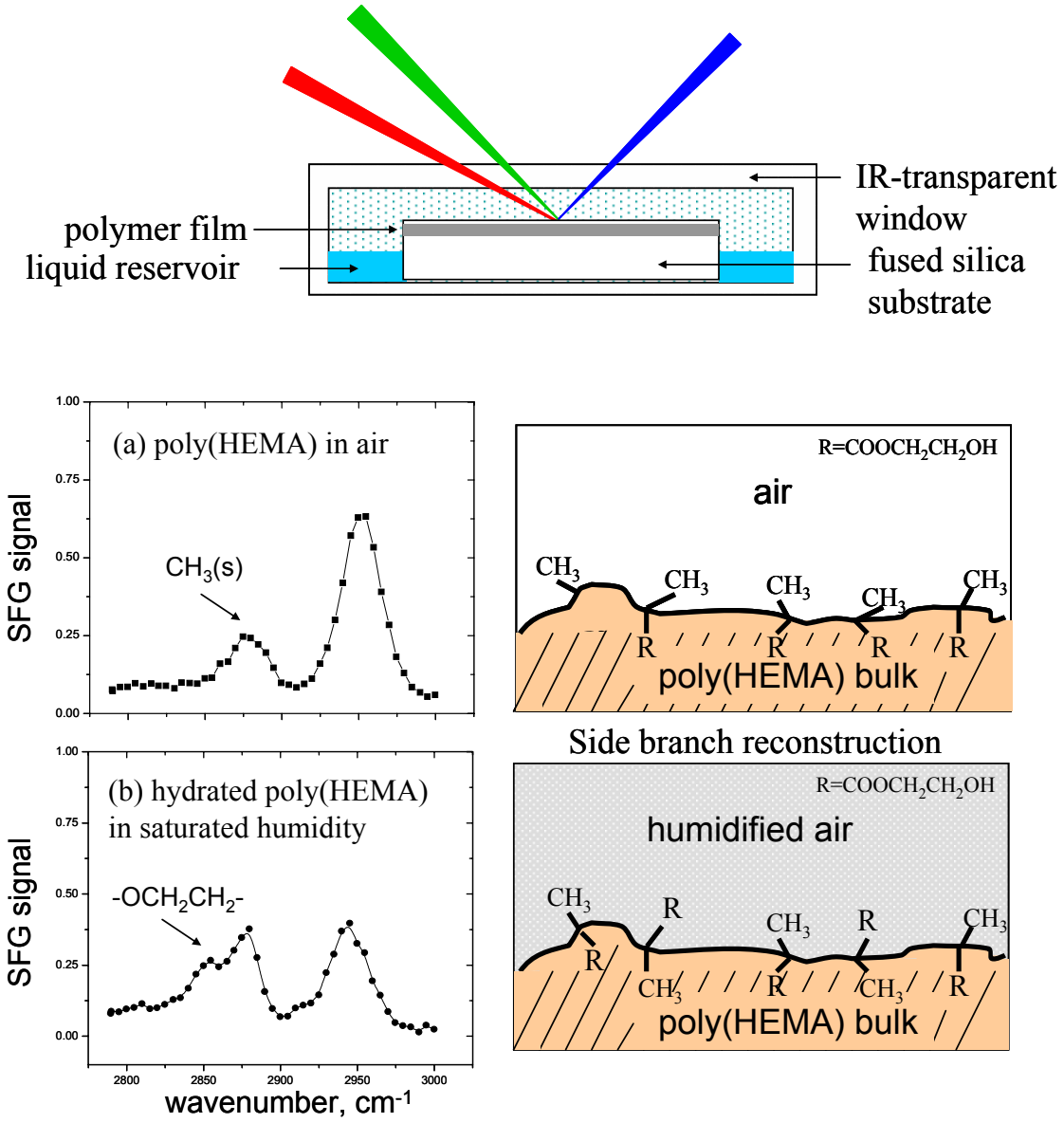

Figure 4.11: SFG spectra of poly(HEMA) exposed to (a) air and to (b) saturated humidity. To lower the overall surface energy, the polymer chain reorients itself to expose its hydrophilic hydroxyethyl groups into the vapor phase. The vapor cell used to collect SFG spectra at the polymer/air and polymer/vapor interfaces is shown above.

chemistry. The authors, however, do not rule out the possibility that hydrogel materials with anomalous water transport properties can be used to improve water retention.

Although manufacturers can alter the copolymer formulation of their contact lenses to improve water binding in the bulk, the surface composition and chemistry of the hydrogel dictate the state of interfacial hydration. AFM and SFG studies have shown that a surface-enrichment in the hydrophilic component of a copolymer system or in the fraction of hydrophilic pendant groups occurs at a wetted polymer interface.[33,34] Figure 4.11, for instance, shows that as the humidity is increased, poly(HEMA) chains at the surface reorient to allow their hydrophilic hydroxyethyl groups to replace pendant methyl groups.[29] Long-range migration of hydrophilic polymer segments to a water interface, however, is not likely in cross-linked hydrogel networks. As a result, monomers may be locked in place, unable to minimize the surface energy of the hydrogel. SFG has not been able to detect a peak corresponding to the carboxyl group of the methacrylic acid component of poly(HEMA+MA) in high humidity. This suggests that either carboxyl groups are not present at the hydrogel surface or that they are not sufficiently ordered to generate SFG. A greater understanding of chain mobility and morphology in cross-linked hydrogels is needed to determine how the chemistry of copolymers controls interfacial water content.

4.4 Conclusion

As contact lenses dehydrate, they must draw water from the eye. As a result, the ocular comfort of contact lenses is tied into their surface mechanical and chemical properties. AFM has been shown to be a powerful tool in appraising the role of humidity

and, consequently, interfacial water content in controlling surface viscoelastic and compliance effects. Measuring the changes in the mechanical properties of hydrogels as a function of humidity and probing rate is a useful way to track interfacial water content. In Appendix B, the affect of an adsorbed protein layer on a hydrogel surface is addressed. Lysozyme is used to fully mimic an ocular environment and determine whether surface water content is affected.

The lag in the onset of viscoelastic behavior, as well as differences in surface stiffness and work of adhesion between poly(HEMA) and poly(HEMA+MA) point to lower interfacial water content for poly(HEMA+MA). Prior clinical and experimental observations also show interfacial water content is compromised in high bulk water content lenses. Ongoing work in finding novel methods to retain surface wettability and biocompatibility for high water content lenses (e.g., preferential segregation or grafting of the hydrophilic component to the surface) is needed.[35]

4.5 Appendix B: Analysis of protein adsorption at the hydrogel surface: surface roughness and water content

The surfaces of poly(HEMA) hydrogel contact lenses exposed to lysozyme (LYZ) solutions of various concentration over a 24-hour period were investigated by AFM. Friction images are shown in Figure 4.12. The root-mean-square (rms) roughness values for the corresponding topographic images were also calculated in order to gauge the degree and nature of protein adsorption. The rms roughness is defined as the standard deviation of the height and provides a relative measure of surface smoothness.

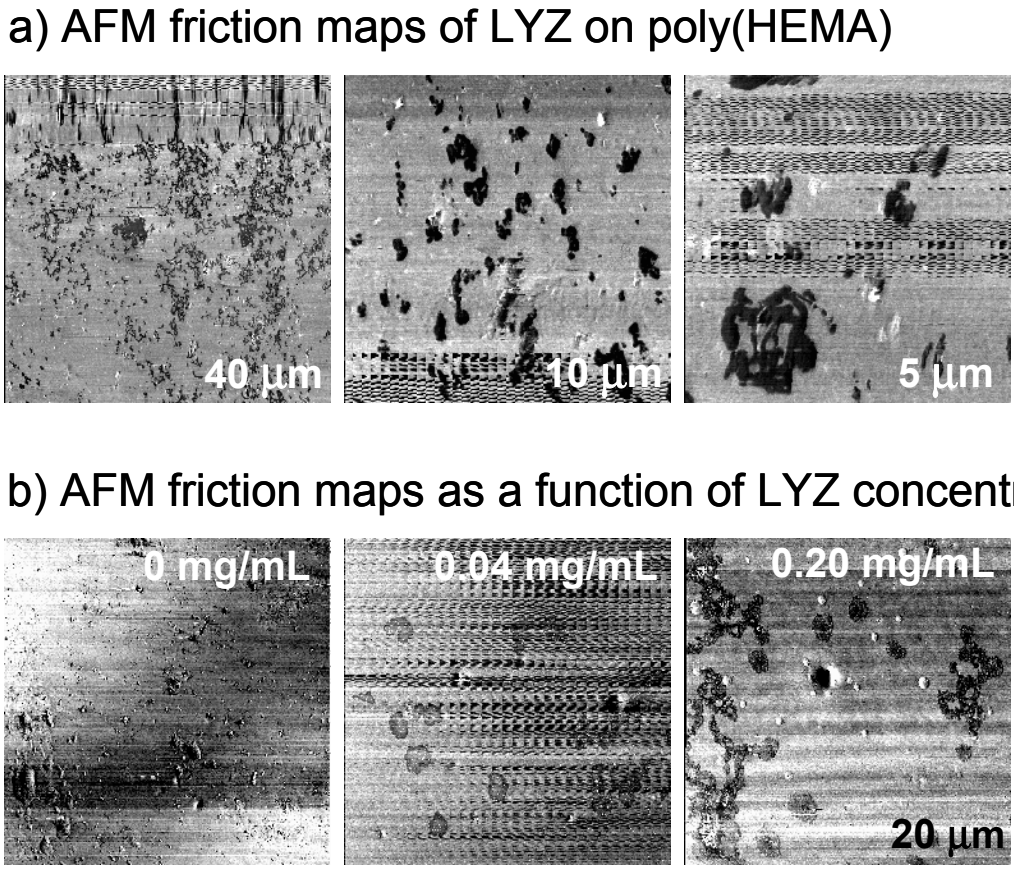

Figure 4.12: AFM friction images of lysozyme (LYZ) on poly(HEMA) at (a) the indicated scan size and (b) exposed to protein solutions at the indicated protein concentration.

Figure 4.13 shows that the rms roughness reaches a maximum and then decreases. Initially, a bare poly(HEMA) with a ~20-Å rms surface roughness exists. When LYZ is deposited, the initially smooth surface is dotted by protein and there is an associated increase in surface roughness. However, when the hydrogel is exposed to LYZ solution of higher protein concentration and more protein is deposited, the surface roughness decreases to a value below the original surface roughness of bare poly(HEMA). The increase in protein deposition is visually observed in the AFM images shown in Figure 4.12(a). LYZ is a somewhat hard protein, yet will still denature and spread out when adsorbed onto a surface. The decrease in surface roughness is observed as we transition from imaging a surface dotted with protein to one that is layered by it.

To ensure that protein had deposited on the surface, fluorescence microscopy measurements of LYZ labeled with a Texas Red fluorophore were performed. Prior to analyzing this surface, poly(HEMA) hydrogels were removed from the protein solution and rinsed to remove any unadsorbed LYZ. The fluorescence intensity is then proportional to the concentration of protein at the hydrogel surface. Figure 4.13(b) shows that there is a steep rise in the fluorescence intensity as more protein as deposited; the curve then approaches a limiting value indicative of complete surface coverage.

While it is known that contact lenses with large amounts of adsorbed protein can leave the eye vulnerable to infection, it is also advantageous to use a layer of adsorbed protein from a surface roughness and tribology point of view. Very recently, contact lenses with a monolayer of covalently-tethered protein have been developed. Because protein is already immobilized at the surface, further protein adsorption is retarded. These

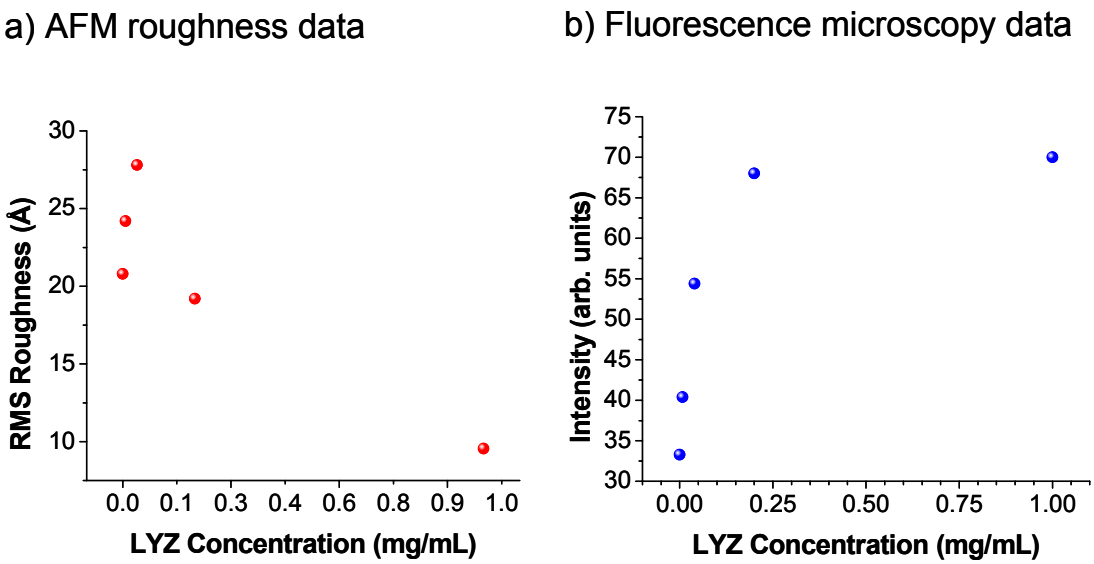

Figure 4.13: Plots of (a) AFM rms roughness data and (b) fluorescence intensity at the poly(HEMA) surface as a function of the lysozyme (LYZ) concentration of solutions to which the hydrogels are exposed.

lenses find use in extended wear applications. In Chapter 5, AFM friction data is complemented by molecular-level SFG analysis of the protein/polymer interface.

The nominal concentration of LYZ in tear fluid in 4 mg/mL,[36] yet surface water transport appears to be affected at even lower concentrations. Preliminary AFM force-distance measurements, using the method outlined in Chapter 3, indicate that adsorbed protein leads to a decrease in surface water content. The amount of protein deposition will increase for high bulk water content ionic contact lenses, which carry a negative charge at ocular pH (6.5 – 7.6).[36,37] The transport of LYZ, with an isoelectric point of 11, to the HEMA surface is driven by both hydrophobic and electrostatic forces. Thus, changes in the surface mechanical properties of poly(HEMA+MA) are amplified relative to poly(HEMA) for exposure to a solution at a given lyzozyme concentration.

In fact, due to its small size, much of the LYZ actually penetrates into the hydrogel polymer matrix. Early studies of water permeability in LYZ-adsorbed contact lens materials by Mirejovsky et al. actually show that the equilibrium water content is lowered by about 5%wt.[38] This AFM study indicates that the loss in bulk water may translate up to the surface. Further research by Cheng et al. on the wettability of HEMA materials demonstrates that the tear film over the contact lens is more susceptible to break up upon LYZ adsorption, although they also argue that it is easier to re-wet the surface, relative to a film formed from an isotonic solution.[36]

References

(1) Kim, S. H.; Opdahl A.; Marmo C.; Somorjai, G. A. *Biomaterials* **2002**, *23,* 1657.

(2) Kim, S. H.; Marmo, C.; Somorjai, G. A. *Biomaterials* **2001**, *22*, 3285.

(3) Arciola, C. R.; Maltarello, M. C.; Cenni, E.; Pizzoferrato A. *Biomaterials* **1995**, *16*, *685*.

(4) Wahlgren, M.; Arnebrant, T. *Trend Biotech*. **1991**, *9*, 201.

(5) Opdahl, A.; Kim, S. H.; Koffas, T. S; Marmo, C.; Somorjai. G. A., *J. Biomed. Mat. Res.* **2003**, *67A*, 350.

(6) Bruinsma, G. M.; van der Mei, H. C.; Busscher, H. J. *Biomaterials* **2001**, *22*, 3217.

(7) Bonanno, J. A.; Stickel, T.; Nguyen, T.; Biehl, T.; Carter, D.; Benjamin, W. J.; Soni, P. S. *Invest. Ophth. Vis. Sci.* **2002**, *43*, 371.

(8) Harris M. G.; Hall, K.; Oye, R. *Am. J. Optom. Arch. Am. Acad. Optom*. **1973**, *50*, 546.

(9) Nicolson, P. C.; Vogt, J. *Biomaterials* **2001**, *22*, 3273.

(10) Barbieri, R.; Quaglia, M.; Delfini, M.; Brosio, E. *Polymer* **1998**, *39*, 1059.

(11) McConville, P.; Pope, J. M. *Polymer* **2000**, *41*, 9081.

(12) Jhon, M. S.; Ma, S. M.; Hattori, S.; Gregonis, D. E.; Andrade, J. D. *Hydrogels for Medical and Related Applications*; Andrade, J. D., Ed.; American Chemical Society: Washington, D.C., 1976; pp 60-68.

(13) Wichterle, O.;Lim, D. *Nature* **1960**, *185*, 117.

(14) Ratner, B. D.; Hoffman, A. S. *Hydrogels for Medical and Related Applications*; Andrade, J. D., Ed.; American Chemical Society: Washington, D.C., 1976; pp 1-36.

(15) Refojo, M. F. *Hydrogels for Medical and Related Applications*; Andrade, J. D., Ed.; American Chemical Society: Washington, D.C., 1976; pp 37-51.

(16) *Polymer Handbook*, Brandup, J., Immergut E. H., Grulke, E. A., Eds.; Wiley: New York, 1989.

(17) Pritchard, N.; Fonn, D. *Opthal. Physiol. Opt.* **1995**, *15*, 281.

(18) Kohler, J. A.; Flanagan, G. W. *ICLC* **1985**, *12*, 152.

(19) Lopez-Alemany, A.; Compan, V.; Refojo, M. F. 2002, 63, *J. Biomed. Mat. Res.* **2002**, *63*, 319.

(20) Martin, D. K. *J. Biomed. Mat. Res.* **1995**, *29*, 857.

(21) Gracias, D. H.; Zhang, D.; Lianos, H.; Ibach, W.; Shen, Y. R.; Somorjai, G. A. *Chem. Phy.* **1999**, *245*, 277.

(22) Tsukruk, V. V.; Huang, Z.; Chizhik, S. A.; Gorbunov, V. V. *J. Mater. Sci.* **1998***, 33*, 4905.

(23) Chizhik, S. A.; Huang, Z.; Gorbunov, V. V.; Tsukruk, V. V. *Langmuir* **1998**, *14*, 2606.

(24) The reference was prepared by treating a glass slide with Piranha solution.

(25) Ferry, J. D. *Viscoelastic Properties of Polymers*, 3rd ed.; New York: Wiley, 1980.

(26) Basire, C.; Fretigny, C. *Tribol. Lett.* **2001**, *10*, 189.

(27) Opdahl, A.; Somorjai, G. A. *J. Polym. Sci. Pol. Phys.* **2001**, *39*, 2263.

(28) Gregonis, D. E.; Chen C. M.; Andrade, J. D. *Hydrogels for Medical and Related Applications*; Andrade, J. D., Ed.; American Chemical Society: Washington, D. C., 1976; pp 88-104.

(29) Chen, Q; Zhang, D; Somorjai, G. A.; Bertozzi, C. R. *J. Am. Chem. Soc*. **1999**, *121*, 446.

(30) Chen, Z.; Shen, Y. R.; Somorjai, G. A. *Annu. Rev. Phys. Chem*. **2002**, *53*, 437.

(31) Shen, Y. R. *Pure Appl. Chem*. **2001**, *73*, 1589.

(32) McConville, P; Pope, J. M. *Polymer* **2001**, *42*, 3559.

(33) Chen, C.; Wang, J.; Woodcock, S. E.; Chen, Z. *Langmuir* **2002**, *18*, 1302.

(34) Zhang, D.; Gracias, D. H.; Ward, R.; Gauckler, M.; Tian, Y.; Shen, Y. R.; Somorjai, G. A. *J. Phys. Chem. B* **1998**, *102*, 6225.

(35) Elbert, D. L.; Hubbell, J. A. *Ann. Rev. Mater. Sci.* **1996**, *26*, 365.

(36) Cheng, L; Muller S. J.; Radke, C. J. *Curr. Eye Res.* **2004**, *28*, 93.

(37) Yamada, M.; Kawai, M.; Mochizuki, H.; Hata Y.; Yukihiko M. *Curr. Eye. Res.* **1998**, *17*, 1005.

(38) Mirejovsky, D.; Patel, A. S.; Rodriguez, D. D. *Curr. Eye Res.* **1991**, *10*, 187.

Chapter 5

Surface Analysis of Immobilized Protein on Latex Microspheres

5.1 Introduction

Protein adsorption on to solid interfaces holds much interest in the scientific and medical communities, owing to its relevance in implant biocompatibility, biofouling, and diagnostics.[1-3] In Chapters 3 and 4, the surface mechanics of contact lens hydrogels were discussed in relation to their surface chemical configuration. Our discussion of biopolymers would be incomplete, however, without addressing the nature of protein deposition at the polymer interface. SFG analysis of the polymer/polymer interface was introduced in Chapter 2. The results of that chapter concerning the role of surface energy and water solvent in mediating the interaction between polymer adsorbate and polymer substrate will serve us well in discussing protein deposition, as proteins are assemblies of polypeptides, each of which is a polymer chain composed of amino acid residues.

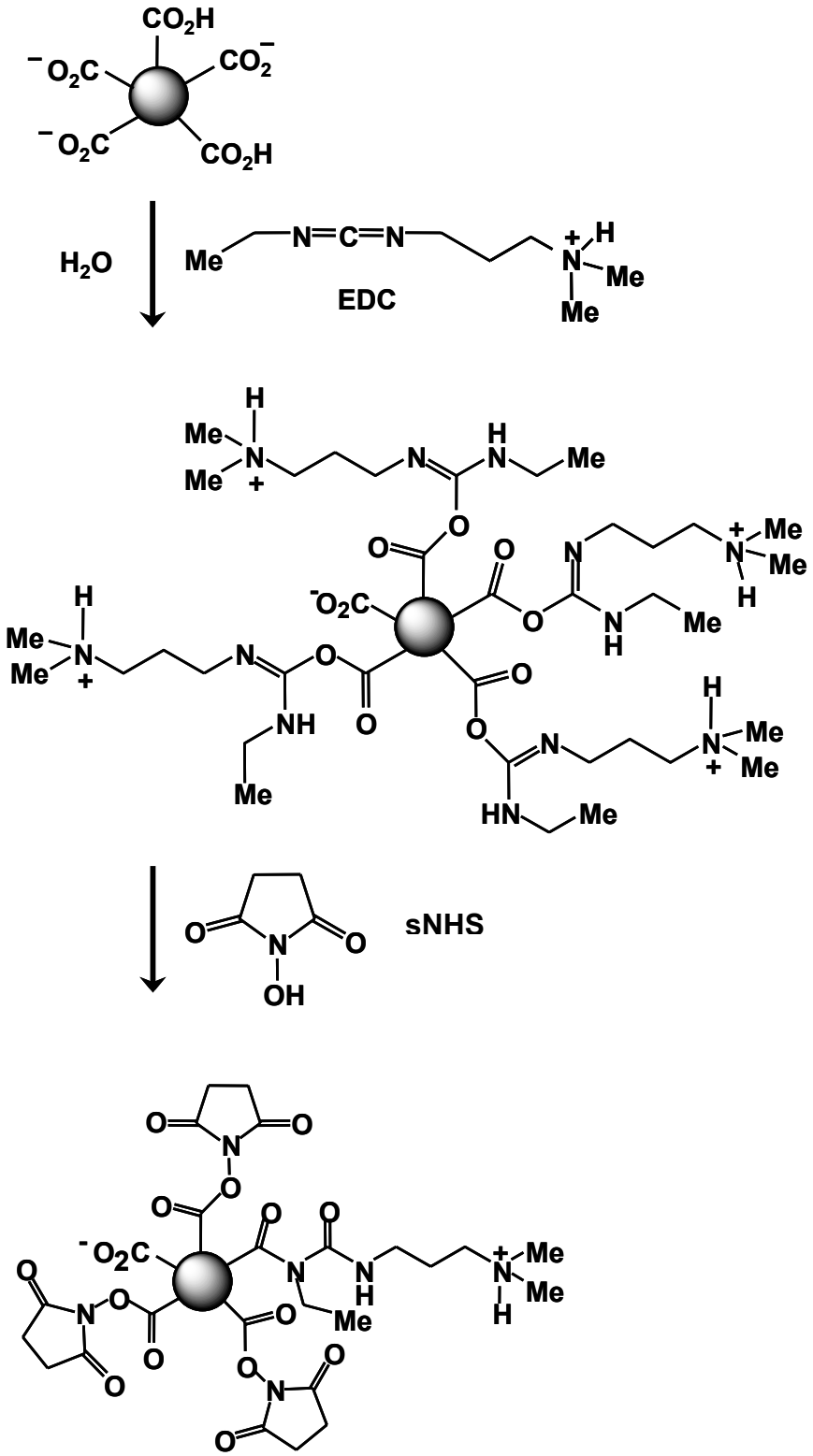

Fig 5.1: Synthetic route to the preparation of BSA-modified polystyrene microspheres.

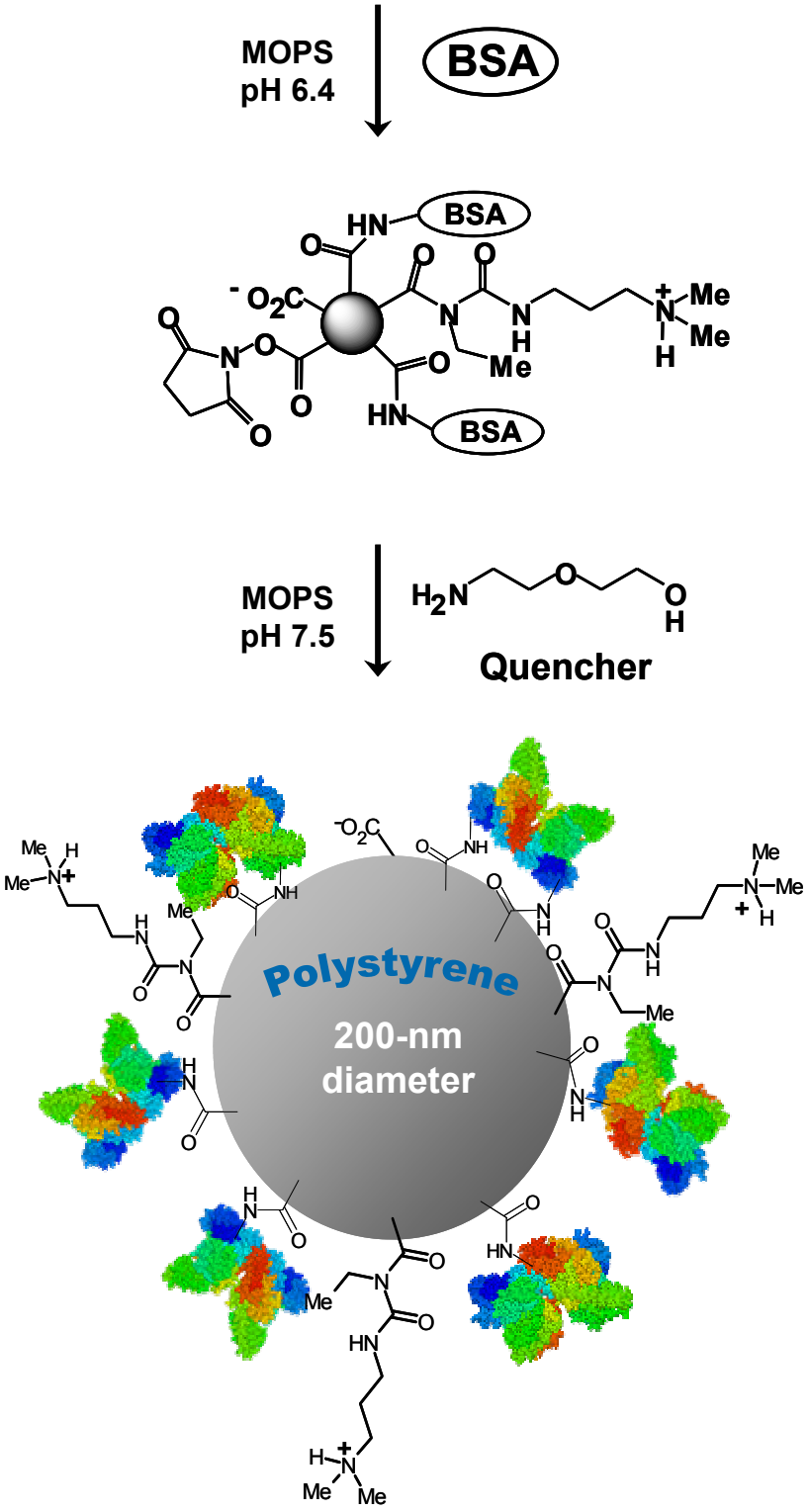

Figure 5.1: cont.

A principal goal of protein characterization at polymer surfaces is to correlate the surface chemical properties of the biomaterial with the biological response elicited in the body or in an assay.[4] As the mechanisms of protein adsorption in actual biological systems are quite complex, a useful starting point is the interrogation of model systems having well-characterized surfaces exposed to an adsorbate under controlled conditions.[1,2] In this chapter, we report the molecular-level detection and behavior of bovine serum albumin (BSA), covalently anchored to latex microspheres, by SFG vibrational spectroscopy and AFM, operated in friction force mode (FFM). In this system, BSA molecules are isotropically distributed as a monolayer over the surfaces of the microspheres in order to stabilize the colloid. This configuration also ensures that SFG data reflects the protein/substrate interface and not protein-protein interactions.

For the last decade, SFG has provided the requisite surface and structural sensitivity needed to interrogate biologically-relevant surfaces and interfaces that are not easily accessible by conventional techniques.[5-8] SFG methods are particularly well-suited to biomaterials research because they can be applied in situ (e.g., under water or buffered solutions) to access spectroscopic information non-destructively. More recently, SFG techniques have been expanded to structural investigations of molecules physically and chemically adsorbed onto spherical particles of various diameter.[9-11] In this study, AFM tribological measurements of beads with and without protein attached complement the SFG spectra.

5.2 Experimental procedures

5.2.1 Materials

The beads, ca. 200 nm in diameter, consist of styrene copolymerized with acrylic acid. Antibodies can be immobilized onto the surface of the bead, either covalently or passively, for use in diagnostic immunoassays to quantitate, for example, the concentrations of drugs of abuse or therapeutic drugs in bodily fluids. After antibody immobilization, the remaining particle surface is typically covered with a protein, such as BSA, to afford colloidal stability to the functionalized bead at physiological pH (pI for BSA = 4.7)[12] and to render the surface resistant to non-specific adsorption of proteins and other moieties present in the clinical sample.[13] To simplify the spectroscopic analysis, the beads studied here have been functionalized with *only* BSA. Antibody adsorption is studied independently in Chapter 6.

5.2.2 Sample preparation

The synthetic route to prepare the BSA-modified beads is shown in Figure 5.1. Latex micro-particles were obtained from Seradyn (Indianapolis) and washed by repeated cycles of centrifugation and resuspension before use. For the experiments reported here, micro-particle carboxyl groups were converted to *N*-hydroxysulfosuccinimide (sNHS) esters by reaction with *N*-ethyl-*N*′-(3-dimethyl-aminopropyl)carbodiimide (EDC) and sNHS. After washing in 50 mM 3-morpholinopropanesulfonic acid (MOPS) at pH 6.4, the activated micro-particles were incubated with BSA (2.5 mg/mg micro-particle) in the same buffer. After 2 hr the mixture was centrifuged (15,000 x *g*, 4 ^{o}C), and the micro-particles washed three times with 50 mM MOPS pH 7.5. The washed micro-particles were stored in the same buffer at 4 ^{o}C.

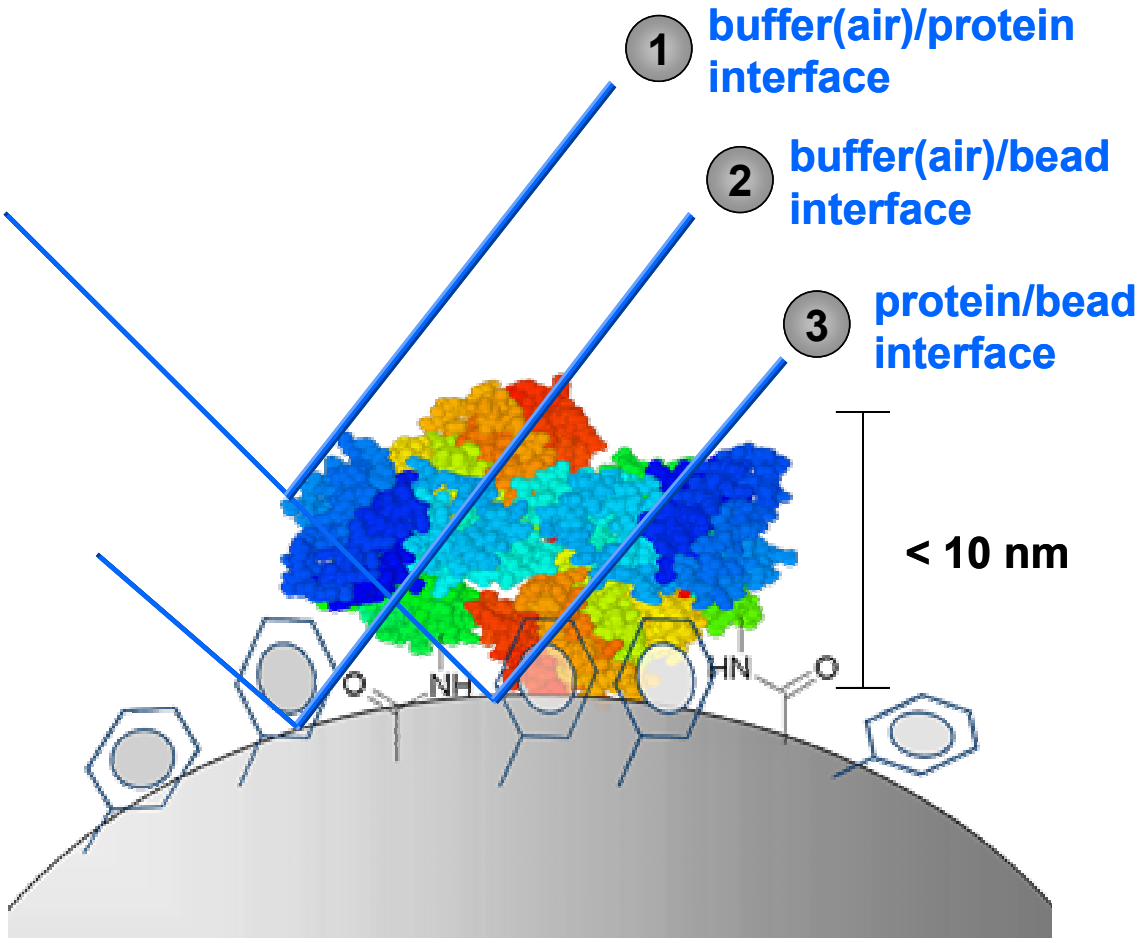

Figure 5.2: SFG spectra of the polymer-protein system are likely a convolution of signal intensity from three interfaces.

5.3 Results and Discussion

5.3.1 SFG analysis of the air/liquid and air/solid interfaces

In these protein-polymer systems, a sum-frequency signal may be generated at up to three interfaces, which are indicated in Figure 5.2. The adsorbed protein layer is not thick enough to attenuate the incoming beams or reflected SFG signal. So, in all likelihood, SFG spectra are a convolution of data from all three interfaces. Figure 5.3 shows SFG spectra for the latex beads with and without immobilized BSA, taken at the air/solid and air/liquid interfaces. Spectra of free BSA molecules in solution or adsorbed onto silica and a polystyrene film are included for comparison. Spectra were collected under the $s_{sfg}s_{vis}p_{ir}$ polarization combination by overlapping 532-nm visible and tunable IR laser pulses on the surface and then measuring the generated sum frequency signal over 2750−3100 cm^{-1}, averaged over three scans and normalized

The spectra in Figure 5.3 have been compared against SFG spectra of the individual buffer components in solution. These molecules give no appreciable signal intensity at the air/liquid interface, presumably because they are randomly oriented. They neither appear in the spectrum of the bare bead, nor should they be convoluted into the spectra of the BSA-modified beads or BSA in buffer. Therefore, the peaks associated with BSA-modified beads at both interfaces originate solely from the phenyl groups in polystyrene and the amino acids residues in BSA molecules that have been specifically immobilized on the surface.

In the air/liquid experiments, ca. 2.0 mL of each solution was transferred to an ultra-clean Petri dish and equilibrated for 30 min before SFG data collection. Figure 5.3(a) shows that the suspension of bare latex beads yields no observable SFG intensity at

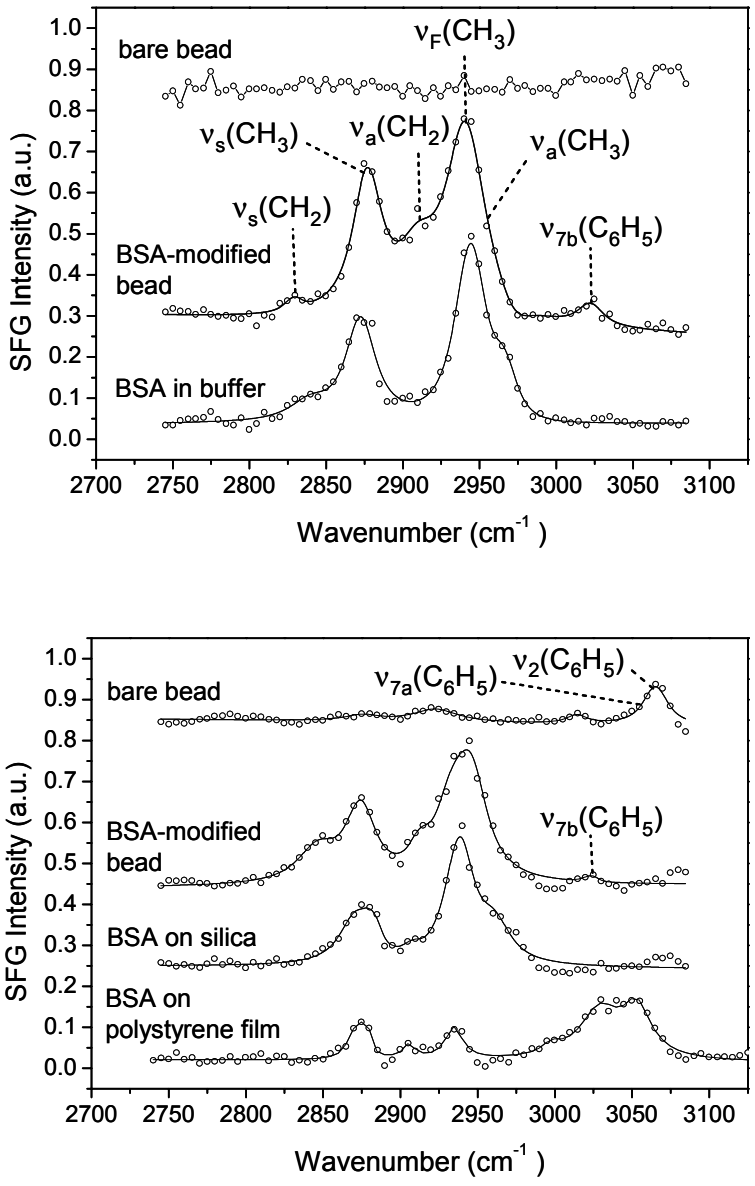

Figure 5.3: SFG spectra (*ssp* polarization combination) of microsphere suspensions with and without BSA covalently attached at the (a) air/liquid and (b) air/solid interfaces. The spectra are referenced to those of BSA in buffer and for BSA adsorbed onto a flat polystyrene film (both 1.0 mg/mL). Symmetric (s), asymmetric (a), Fermi (F), and phenyl bands are identified.

the air/liquid interface over the investigated wavenumber range. The bead is primarily composed of polystyrene, yet the expected normal modes of vibration for the phenyl ring that normally occur between 3050−3100 cm^{-1}, are not observed. Previous SFG studies have characterized free polystyrene surfaces at the air interface and have shown that phenyl rings order away from the surface, although the tilt angle is in question.[16-18] In this experiment, however, beads are suspended in solution and wetted with buffer. In a hydrophilic environment, phenyl rings will lie flat on the surface in order to minimize the interfacial free energy. In addition, the beads likely contain a surface excess of the acrylic acid component of the styrene copolymer. The acrylic acid will hydrogen-bond with interfacial water molecules through its carboxyl groups. A greater density of water molecules near the bead surface will cause further repulsive interactions with the phenyl groups. Under the *ssp* polarization combination, SFG does not access molecular vibrations that are parallel to the surface or those that are randomly ordered.[19] These factors, along with the slight attenuation of the IR beam by buffer, may render the phenyl groups transparent to SFG.

Although the phenyl groups associated with the underlying polystyrene cannot be detected in the case of bare beads at the air/liquid interface, phenyl CH resonances between 3000−3100 cm^{-1} appear in spectra taken from the same beads deposited onto a solid substrate. In these studies, ca. 50 μL of each sample was spun-cast onto a clean silica surface and dried at room temperature. Figure 5.3(b) contains SFG spectra of the resulting latex thin films at the air/solid interface. A symmetric ν_2 phenyl mode can be observed for the bare bead at 3070 cm^{-1}.[16-18] This broadened phenyl resonance also

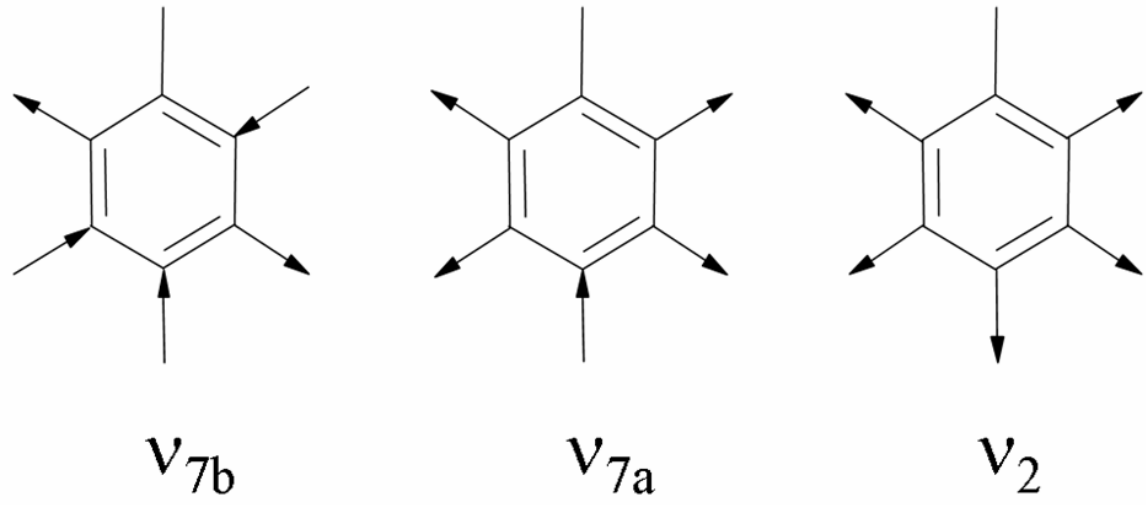

Figure 5.4: Normal modes of vibration assigned to the polystyrene phenyl rings in SFG spectra.

includes a shoulder at 3053 cm^{-1}, which is more clearly identified as a phenyl ν_{7a} stretching mode in the reference spectrum of BSA absorbed onto flat polystyrene.[8] Normal modes of vibration for the phenyl ring are illustrated in Figure 5.4.

In Figure 5.3(a), several CH-stretch modes in the 2800−3000 cm^{-1} range can be identified for BSA-modified beads at the air/liquid interface. Each peak associated with BSA is generated by a convolution of several different amino acid environments. SFG resonances are centered near 2875 (peak), 2915 (shoulder), 2945 (peak), and 2965 cm^{-1} (shoulder) and are assigned to the CH_3 symmetric stretch, CH_2 antisymmetric stretch, a Fermi resonance between the CH_3 symmetric stretch and CH_3-bending overtones, and the CH_3 antisymmetric stretch, respectively.[8,20,21] A further shoulder attributed to the CH_2 symmetric stretch that is well-resolved in the reference spectrum of BSA in buffer is seen at 2840 cm^{-1}. Interestingly, for the BSA-modified bead, a small peak at 3025 cm^{-1} emerges. This peak, which does not appear in spectra of the bare bead or BSA in buffer, most likely originates from the ν_{7b} stretching mode of the beads' phenyl groups. Although weak, hydrophobic interactions between BSA and the underlying polystyrene have coaxed the phenyl rings into a new or possibly more ordered orientation.[8]

In Figure 5.3(b), the SFG spectrum for BSA-modified beads at the air/solid interface contains several resonances in the 2800−3000 cm^{-1} region. As was the case for BSA-modified beads at the air/liquid interface, these peaks originate from BSA molecules immobilized on the bead surface. Similar spectral features are observed in the SFG spectrum of free BSA molecules deposited onto silica. In addition to the CH-stretching modes, the spectrum for the BSA-modified beads contains a phenyl resonance that corresponds to the ν_{7b}-stretching mode at 3025 cm^{-1}. Yet the symmetric ν_2 phenyl

mode, which appears in the spectrum of the bare bead at 3070 cm^{-1}, does not emerge. The ν_{7a} and ν_{7b} phenyl modes are also observed in the spectrum of free BSA molecules deposited onto a polystyrene film, while the ν_2 mode is absent. Covalently-tethered BSA may frustrate symmetric vibrations or alter tilt angles through surface adsorption. The suppression of the symmetric ν_2 vibrational mode in the spectra for both BSA-modified beads and the flat film also suggests complete surface coverage of polystyrene by protein.

Mode strength ratios (A) between the phenyl ν_{7b} stretch, from the bead, and CH stretches, from protein, have been calculated from the fitting parameters for the air/liquid and air/solid interfaces. Given that each bead has the same number density of BSA molecules, the ratios provide a relative indication of the extent of phenyl ordering at the bead/protein interface; for example, in the spectra of BSA-modified beads for both interfacial conditions, $A[\nu_{7b}(C_6H_5)]$ / $A[\nu_s(CH_3)]$ is larger by ca. 30% at the air/solid interface. This can be explained by stronger hydrophobic interactions between polystyrene and BSA at the air/solid interface, relative to those in solution. The change in the bead-protein interaction strength is likely due to an interface-driven reorganization of hydrophilic and hydrophobic domains at the protein surface.[22] Weaker protein-substrate interactions at the air/liquid interface allow the beads' phenyl groups to enjoy a higher degree of vibrational freedom.

5.3.2 AFM topographic and friction analysis

To corroborate the suggestion that protein-substrate interactions are diminished in solution, an atomic force microscope (AFM) was used to compare the surface topography

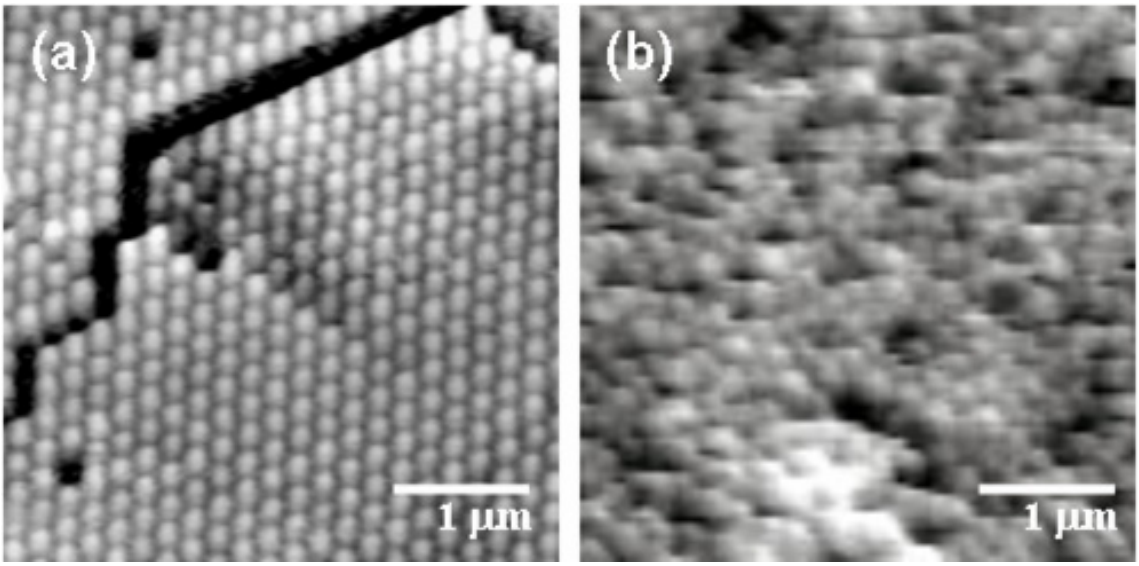

Figure 5.5: Characteristic AFM topographs of dry films of (a) bare and (b) BSA-modified polystyrene microspheres supported on glass slides. The BSA-modified microspheres are randomly ordered, relative to the hexagonal close packed structure formed by the bare microspheres.

and tribology of bare and BSA-modified beads under hydrated and non-hydrated conditions. The AFM has been previously used to investigate protein adsorption on flat polymer substrates.[23] In these experiments, ca. 50 μL of each latex suspension (bare and BSA-modified) was drop-cast onto a pre-cleaned glass slide and dried at room temperature to create a film. The hydrated bead surface was prepared by equilibrating the latex film in buffer solution for 30 min prior to AFM scanning. Data was collected with the beads immersed in buffer. Frictional properties were measured by rastering a silicon nitride AFM tip (ThermoMicroscopes, CA) across the film and spatially recording the torque exerted on the tip by the surface (given in volts by the lateral deflection of the tip), while also acquiring topographical data (shown in Figure 5.5). The resulting voltage is proportional to the coefficient of friction. Data were averaged over several segments of the film where the beads were well-aligned in order to remove topographical artifacts from the friction signal.

AFM topographs of the latex films on silica substrates reveal that the presence of protein at the bead surface directs ordering. While the bare microspheres preferentially pack into a two-dimensional hexagonal array (Figure 5.5(a)), BSA-modified microspheres exhibit random aggregation on a silica substrate (Figure 5.5(b)). The formation of well-defined two-dimensional patterns has been observed for slightly negatively-charged silica and polystyrene beads on various substrates.[24,25] Protein-protein interactions between beads in Figure 5.5(b) may prevent such packing, although the mechanism is not known.

AFM friction values obtained for bare beads at both the air/solid and liquid/solid interfaces are roughly similar. Differences in the frictional properties were recorded

between interfacial conditions, however, for beads with BSA attached. 12 ± 3% and 26 ± 5% increases in the friction signal over the bare state were found for BSA-modified beads at the air/liquid and air/solid interfaces, respectively. The smaller relative increase at the air/liquid interface suggests weaker interaction with the substrate there, as protein that is not strongly adsorbed will more easily shift to dissipate the lateral stress of the tip.

5.4 Conclusion

The molecular-level detection and behavior of BSA covalently bound to polystyrene microspheres at the air/liquid and air/solid interfaces has been reported by SFG vibrational spectroscopy and friction force microscopy. SFG spectra contain signals corresponding to CH-stretching modes at both the air/liquid and air/solid interfaces, indicating that some amino acid residues in BSA are well-ordered. It is also observed that the orientation and ordering of phenyl rings on the microsphere are affected by the presence of BSA. At the air/liquid interface, the interaction of BSA with the substrate orders the phenyl groups in the polystyrene microsphere, relative to the bare microsphere.

At the air/solid interface, however, the SFG signal intensity of the CH-stretch mode for the phenyl rings attenuates after BSA adsorption, disrupting the previously ordered phenyl rings in the underlying, bare surface. AFM images show that bare microspheres self-assemble into a two-dimensional hexagonal packing, whereas protein-modified microspheres randomly aggregate on the silica surface. Differences in surface tribology were also recorded between interfacial conditions for microspheres with and without BSA attached. 12 ± 3% and 26 ± 5% increases in the friction signal over the bare state were found for BSA-modified microspheres at the air/liquid and air/solid

interfaces, respectively. The friction values suggest that BSA interacts more strongly with the microsphere at the air/solid interface.

Additional studies of the conformational changes accompanying the binding of protein fragments to substrate are ongoing. The interaction of polystyrene with BSA and other proteins by SFG and FFM as functions of solvent pH and substrate charge, for example, is currently being explored. These studies will determine if SFG spectra can serve as fingerprints for specific proteins and may help identify significant molecular interactions that direct protein adhesion on the whole.

5.5 Appendix C: AFM gallery of protein deposition on polymer and hydrophilic silica substrates

The SFG results of Chapter 2 indicated that hydrophobic surfaces along with water solvent are required for adsorbed amphiphilic neutral polymers to order. The same polymers were observed to randomly orient at hydrophilic silica/water and hydrophobic PS/methanol interfaces. These orientation effects were believed to be governed by the hydrophobicity of the surface and nature of the solvent via hydrophobic interactions. In this study, AFM topographs of BSA, lysozyme, and fibrinogen on various hydrophobic polymer and hydrophilic silica substrates are presented to determine how the nature of the protein may affect its adsorption behavior.

Figure 5.6 is a cartoon which highlights differences in the behavior of soft and hard proteins. Soft proteins are those which denature easily when they adsorb to a

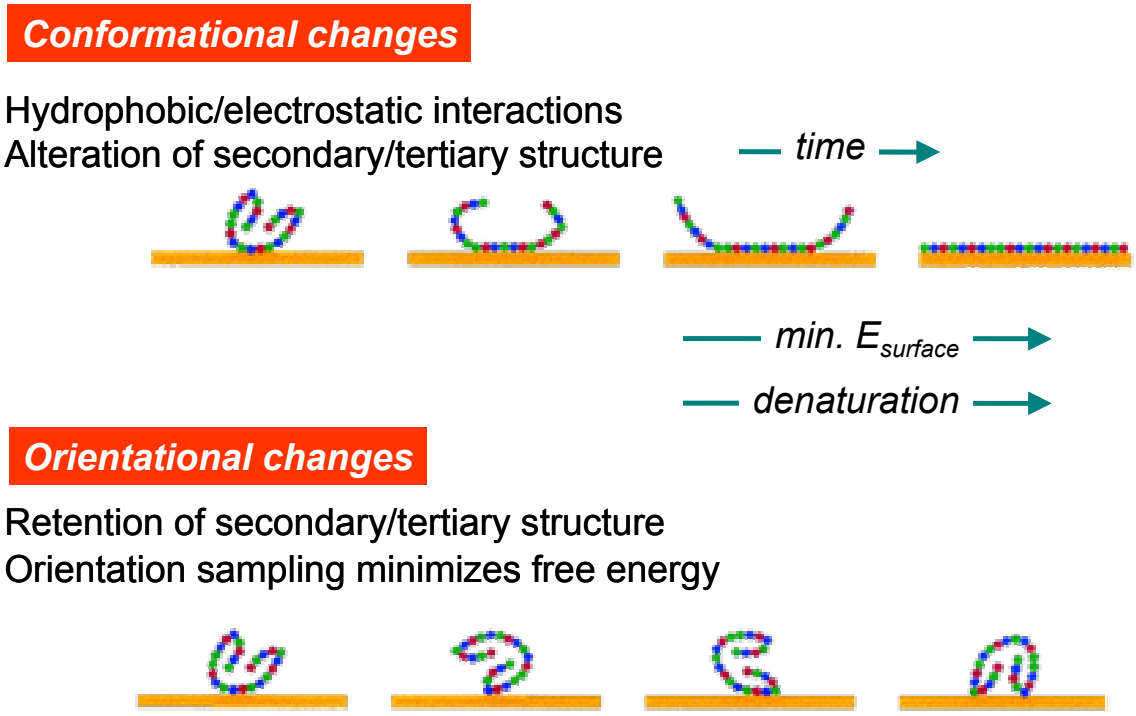

Figure 5.6: Cartoons of the water-mediated conformational and orientational changes accompanying protein adsorption. The nature of the protein (soft vs. hard) and the surface energy of the substrate strongly influence the strength of adhesion and rate of denaturation.

surface. Hard proteins, which tend to have a larger number of internal intermolecular forces, will retain their secondary and tertiary structure upon adsorption. However, the surface energy of the substrate will dictate the strength of adhesion and the extent and rate of protein denaturation.

Samples were prepared by exposing the silica and polymer substrates to 0.008 mg/L solutions of protein overnight. The samples were removed and rinsed with water prior to contact-mode imaging in air. The gallery of AFM images begins with Figure 5.7(a), which shows reference topographic and friction images of silica and polystyrene surfaces. The images have an expectedly low rms roughness. It is not possible to identify protein or protein clusters in the images of BSA adsorbed on hydrophilic silica, shown in Figure 5.7(b). The images in Figure 5.7(b) are slightly rougher than the reference images due to salts in the buffer, which still adhere to the surface after rinsing.

Recall that protein adsorption is normally stabilized through hydrophobic interactions, which is perhaps why lysozyme can be resolved on polystyrene in Figure 5.8(d), but not on silica or polyethylene glycol – a typical non-fouling substrate. Even more exquisite ordering patterns are observed in Figure 5.9(b), which contains magnified images of fibrinogen adsorbed on polystyrene. The long-arm molecular structure of fibrinogen, a blood clotting protein, is shown Figure 5.9(a) and may help explain these self-assembled patterns. To confirm the deposition behavior observed on polystyrene, fibrinogen was also imaged on another hydrophobic polymer surface: polyethylene. While there is no overall order to the protein deposition in Figure 5.10, multilayers are created. The surface energy of polyethylene is 5 dyn/cm lower than that of polystyrene. Thus, differences in protein/substrate interaction forces may explain this behavior.

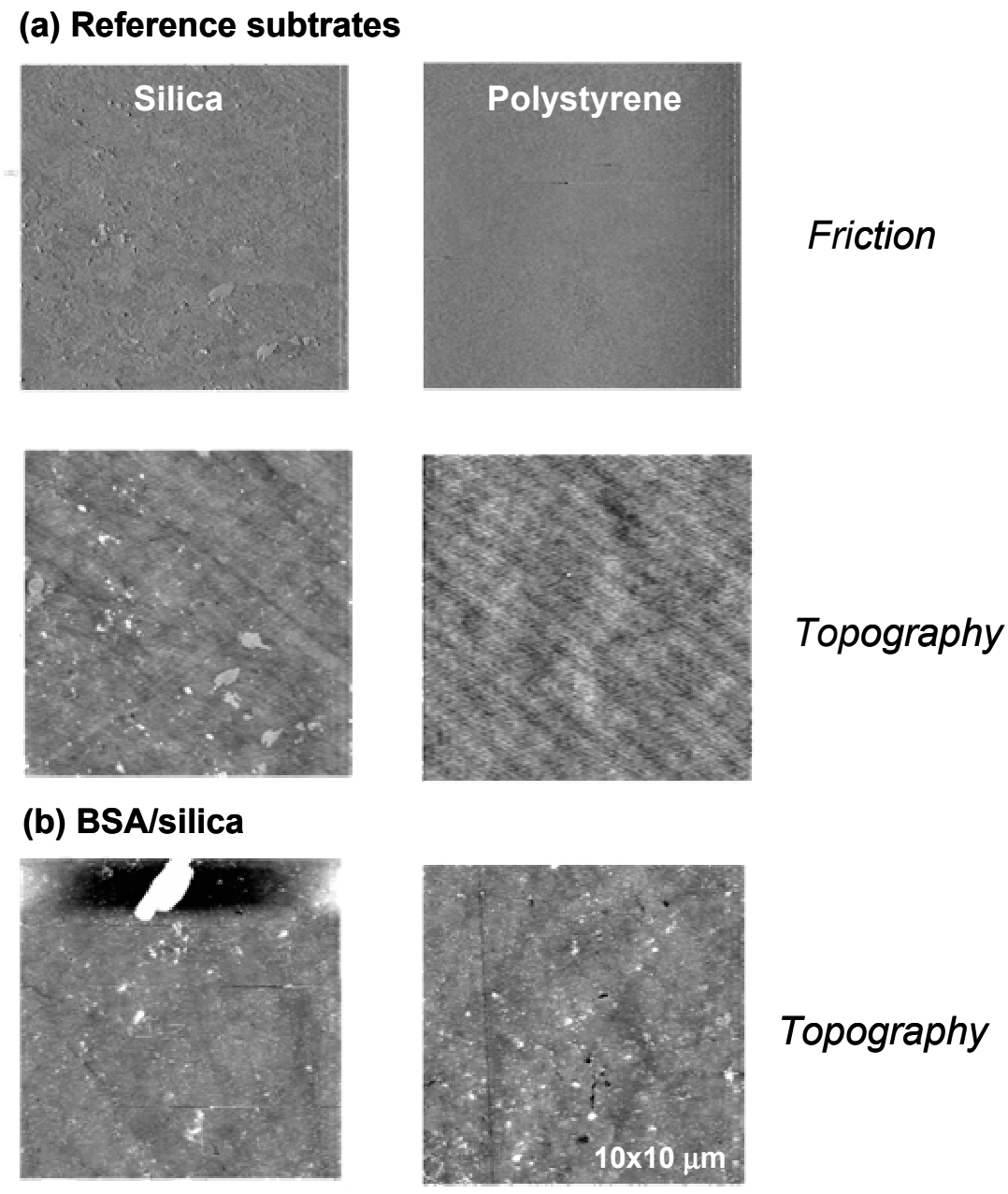

Figure 5.7: AFM topography and friction images of (a) bare silica and polystyrene references and (b) topography images of BSA adsorbed onto silica. BSA, a soft protein, is not well-resolved in the image acquired on silica. (Note: bacteria appear to be imaged in the upper portion of the BSA/silica topograph on the left).

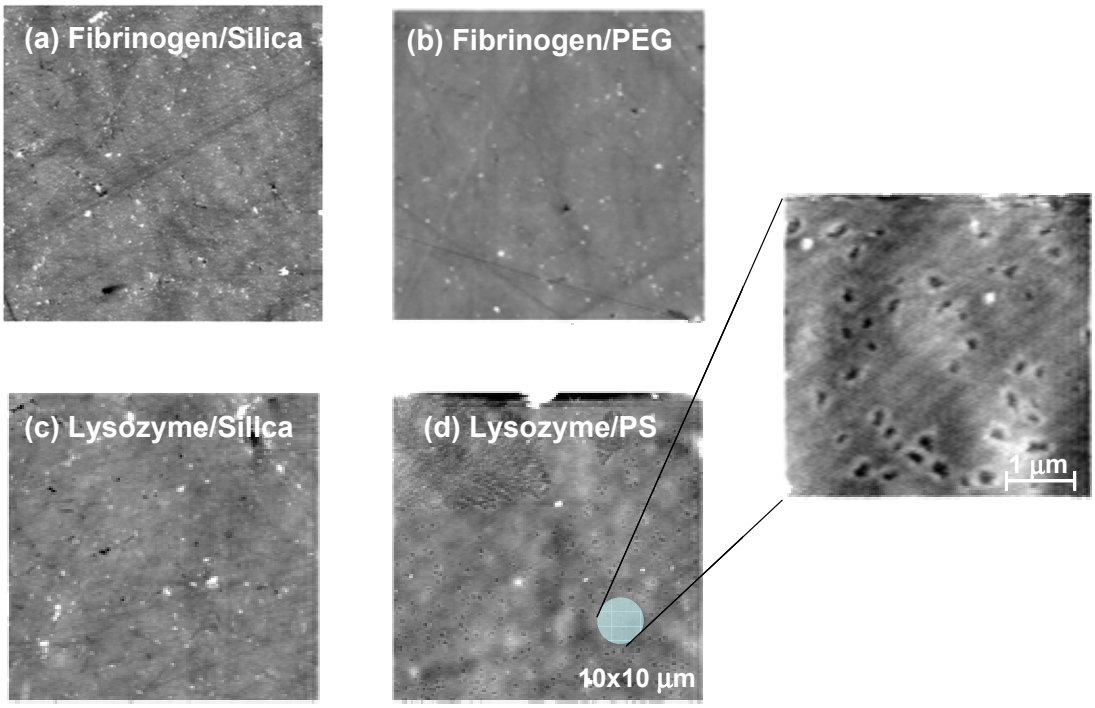

Figure 5.8: AFM topographs of hard proteins: fibrinogen on (a) silica and (b) polyethylene glycol (PEG) and lysozyme on (c) silica and (d) polystyrene. No protein is imaged on silica, a standard hydrophilic substrate or PEG, a non-fouling polymer surface. Lysozyme clusters are imaged, however, on hydrophobic PS (shown in the blow-up).

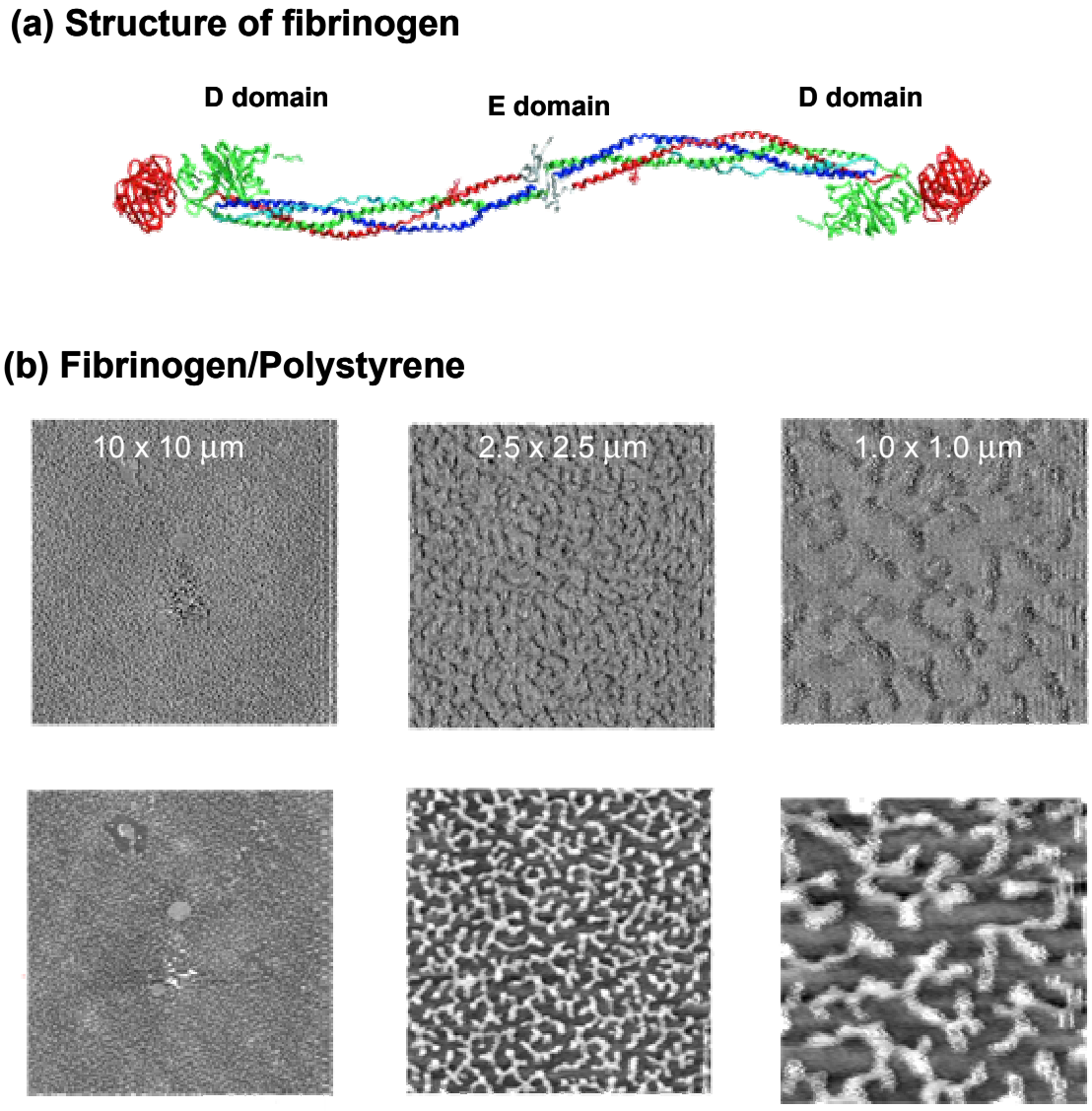

Figure 5.9: (a) Domain-labeled structure of fibrinogen and (b) AFM friction and topography images (top and bottom, respectively) of fibrinogen deposited onto a polystyrene film. Fibrinogen, a hard protein involved in blood clotting, has two long arms which give rise to the patters resolved on the hydrophobic substrate above.

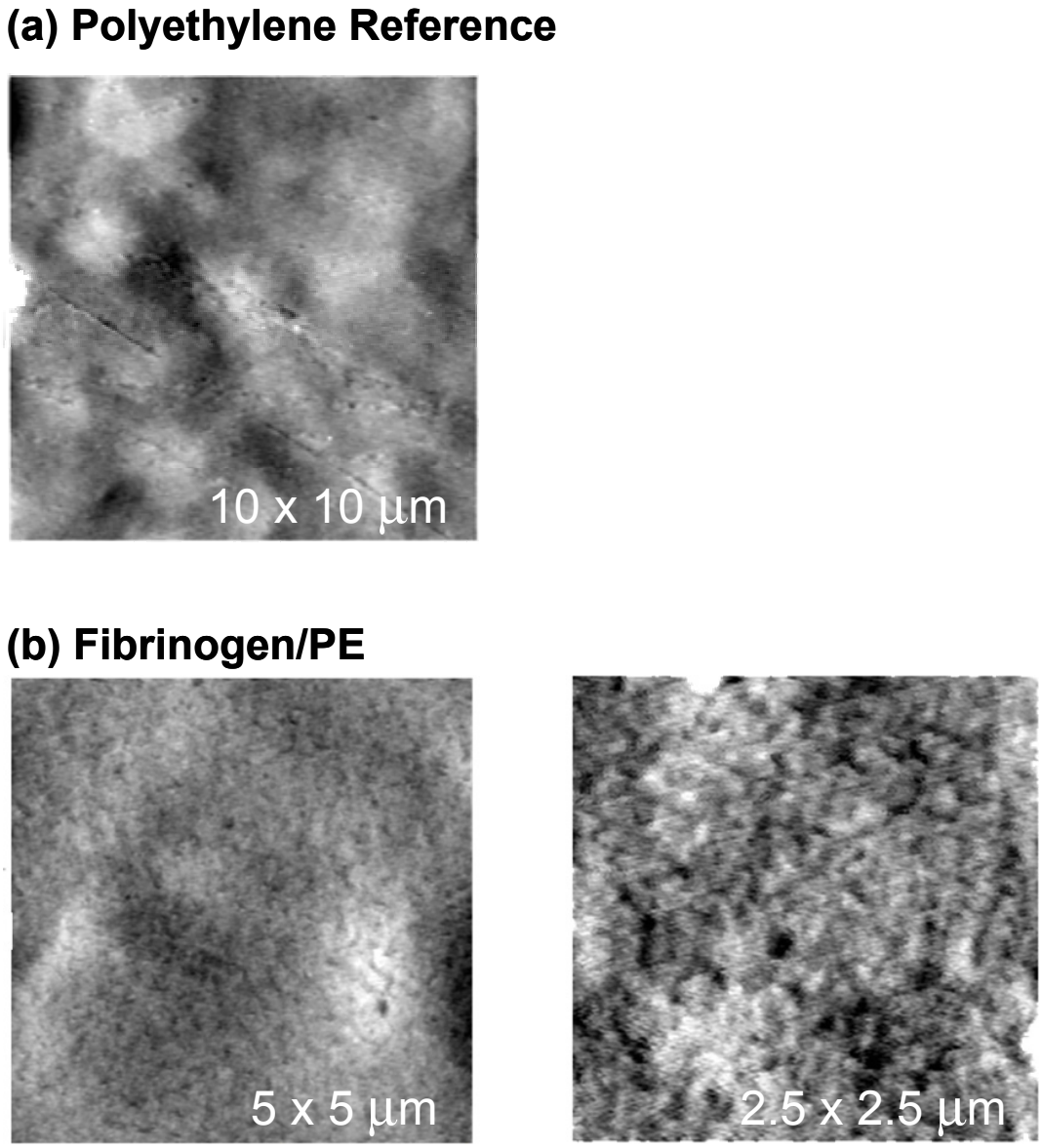

Figure 5.10: AFM topographs of (a) bare polyethylene (PE) and (b) fibrinogen adsorbed on PE at the indicated scan areas. While the exquisite ordering observed in polystyrene is not observed on PE, rough protein multilayers do form.

References

(1) *Proteins at Interfaces II: Fundamentals and Applications*; Horbett, T. A., Brash, J. L., Eds.; American Chemical Society: Washington, D. C., 1995.

(2) *Proteins at Interfaces: Physicochemical and Biochemical Studies*; Brash, J. L., Horbett, T. A., Eds.; American Chemical Society: Washington, D. C., 1987.

(3) Castner, D. G.; Ratner, B. D. *Surf. Sci.* **2002**, *500*, 28.

(4) Andrade, J. D.; Hlady, V. *Adv. Polym. Sci.* **1986**, *79*, 1.

(5) Chen, Z.; Ward, R.; Tian, Y.; Baldelli, S.; Opdahl, A.; Shen, Y. R.; Somorjai, G. A. *J. Am. Chem. Soc.* **2000**, *122*, 10615.

(6) Gracias, D. H.; Chen, Z.; Shen, Y. R.; Somorjai, G. A. *Acc. Chem. Res.* **1999**, *32*, 930.

(7) Chen, Q.; Zhang, D.; Somorjai, G.; Bertozzi, C. R. *J. Am. Chem. Soc.* **1999**, *121*, 446.

(8) Kim, J.; Somorjai, G. A. *J. Am. Chem. Soc.* **2003**, *125*, 3150.

(9) Clark, H. A.; Campagnola, P. J.; Wuskell, J. P.; Lewis, A.; Loew, L. M. *J. Am. Chem. Soc.* **2000**, *122*, 10234.

(10) Kawai, T.; Neivandt, D. J.; Davies, P. B. *J. Am. Chem. Soc.* **2000**, *122*, 12031.

(11) Ma, G.; Allen, H. C. *J. Am. Chem. Soc.* **2002**, *124*, 9374.

(12) Peters, T. J. *All about Albumin: Biochemistry, Genetics, and Medical Applications*; Academic Press: San Diego, 1996.

(13) Ortega-Vinuesa, J. L.; Bastos-González, D. *J. Biomater. Sci. Polym. Edn.* **2001**, *12*, 379.

(14) Shen, Y. R. *Nature* **1989**, *337*, 519.

(15) Shen, Y. R. *Surf. Sci.* **1994**, *299/300*, 551.

(16) Gautam, K. S.; Schwab, A. D.; Dhinojwala, A. *Phys. Rev. Lett.* **2000**, *85*, 3854.

(17) Zhang, D.; Dougal, S. M.; Yeganeh, M. S. *Langmuir* **2000**, *16*, 4528.

(18) Briggman, K. A.; Stephenson, J. C.; Wallace, W. E.; Richter, L. J. *J. Phys. Chem. B* **2001**, *105*, 2785.

(19) Wei, X.; Hong, S.-C.; Zhuang, X.; Goto, T.; Shen, Y. R. *Phys. Rev. E* **2000**, *62*, 5160.

(20) Gragson, D. E.; McCarty, B. M.; Richmond, G. L. *J. Am. Chem. Soc* **1997**, *119*, 6144.

(21) Gragson, D. E.; Richmond, G. L. *J. Phys. Chem. B* **1998**, *102*, 3847.

(22) Israelachvili, J.; Wennerstroem, H. *Nature* **1996**, *379*, 219.

(23) Chen, X.; Davies, M. C.; Roberts, C. J.; Tendler, S. J. B.; Williams, P. M.; Davies, J.; Dawkesand, A. C.; Edwards, J. C. *Langmuir* **1997**, *13*, 4106.

(24) Rajeshwar, K.; de Tacconi, N. R.; Chenthamarakshan, C. R. *Chem. Mater.* **2001**, *13*, 2765.

(25) Fischer, U. C.; Heimel, J.; Mass, H.-J.; Hartig, M.; Hoeppener, S.; Fuchs, H. *Surf. Interface Anal.* **2002**, *33*, 75.

Chapter 6

Surface Analysis of Antibody- and Surfactant-Modified Latex Microspheres

6.1 Introduction

As was remarked in Chapter 5, protein adsorption onto polymer surfaces is a highly active area of research due to its relevance in both biology and medicine and the desire to apply the data acquired from these studies in surface-based biotechnologies.[1-3] Although their specific aims may vary, the characterization and manipulation of adsorbed proteins on solid surfaces with increasingly greater sensitivity and control has been a common goal among researchers. For example, the complete removal of adsorbed proteins from surfaces is generally required in the medical and food industries, since even a small amount of deposited protein will give rise to the subsequent adsorption of fibrous proteins, leading to adverse biological consequences.[4,5] In contrast, the controlled immobilization of enzymes and antibodies at interfaces is required in biosensor development for disease diagnostics and drug detection.[6-8]

The polymer microspheres (beads) of micron- to nanometer-sized diameter that were introduced in Chapter 5 have been popularly used as solid substrates for biomolecular immobilization. These beads are primarily made of polystyrene and another polymer containing either carboxyl, amine, or hydroxyl groups as a minor component in the bead formulation.[9-11] These functional groups are used to selectively and specifically adsorb various biomolecules, such as proteins and DNA, via direct chemical coupling.[12,13] Although antibodies were not present on the beads studied in Chapter 5 (to simplify the spectral analysis), IgG antibodies are normally loaded onto the bead for use in drug assays.[9,10] The accuracy and limit of detection for these systems depend primarily on the structure and orientation of biomolecules adsorbed at the surface.

Various techniques, including light scattering, spectroscopy, microscopy, and flow-adhesion assays have been used to structurally characterize bead adsorbates.[9,12-15] Although these techniques have produced valuable information regarding the chemical structure and concentration of adsorbates, more detailed structural information at the molecular level is anticipated. Over the last decade, SFG has been used to create chemical and physical pictures of the interfacial structure and behavior of molecules of various size -- both small (e.g., water, acetonitrile, and carbon monoxide) and large (e.g., self-assembled monolayers, polymers, and proteins) under diverse environmental conditions.[16-26] SFG studies have been expanded to structural investigations of molecules physically and chemically adsorbed onto spherical particles of various size.[16,27-29] AFM has also contributed to protein research as a tool to characterize biological surfaces in situ with molecular resolution.[30-33]

In this chapter, we have expanded our surface investigations to beads which have been modified by either covalent linking of immunoglobulin G (IgG) or BSA at different values of pH or beads onto which a Pluronic surfactant has been physical adsorbed. Pluronics are normally used to minimize subsequent protein adsorption from blood serum onto the bead following modification with BSA and IgG. The beads studied in this chapter are again ca. 200 nm in diameter and consist of styrene copolymerized with a small amount of acrylic acid. The structural characterization of these beads in the presence of macromolecular adsorbates using SFG and AFM follows.

6.2 Experimental procedures

6.2.1 Sample Preparation

Latex microspheres with a diameter of ca. 200 nm were obtained from Seradyn (Indianapolis, IN) and washed by repeated cycles of centrifugation and resuspension before use. The bare microspheres consist of a blend of polystyrene and polyacrylic acid (1.5 – 3.0 w/w %). All other chemicals were purchased from Sigma-Aldrich. Beads with Pluronic were prepared by incubating bare microsphere suspensions (10 ml, 1.0 % (w/v)) at room temperature overnight in the presence of 0.1 % (w/v) Pluronic F127. Excess Pluronic was removed by repeated cycles of centrifugation/resuspension. To covalently link BSA and IgG, carboxyl groups on the microspheres were converted to *N*-hydroxysulfosuccinimide (sNHS) esters by reaction with *N*-ethyl-*N*′-(3-dimethyl-aminopropyl)carbodiimide (EDC) and sNHS.[36] After washing, the microspheres were resuspended in 50 mM 3- morpholinopropanesulfonic acid (MOPS) at either pH 6.4 (IgG

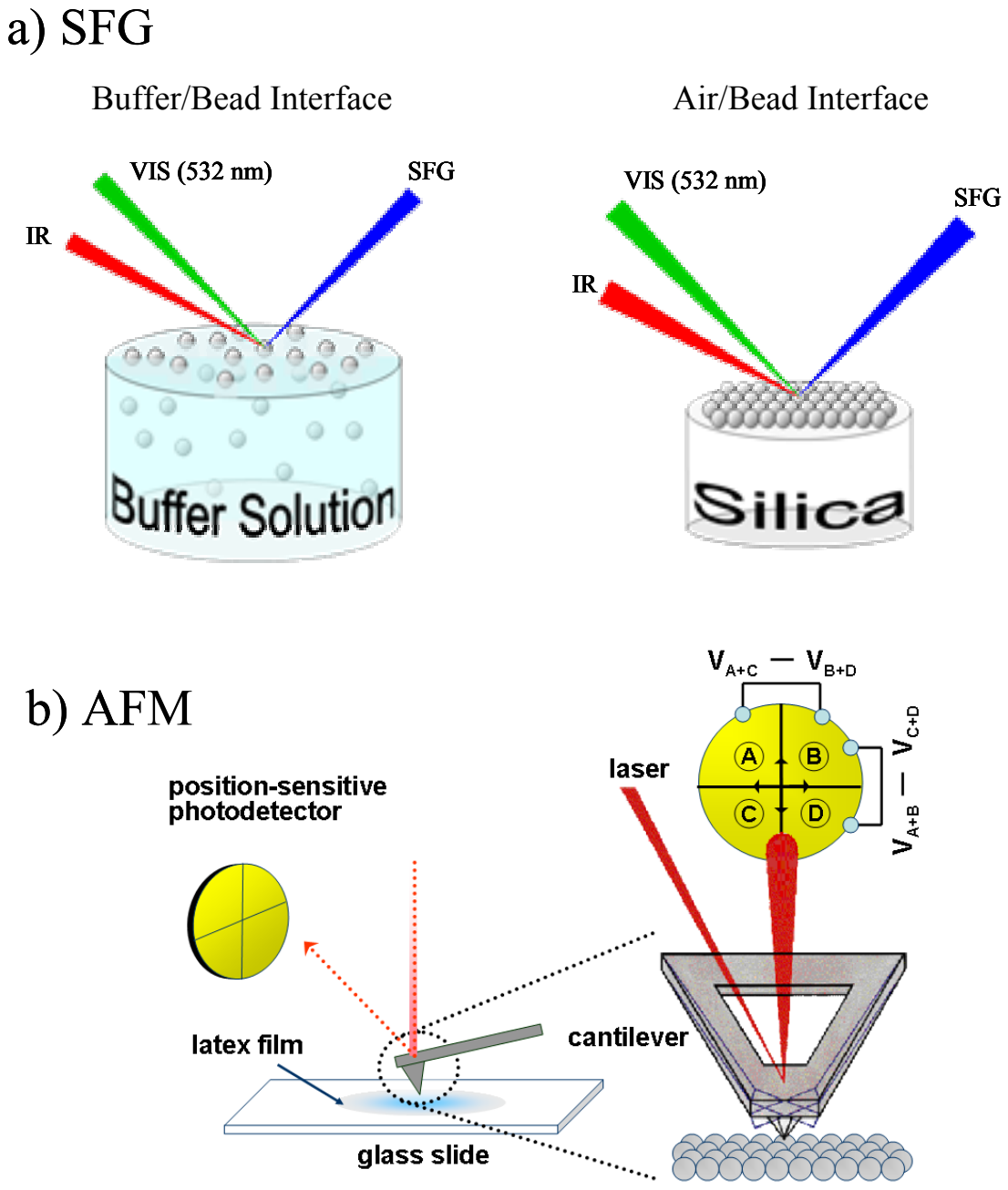

Figure 6.1: Schematic of (a) SFG and (b) AFM data collection at the buffer/bead and air/bead interfaces.

BSA) or at pH 7.2 (IgG), followed by addition of the corresponding protein solutions (10.0 μg/mg). After incubation for 1.5 hr, an excess of 2-aminoethoxyethanol (AEO) was added to each mixture. After overnight incubation, the mixtures were centrifuged (15,000 x *g*, 4 ^{o}C) and washed three times with 50 mM MOPS, 0.09 % (w/v) NaN_3, pH 7.5. The resuspended beads (1.0 % (w/v)) were stored in the same buffer at 4 ^{o}C until analysis. Assuming maximum footprint areas of 11,000 and 3200 Å^2 for IgG and BSA, respectively, about 5,000 IgG and 17,000 BSA molecules cover the bead surface.

6.2.2 SFG and AFM experimental setups

The following sample components were independently examined for comparative SFG peak assignments: 1) polystyrene and polyacrylic acid films, 2) surface modifying agents (EDC and NHS), 3) buffer chemical (MOPS), 4) Pluronic F127 and its block copolymer units (polypropylene oxide and polyethylene oxide), and 5) BSA and IgG in pH 6.4 and 7.2 buffer solutions.

For SFG and AFM studies at the air/bead interface, ca. 10 μL of each sample was transferred to a clean silica surface, uniformly spread out by spinning, and dried at room temperature. For experiments at the buffer/bead interface, ca. 2 mL of each solution was transferred to an ultra-clean Petri dish and allowed at least 30 min to equilibrate prior to SFG data collection. Schematics of the experimental set up for SFG and AFM at both interfaces are illustrated in Figure 6.1.

6.3 Results and Discussion

6.3.1 SFG Analysis of the buffer/bead interface

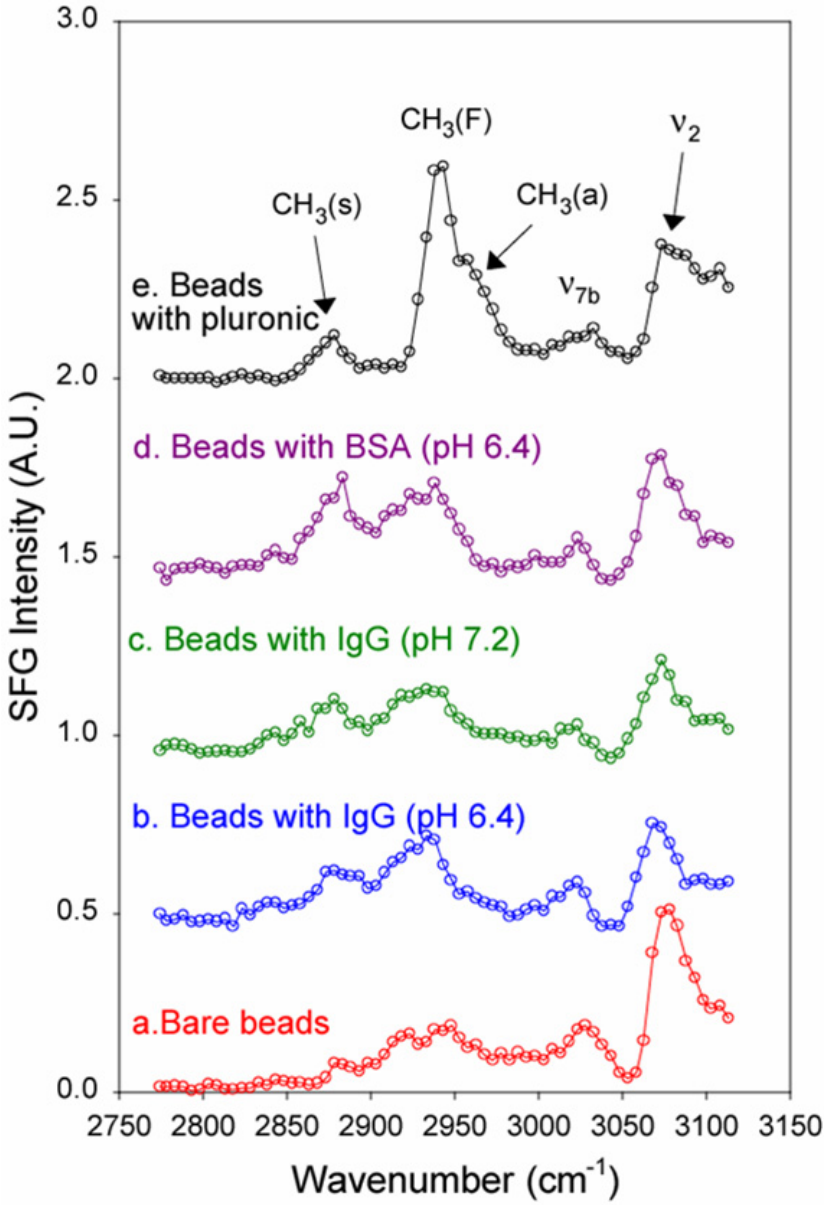

Figure 6.2: SFG spectra for (a) bare beads, (b) beads with IgG immobilized at pH 6.4, (c) beads with IgG immobilized at pH 7.2, (d) beads with BSA immobilized at pH 6.4, and (e) beads with physisorbed Pluronic at the buffer/bead interface.

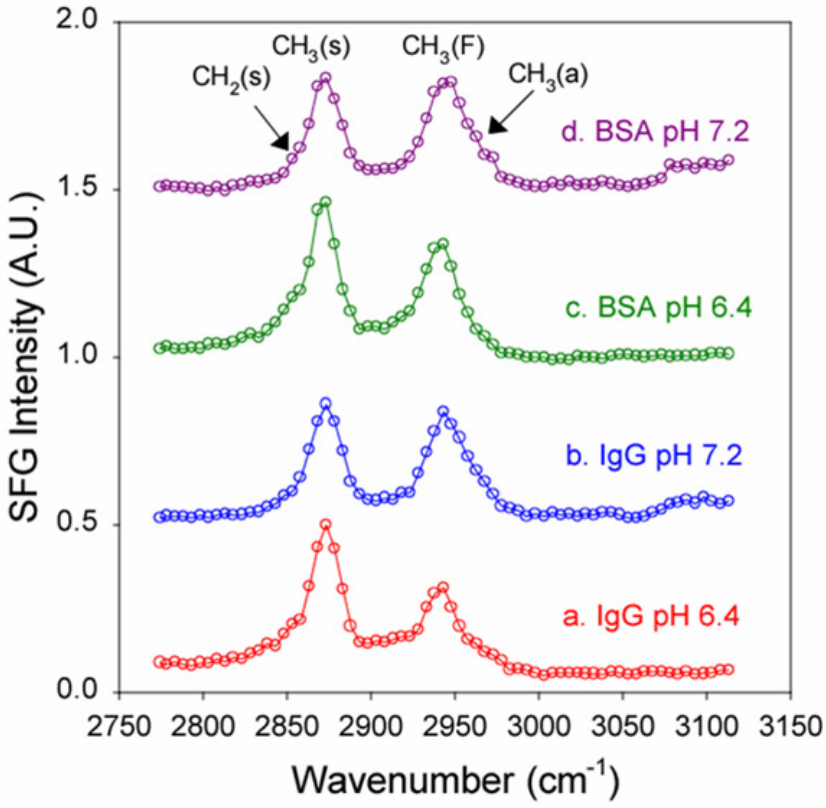

Figure 6.3: SFG spectra for IgG and BSA at the air/liquid interface at pH 6.4 and 7.2.

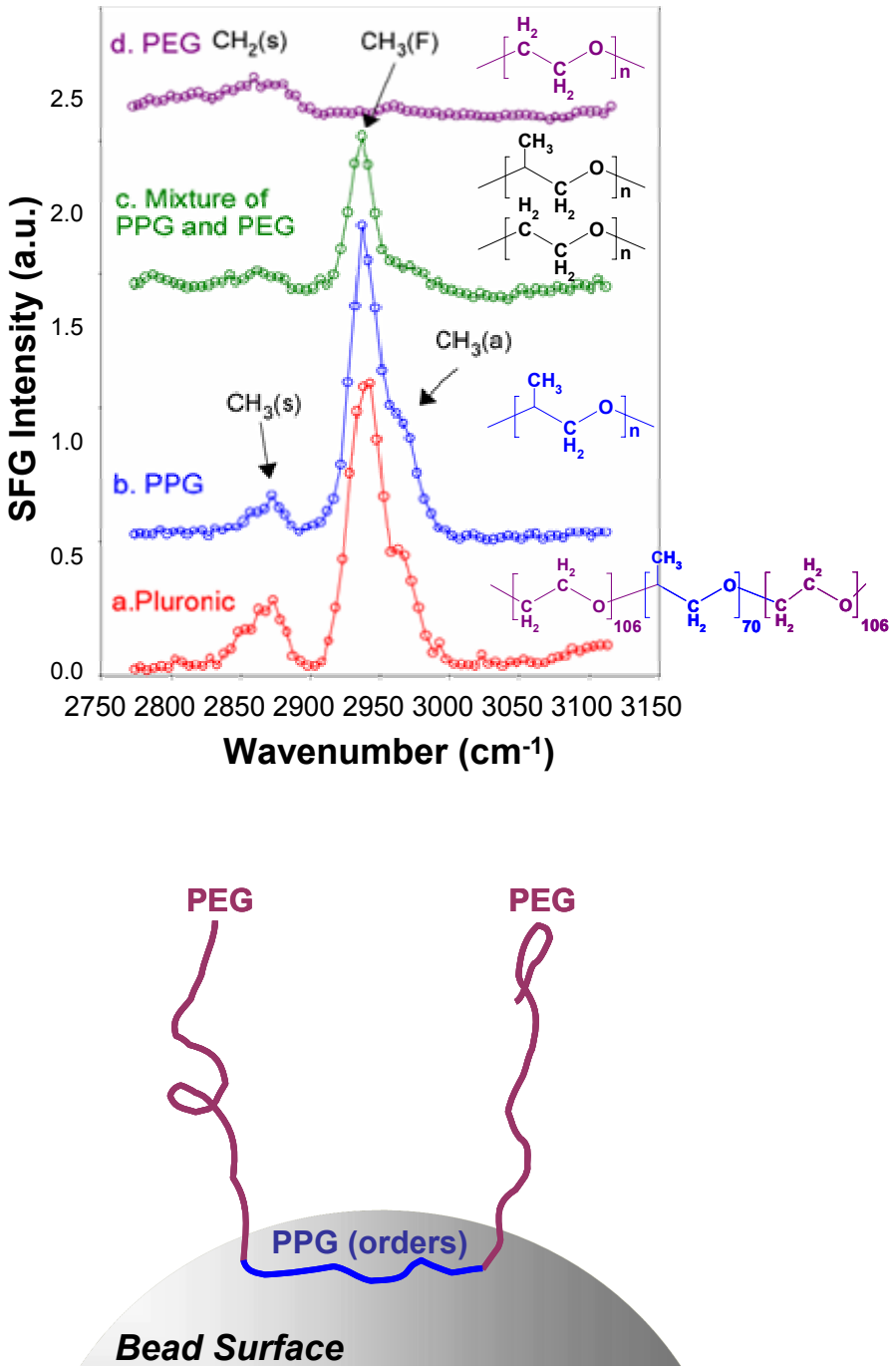

Figure 6.4: SFG spectra for (a) Pluronic, (b) PPG, (c) a 1:1 mixture of PPG and PEG, and (d) PEG at the air/liquid interface. A cartoon of the structure of the adsorbed Pluronic is illustrated below.

Figure 6.2 presents SFG spectra in the CH-stretch region for beads that are unmodified, covalently linked with IgG at pH 6.4 and 7.2, covalently linked with BSA at pH 6.4, and physisorbed with Pluronic at the buffer/bead interface. For comparison, SFG spectra obtained from reference materials (i.e., IgG, BSA, Pluronic, polypropylene glycol (PPG), polyethylene glycol (PEG), and a 1:1 mixture of PPG and PEG) obtained at the air/liquid interface are also presented in Figures 6.3 and 6.4, respectively.

All beads and reference samples generate SFG signal intensity, with the emergence of several CH-stretch modes in the range of 2800 to 3100 cm^{-1}. In the aliphatic CH-stretching frequency region (2800 to 3000 cm^{-1}), four CH-stretch modes are generally identified around 2850 (shoulder), 2875 (peak), 2950 (peak), and 2965 cm^{-1} (shoulder). These modes are assigned to the CH_2 symmetric stretch (CH_2(s)), CH_3 symmetric stretch (CH_3(s)), CH_3 Fermi resonance (CH_3(F)), and CH_3 asymmetric stretch (CH_3(a)), respectively.[16,17,24,25] These peaks originate from surface methyl and methylene groups present in either the polystyrene backbone or from macromolecules adsorbed on the beads (i.e., BSA, IgG, and Pluronic). SFG signals from the polymer backbone, however, are generally weaker compared to those generated by branched side chains.[37]

In addition, SFG spectra obtained from the bead samples in Figure 6.2 contain spectral features in the range of 3000 to 3100 cm^{-1}, which are attributed to aromatic CH-stretch modes.[16,17,38,39] Although most proteins contain aromatic amino acid residues, previous SFG studies in our group using *per*-deuterated polystyrene thin films have shown that the CH-stretch modes of phenyl rings in polystyrene comprise the majority of SFG signal intensity in this frequency region.[17] Large and small peaks around 3075 and 3025 cm^{-1} are responsible for the ν_2 and ν_{7b} phenyl modes, respectively.[16,17,38,39] The

intensity of the ν_2 mode is affected by the presence of adsorbed molecules. This is attributed to changes in the ordering and orientation of phenyl rings in the underlying polystyrene substrate upon molecular adsorption via intermolecular interactions (i.e., van der Waals forces) between the phenyl rings and adsorbates.

6.3.2 SFG analysis of unmodified (bare) beads

The SFG spectrum obtained from bare polystyrene beads in Figure 6.2(a) contains CH-stretch signals around 2920 and 2945 cm^{-1}. Although the origin of these vibrational modes is not clear, they may be due to CH_2-stretch modes from the polystyrene backbone. More importantly, Figure 6.2(a) shows additional CH-stretch modes around 3075 and 3025 $cm^{-1}$from phenyl rings in the bead, indicating that phenyl rings are oriented with their dipole components directed along the surface normal. These peaks, however, did not appear in SFG analyses of the bare bead samples at the buffer/bead interface in Chapter 5.[16]

The lack of spectral features in previous bare bead samples was interpreted to mean that the beads' phenyl rings were lying parallel or nearly flat to the bead surface – an orientation which the SFG is insensitive to using the $s_{sum}s_{vis}p_{ir}$ beam polarization combination. The phenyl groups were believed to lie flat due to the aggregation of water molecules via hydrogen bonding to the carboxyl groups of polyacrylic acid present at the bead surface. The accumulation of water molecules at the surface would also attenuate the IR beam, lowering SFG signal intensity.

As described in Chapter 1, two factors govern SFG signal intensity: the number density of molecules and their average ordering/orientation at the surface. If the relative

bulk concentrations of styrene and acrylic acid used to synthesize the copolymer beads is not consistent between samples, their concentrations at the bead surface will also be affected. Previous studies in our group involving polymer blends, with each component having a different hydrophobic character, have shown that even a small amount (ca. less than 2% wt) of one component in the bulk can become the dominant component at the surface.[22]

Slight changes in the bulk composition are believed to severely affect the surface composition, since the more hydrophobic (or hydrophilic) constituents preferentially segregate to the surface depending on the interfacial nature of the environment. Moreover, the surface number density is intimately related to the orientation and ordering of molecules at interfaces, as observed in both binary methanol-water and acetonitrile-water systems, as well as *atactic* polypropylene and *atactic* polyethylene-*co*-propylene rubber blends.[37,40,41] XPS analysis (reference Figure 6.6) shows that the current sample contains nearly twice as much atomic oxygen in the near-surface region than the previous sample, indicating a greater interfacial concentration of polyacrylic acid. The results suggest that the appearance of the SFG signals associated with phenyl groups is caused by ordering and orientation effects rather than a higher surface density of polystyrene.

6.3.3 SFG analysis of beads modified with IgG

SFG spectra for beads with covalently adsorbed IgG at pH 6.4 and 7.2 are shown in Figure 6.2(b) and (c), respectively. Despite the different pH values used during immobilization, beads with immobilized IgG do not show discernable differences in the CH-stretch region (2800 to 3000 cm^{-1}). SFG spectra of IgG-modified beads at either pH

condition contain an SFG signal for the CH-stretch mode near 3075 cm^{-1} (ν_2 mode) from the underlying phenyl rings. SFG signal strength for the ν_2 mode is weaker, relative to the intensity observed from bare beads (see Figure 6.2(a) compared to Figure 6.2(b) and (c)). Although *free* IgG molecules at the buffer/air interface at the same pH values used during immobilization (6.4 and 7.2) yield SFG signals at nearly identical positions, their CH_3- and CH_2-stretch modes differ slightly in relative intensity (see Figure 6.3(a) and (b)). Such a result implies a structural rearrangement in the protein after aggregation at the surface due to pH-dependent electrostatic interactions. A change in tertiary and secondary structures will cause the protein to expose different amino acid residues at the surface and affect the ordering of those exposed amino acid residues.

6.3.4 SFG analysis of beads modified with BSA.

SFG spectra of covalently-linked BSA at pH 6.4 at the bead/buffer interface and free BSA at pH 6.4 and 7.2 at the air/buffer interface are shown in Figures 6.2(d) and 6.3, respectively. Compared to IgG-modified beads, SFG spectra from beads modified with BSA contain signals with a large intensity in the 2800 to 3000 cm^{-1} range. As in the case of IgG, attenuation of the SFG signal intensity for the ν_2 mode around 3075 cm^{-1} is observed. SFG spectra of free BSA obtained at the buffer/air interface for different pH values show differences in relative peak intensity for the CH_3- and CH_2-stretch modes, presumably due to different tertiary structures at the interface (Figure 6.3).

6.3.5 SFG analysis of beads with adsorbed Pluronic

The SFG spectrum for beads adsorbed with Pluronic is shown in Figure 6.2(e). The general structure of this class of triblock copolymers consists of a central section of polypropylene glycol (PPG) units flanked on both ends by polyethylene glycol (PEG). Previous SFG studies, such as those in Chapter 2, have revealed that hydrophobic groups generally dominate the SFG signal when in contact with hydrophobic media at the air/solid, or air/liquid, or liquid/solid interface.[42-44] Thus, characteristic spectral features more strongly associated with PPG are expected to appear in the SFG spectrum; Figure 6.2(e) bears this out. CH_2-stretch modes from the less hydrophobic PEG sections are not clearly identified in the spectrum. Additional SFG spectra taken for Pluronic (Figure 6.4(a)), PPG (Figure 6.4(b)), PEG (Figure 6.4(d)), and a 1:1 mixture of PPG and PEG (Figure 6.4(c)) show that the SFG spectra generated by PPG and the PPG:PEG mixture are nearly identical to those collected from Pluronic at the buffer/bead interface in terms of their peak positions and relative intensities, within the experimental error. The results indicate that the more hydrophobic PPG groups are well-ordered when contacting hydrophobic interfaces, such as air and polystyrene. Pluronics are believed to bind to the polystyrene beads via hydrophobic interactions between the bead surface and the PPG unit of the polymer, with hydrophilic PEG tails dangling out into solution.

6.3.6 SFG analysis of the air/bead interface

Although structural data obtained at the buffer/bead interface are more useful to deduce molecular structures on beads in actual working systems, investigations at the air/bead interface have also been carried out to obtain additional information that is not

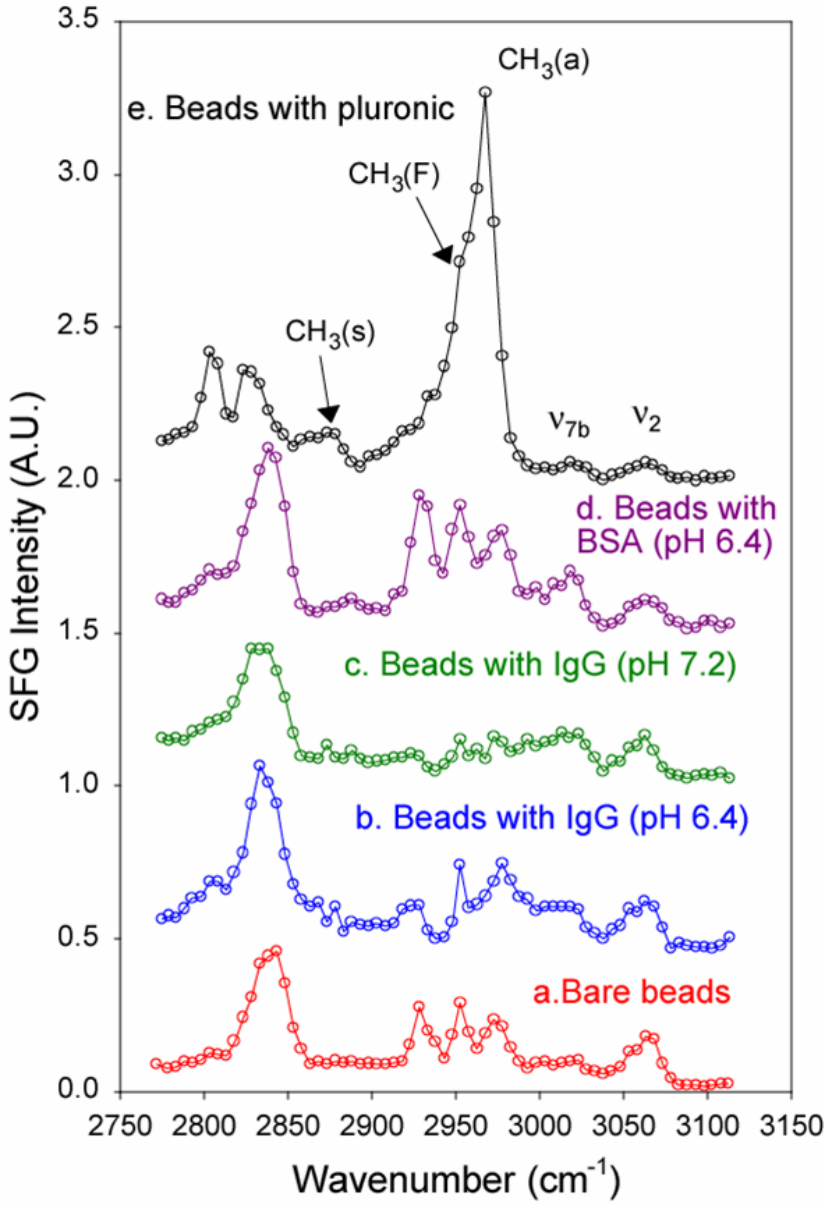

Figure 6.5: SFG spectra for (a) bare beads, (b) beads with IgG immobilized at pH 6.4, (c) beads with IgG immobilized at pH 7.2, (d) beads with BSA immobilized at pH 6.4, and (e) beads with physisorbed Pluronic at the solid/bead interface.

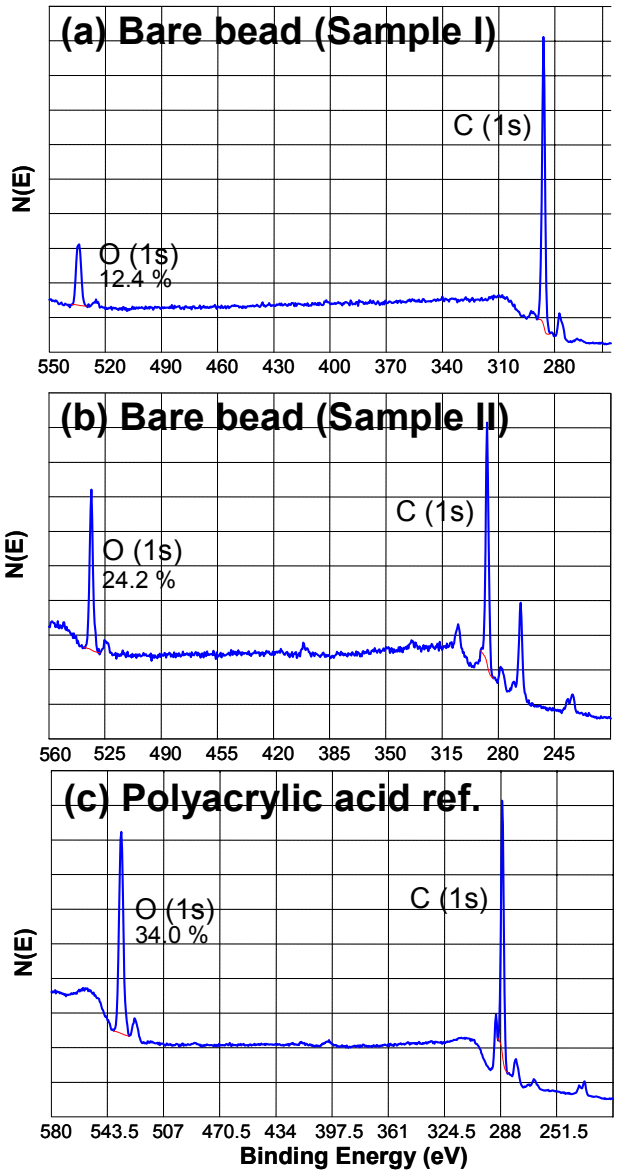

Figure 6.6: XPS spectra of bare beads in (a) sample I and (b) sample II, as well as (c) a reference spectrum of polyacrylic acid. The integrations of the O(1s) peaks (expressed as a percentage of the total area of the O(1s) and C(1s) peaks) are indicated. Sample II contains twice as much atomic oxygen (from polyacrylic acid) as sample I.

available at the buffer/bead interface. Figure 6.5 contains SFG spectra of identical bead samples at the air/bead interface for comparison with data obtained at the buffer/bead interface. Among the observable spectral differences is the presence of strong resonances around 2840 and 2950 cm^{-1}. In addition, all spectra exhibit weaker SFG signal intensity for the CH-stretch modes from the phenyl ring compared to those at the buffer/bead interface. This may indicate that adsorbed molecules (either protein or buffer components) strongly bind to the surface and disrupt phenyl ring ordering, lowering SFG signal intensity in that region.

Several remarkable resonances in the SFG spectrum of the bare bead occur around 2840 cm^{-1} and between 2925 and 2980 cm^{-1} (Figure 6.5(a)). These signals generally arise from stretch modes of aliphatic CH groups; they do not appear in the spectrum obtained at the buffer/bead interface (see Figure 6.2(a)). The methylene groups in polyacrylic acid, the other bead component, yield an SFG signal around 2930 cm^{-1} (data not shown here). Therefore, we are led to believe that some components, including buffer, are responsible for the CH resonances around 2840 and 2950 cm^{-1}, due to strong interactions with the hydrophobic bead surface at the air/bead interface.

SFG spectra for beads with IgG linked at different pH conditions are shown in Figure 6.5(b) and (c), respectively. Strong CH-stretch modes for adsorbed IgG are not observed, compared to the corresponding samples at the buffer/bead interface. This indicates that IgG molecules adsorbed between two hydrophobic surfaces (air and bead in this case) generate less signal intensity compared to IgG molecules adsorbed between a hydrophilic and a hydrophobic surface (e.g., air/water or water/bead interfaces). Amino acid residues are more likely to randomly orient at an interface when both surfaces are

hydrophobic (or hydrophilic), since surface energy differences do not force them to preferentially reorganize. Similarly, CH-stretch signals found in the SFG spectrum for beads modified with BSA in Figure 6.5(d) do not correspond to those which that were collected from BSA at the buffer/bead interface (Figure 6.2(d)). Rather, SFG spectra are dominated by signals arising from unidentified molecules (perhaps buffer components).

The SFG spectrum for beads with adsorbed Pluronic at the air/bead interface is shown in Figure 6.5(e). SFG resonances in the 2785-2840 cm^{-1} region are observed, which are not generated in the spectrum obtained at the buffer/bead interface. In addition, the SFG spectrum contains a more intense CH_3(a) signal at 2960 cm^{-1} due to the PPG section of the adsorbed Pluronic, compared to the case at the buffer/bead interface (Figure 6.2(e)). This suggests that methyl groups in the PPG section of the Pluronic are more tilted with respect to the surface normal when in contact with the hydrophobic polystyrene surface at the air/solid interface. The CH_3(a) mode appears as a shoulder peak in the spectrum obtained at the buffer/bead and air/liquid interfaces (see Figures 6.2(e) and 6.4(a), (b), and (c)). As was the case for adsorbed proteins, the results suggest that amphiphilic molecules located between a hydrophilic (water or silica) and a hydrophobic (air and bead) surface adopt a more anisotropic orientation than molecules situated between two hydrophobic (or hydrophilic) surfaces.

6.3.7 AFM analysis

In Chapter 5, the packing of beads on silica was shown to be affected by the presence of adsorbed proteins at the bead surface.[16] It is likely that the two-dimensional packing of beads is directed by their hydrophobicity, which, in turn, is related to the

orientation and ordering of functional groups at the bead surface. To obtain further structural information, AFM has been used to systematically study the aggregation behavior of beads modified with various adsorbates.

Figures 6.7 through 6.10 show AFM images collected from beads supported on silica glass slides that were analyzed by SFG at the air/bead interface (images of the same slide samples submerged in buffer appear similar). Unmodified beads deposited on silica pack in a distinctly different manner than what was observed in previous bare lattices. The beads no longer cover the surface completely, but instead form island aggregates that are not necessarily hexagonally close-packed (see Figure 6.7). This is consistent with the increased hydrophobicity suggested by the SFG results and by visual inspection of the wetting behavior of the bead suspensions. The increased hydrophobicity is related to the formation of well-aligned phenyl rings at the bead surface. Similar properties have been observed in self-assembled monolayers (SAMs), in which the orientation of terminal groups and the surface hydrophobicity depend on the parity of SAMs (an even-odd effect).[45] Rather than coating the surface, the beads prefer to minimize their surface energy by close packing instead of binding primarily to the substrate. The rms surface roughness (i.e., the rms height of the surface around its mean value) for a film of unmodified beads is ca. 250Å.

In Figure 6.8, IgG-modified beads at pH 6.4 pack densely but do not form a smooth surface. The packing is very irregular, with large variations in surface height between beads. The rms roughness was calculated to be ca. 330 Å, a higher value than that obtained for unmodified beads. At pH 7.2, IgG-modified beads pack less densely and

(a) AFM topograph

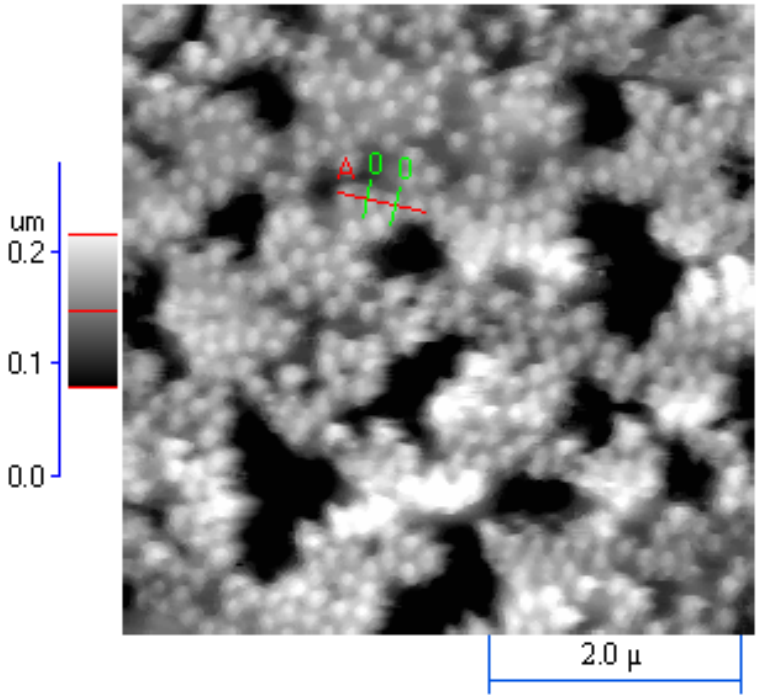

(b) AFM linescan

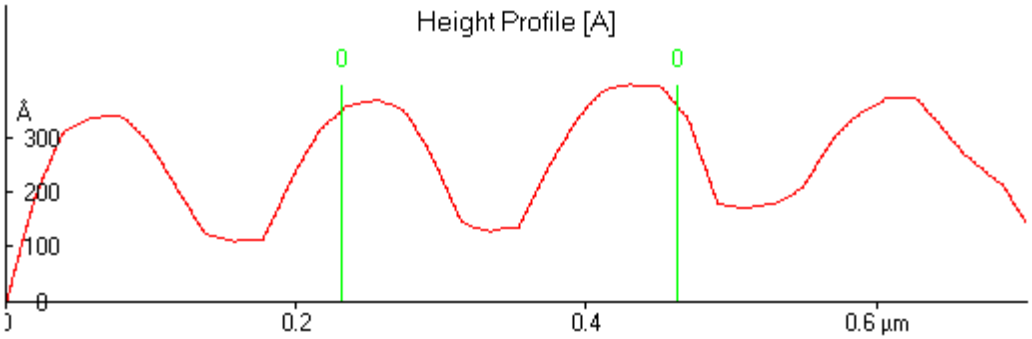

Figure 6.7: AFM topograph (a) of unmodified (bare) beads deposited on a silica substrate. Island aggregates are formed due to hydrophobic effects. The linescan (b) is also shown.

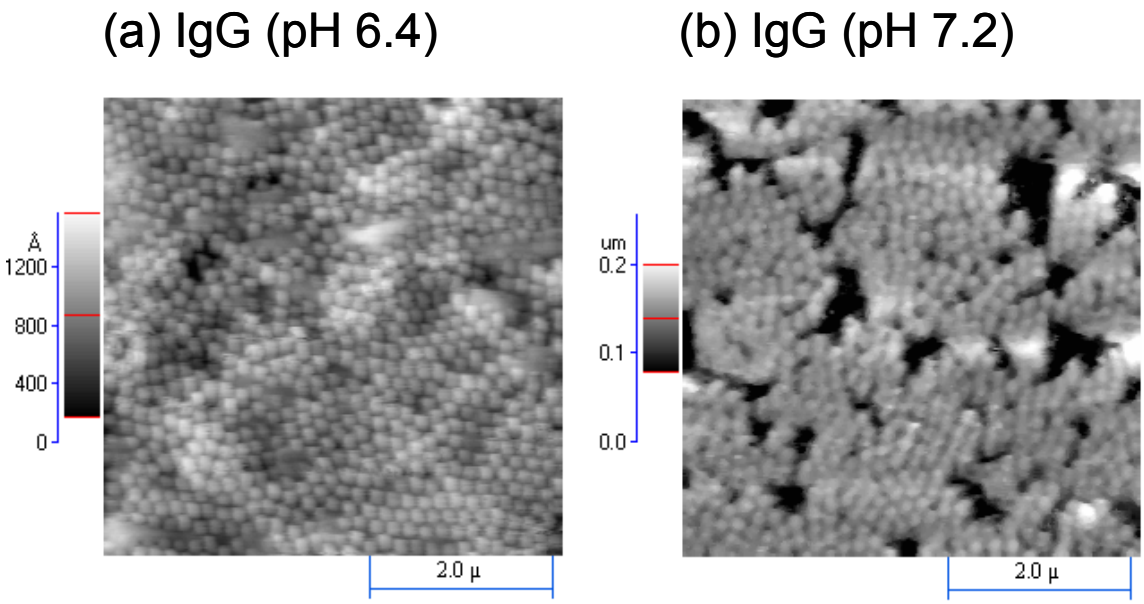

Figure 6.8: AFM topographs of beads immobilized with IgG at pH values of (a) 6.4 and (b) 7.2.

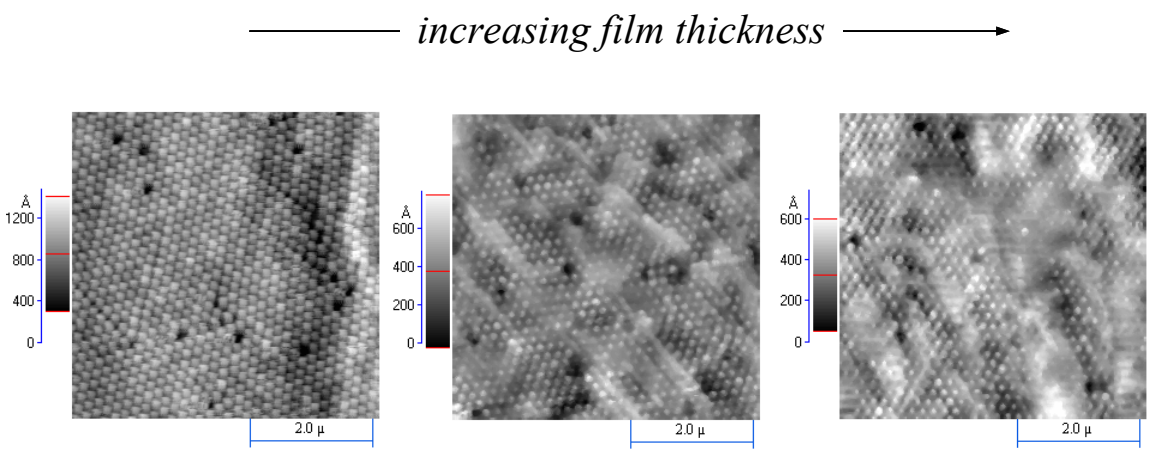

Figure 6.9: AFM topographs of the films created by BSA-modified beads. The film height increases from left to right, but surface roughness is generally maintained.

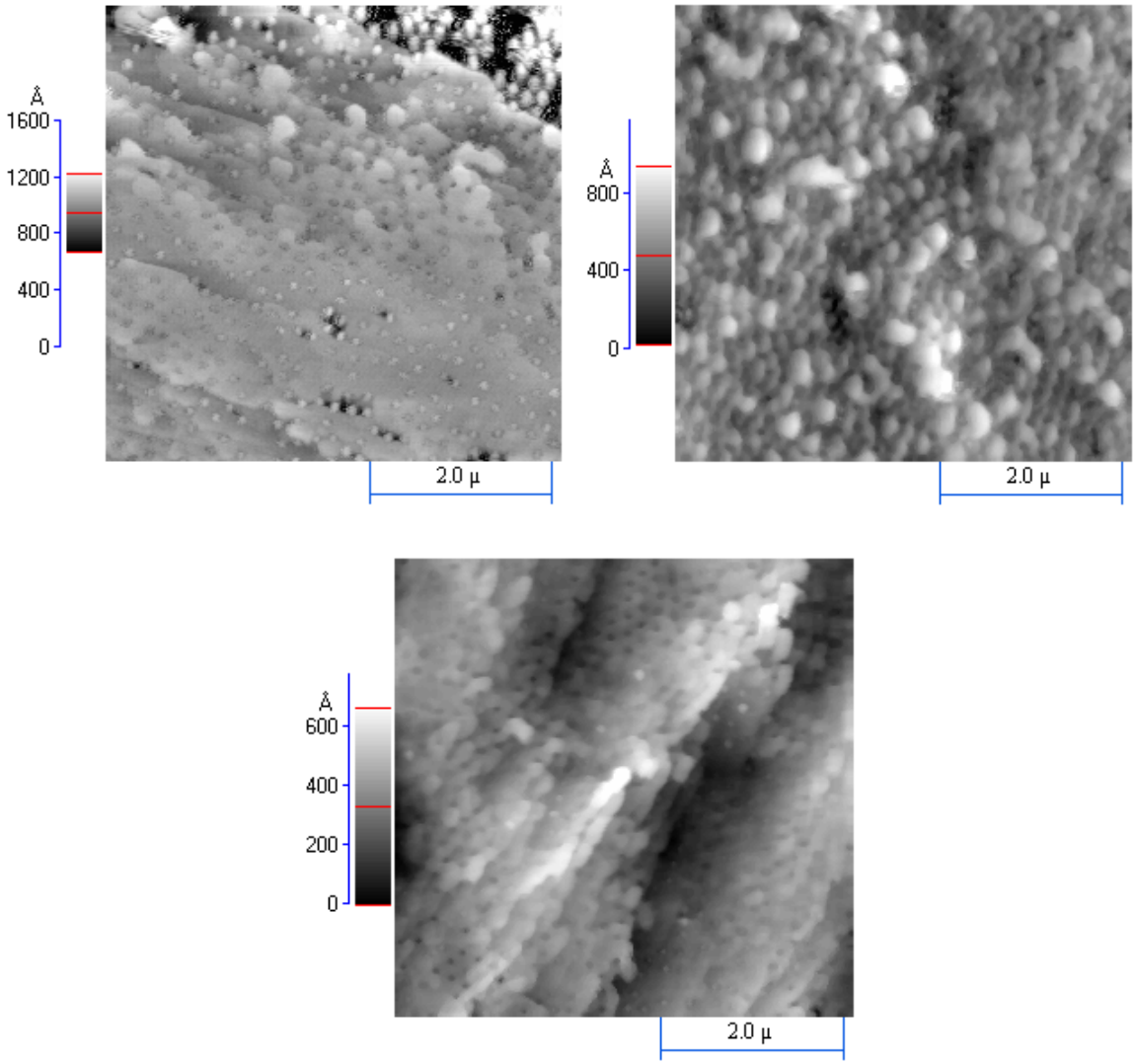

Figure 6.10: AFM topographs of films produced by Pluronic-adsorbed beads on a silica substrate. The beads are larger and appear to be held in a smooth polymer matrix.

in the same plane (Figure 6.8(b)). This surface is smoother with more open areas, relative to IgG bound at pH 6.4. These factors contribute to a low rms surface roughness of 130 Å. The observation that beads linked with IgG at pH 6.4 agglomerate more strongly than those with IgG immobilized at pH 7.2 can be explained by differences in their surface structures and properties. That is, the amino acid residues exposed at the surface dictate the hydrophobic character and the macroscopic packing or aggregation behavior of the beads, although such a difference is not directly observed in the SFG data. This data is presumably related to the immunological activity of the bead-bound IgG molecules that shows a strong dependence on the pH at which the protein adsorption step is performed (data not shown).

Surfaces are expected to reveal more disorder as the film thickness is increased. This is because irregularities in the bulk become more pronounced as monolayers of beads are built one on top of the other. However, AFM studies of films of BSA-modified beads show that they are generally ordered as the film thickness is increased, as shown in Figure 6.9. The values for the rms surface roughness are low (they vary between ca. 80 to 125 Å, depending on film thickness). These values indicate a more homogeneous surface structure, as compared to the other bead samples. It is unclear why current samples of BSA-modified beads form well-ordered films, compared to previous samples or even IgG-modified beads. Again, the increased hydrophobic character of the polystyrene beads or the immobilized BSA molecules themselves may be invoked to explain the increased number density of beads in these films. In fact, the percentage of apolar amino acid residues that are associated with protein hydrophobicity are about 50 and 37% for BSA and IgG, respectively, suggesting that BSA-covered beads are more hydrophobic.[46]

Figure 6.10 reveals that the spherical geometry of Pluronic-adsorbed beads is much less defined, relative to bare beads. They appear much larger in diameter and have a wider size distribution. In a dehydrated state, the beads become entangled in a matrix, which presumably consists of adsorbed and free Pluronic in solution. The rms roughness was calculated to be ca. 130 Å – a lower value than was found for the bare beads, due to the formation of this matrix and fewer open areas. Both hexagonal and simple square packing are observed locally for beads with adsorbed Pluronic, instead of long-range close packing. A more efficient packing is not always possible due to the irregular size distribution of these beads.

6.4 Conclusion

IR-visible SFG vibrational spectroscopy and AFM have been used to investigate the surfaces of bare polystyrene beads and those modified by covalent attachment of IgG and BSA or a physisorbed Pluronic surfactant. SFG spectra indicate that the ordering of phenyl rings at the bead surface is sensitive to the surface composition and the adsorption of proteins and polymers. Although bead-bound proteins are responsible for SFG signal intensity in the aliphatic CH-stretch region, structural differentiation by protein type or immobilization conditions (e.g., pH) is not yet feasible. The Pluronic triblock copolymer is believed to physisorb to the bead through its ordered hydrophobic polypropylene glycol moieties, with the hydrophilic polyethylene glycol chains free to move into solution and prevent subsequent protein adsorption. Surface properties of the bead are revealed by complementary AFM analysis. The increased hydrophobic character of the bare bead is observed in both macroscopic wetting behavior and AFM imaging. While a

near-complete hexagonal packing of beads is observed in the presence of protein, beads with physisorbed Pluronic are held in a polymer matrix and pack in a highly disorganized manner, relative to bare or protein-modified beads. Beads bound with IgG at pH 6.4 agglomerate more strongly than those with IgG bound at pH 7.2, presumably due to changes in protein conformation and surface charge distribution.

References

(1) *Proteins at interfaces II: Fundamentals and applications*; Horbett, T. A.; Brash, J. L., Eds.; American Chemical Society: Washington, DC, 1995.

(2) *Proteins at interfaces: Physicochemical and biochemical studies*; Brash, J. L.; Horbett, T. A., Eds.; American Chemical Society: Washington, DC, 1987.

(3) Castner, D. G.; Ratner, B. D. *Surf. Sci.* **2002**, *500*, 28.

(4) Hubbell, J. A. *Bio-Technol.* **1995**, *13*, 565.

(5) Ishihara, K.; Oshida, H.; Endo, Y.; Ueda, T.; Watanabe, A.; Nakabayashi, N. *J. Biomed. Mater. Res.* **1992**, *26*, 1543.

(6) Martin, B. D.; Gaber, B. P.; Patterson, C. H.; Turner, D. C. *Langmuir* **1998**, *14*, 3971.

(7) Kenseth, J. R.; Harnisch, J. A.; Jones, V. W.; Porter, M. D. *Langmuir* **2001**, *17*, 4105.

(8) MacBeath, G.; Schreiber, S. L. *Science* **2000**, *289*, 1760.

(9) Liu, T.; Burger, C.; Chu, B. *Prog. Polym. Sci.* **2003**, *28*, 5.

(10) Kawaguchi, H. *Prog. Polym. Sci.* **2000**, *25*, 1171.

(11) Covolan, V. L.; D'Antone, S.; Ruggeri, G.; Chiellini, E. *Macromolecules* **2000**, *33*, 6685.

(12) Green, C. E.; Wiencek, J. M.; Arnold, M. A. *Anal. Chem.* **2002**, *74*, 3392.

(13) Ghosh, D.; Faure, N.; Kundu, S.; Rondelez, F.; Chatterji, D. *Langmuir* **2003**, *19*, 5830.

(14) Morrissey, B. M.; Han, C. C. *J. Colloid Interface Sci.* **1978**, *65*, 423.

(15) Dahman, Y.; Puskas, J. E.; Margaritis, A.; Merali, Z.; Cunningham, M. *Macromolecules* **2003**, *36*, 2198.

(16) Koffas, T. S.; Kim, J.; Lawrence, C. C.; Sormorjai, G. A. *Langmuir* **2003**, *19*, 3563.

(17) Kim, J.; Somorjai, G. A. *J. Am. Chem. Soc.* **2003**, *125*, 3150.

(18) Kim, J.; Cremer, P. S. *J. Am. Chem. Soc.* **2000**, *122*, 12371.

(19) Kim, J.; Cremer, P. S. *ChemPhysChem* **2001**, *2*, 543.

(20) Kim, J.; Kim, G.; Cremer, P. S. *J. Am. Chem. Soc.* **2002**, *124*, 8751.

(21) Baldelli, S.; Mailhot, G.; Ross, P.; Somorjai, G. A. *J. Am. Chem. Soc.* **2001**, *123*, 7697.

(22) Chen, Z.; Ward, R.; Tian, Y.; Baldelli, S.; Opdahl, A.; Shen, Y. R.; Somorjai, G. A. *J. Am. Chem. Soc.* **2000**, *122*, 10615.

(23) Wang, J.; Woodcock, S. E.; Buck, S. M.; Chen, C.; Chen, Z. *J. Am. Chem. Soc.* **2001**, *123*, 9470.

(24) Gragson, D. E.; McCarty, B. M.; Richmond, G. L. *J. Am. Chem. Soc* **1997**, *119*, 6144.

(25) Himmelhaus, M.; Eisert, F.; Buck, M.; Grunze, M. *J. Phys. Chem. B* **2000**, *104*, 576.

(26) Liu, Y.; Messmer, M. C. *J. Am. Chem. Soc.* **2002**, *124*, 9714.

(27) Clark, H. A.; Campagnola, P. J.; Wuskell, J. P.; Lewis, A.; Loew, L. M. *J. Am. Chem. Soc.* **2000**, *122*, 10234.

(28) Kawai, T.; Neivandt, D. J.; Davies, P. B. *J. Am. Chem. Soc.* **2000**, *122*, 12031.

(29) Ma, G.; Allen, H. C. *J. Am. Chem. Soc.* **2002**, *124*, 9374.

(30) Kim, D. T.; Blanch, H. W.; Radke, C. J. *Langmuir* **2002**, *18*, 5841.

(31) Takano, H.; Kenseth, J. R.; Wong, S. S.; O'Brien, J. C.; Porter, M. D. *Chem. Rev.* **1999**, *99*, 2845.

(32) Ortega-Vinuesa, J. L.; Tengvall, P.; Lundström, I. *J. Colloid Interf. Sci.* **1998**, *207*, 228.

(33) Yam, C.-M.; Xiao, Z.; Gu, J.; Boutet, S.; Cai, C. *J. Am. Chem. Soc.* **2003**, *125*, 7498.

(34) Shen, Y. R. *Nature* **1989**, *337*, 519.

(35) Shen, Y. R. *Surf. Sci.* **1994**, *299/300*, 551.

(36) Betton, F.; Theretz, A.; Elaissari, A.; Pichot, C. *Colloids Surf. B* **1993**, *1*, 97.

(37) Opdahl, A.; Phillips, R. A.; Somorjai, G. A. *J. Phys. Chem. B* **2002**, *106*, 5212.

(38) Gautam, K. S.; Schwab, A. D.; Dhinojwala, A. *Phys. Rev. Lett.* **2000**, *85*, 3854.

(39) Zhang, D.; Dougal, S. M.; Yeganeh, M. S. *Langmuir* **2000**, *16*, 4528.

(40) Kim, J.; Chou, K. C.; Somorjai, G. A. *J. Phys. Chem. B* **2003**, *107*, 1592.

(41) Wolfrum, K.; Graener, H.; Laubereau, A. *Chem. Phys. Lett.* **1993**, *213*, 41.

(42) Kim, J.; Opdahl, A.; Chou, K. C.; Somorjai, G. A. *Langmuir* **2003**, *19*, 9551.

(43) Ward, R. N.; Davies, P. B.; Bain, C. D. *J. Phys. Chem.* **1993**, *97*, 7141.

(44) Ward, R. N.; Duffy, D. C.; Davies, P. B.; Bain, C. D. *J. Phys. Chem.* **1994**, *98*, 8536.

(45) Colorado Jr., R.; Lee, T. R. *J. Phys. Org. Chem*. **2000***, 13,* 796.

(46) Halle, B.; Andersson, T; Forsen, S.; Lindman, B. *J. Am. Chem. Soc.* **1981**, *103*, 500.